DEPARTMENT OF PHYSICS
UNIVERSITY OF JYVÄSKYLÄ
RESEARCH REPORT No. 12/2009

SHAPE COEXISTENCE IN LIGHT BISMUTH AND ASTATINE ISOTOPES - AN IN-BEAM AND DECAY SPECTROSCOPIC STUDY

BY
MARKUS NYMAN

Academic Dissertation
for the Degree of
Doctor of Philosophy

To be presented, by permission of the
Faculty of Mathematics and Natural Sciences
of the University of Jyväskylä,
for public examination in Auditorium FYS-1 of the
University of Jyväskylä on November 23rd, 2009
at 12 o'clock noon

Jyväskylä, Finland
November 2009

Preface

The experiments on which this work is based were carried out during the JUROGAM 1 campaign, which lasted from 2003 to 2008. The author had the privilege of participating in the work of the reasearch group throughout most of that time.

I wish to express my most sincere thanks to the leaders of Gamma- and RITU groups, Prof. Rauno Julin and Prof. Matti Leino, who a long time ago first gave me the chance to start working in this field. The expertise, support and extraordinary patience of my supervisor, Dr. Sakari Juutinen, is also acknowledged with gratitude. Several other people also sacrificed their time and read through the manuscript offering valuable advice: Dr. Juha Uusitalo, Dr. Päivi Nieminen and Dr. Cath Scholey. I want to express a warm thankyou to them.

The thesis work only formed a part of the tasks that go with being a member of an experimental nuclear physics research group. A large part of my own time was devoted to the maintenance of the JUROGAM gamma-ray spectrometer. I had the great pleasure to learn this part of the work of a nuclear physicist from Dr. Janne Pakarinen, Dr. Tuomas Grahn and our JUROGAM project manager, Dr. Pete Jones. Over the years I worked together with many other members of our group in these detector maintenance tasks: Mr. Juha Sorri, Mr. Pauli Peura, Mr. Steffen Ketelhut, Ms. Ulrika Jakobsson and Mr. Panu Ruotsalainen. It has been a pleasure. It has also been a pleasure to be able to pass the torch to them, knowing that the detectors are in good hands. I would also like to mention the members of the mechanical and electrical workshops, who provided essential support whenever it was needed. Furthermore, the past and present members of Gamma- and RITU-groups and other colleagues not mentioned above deserve a warm thankyou for most pleasant experiences during our daily work as well as in various conferences and summer schools.

Outside the research group, I also want to mention all the friends with whom I had the privilege to spend time throughout my journey in the University of Jyväskylä. Some of them are still around here while others have left, but all of them deserve a warm word of thanks. And finally I want to sincerely thank my family for the altruistic support they have always given me.

Jyväskylä, November 2009

Markus Nyman

Abstract

This thesis is based on the results of two experiments carried out at the Accelerator Laboratory of the Department of Physics, University of Jyväskylä. Detailed gamma-ray spectroscopy was performed to study the very neutron-deficient nucleus ^{191}Bi. As a result an extended level scheme was constructed and, for the first time, superdeformation was observed in such a light Bi isotope. The other experiment consisted of in-beam and decay spectroscopic studies of ^{195}At. Gamma-rays originating from the decays of excited states in this nucleus were observed for the first time. Furthermore, the details of the decay modes of low-lying states were investigated. This experiment also provided decay data for the odd-odd astatine isotopes, ^{194,196}At. As a result, their earlier decay schemes were revised.

Contents

1 Introduction

It has been known for about a century that an atom consists of a very dense nucleus surrounded by a cloud of electrons. The basis for this was the famous gold foil experiment performed by Geiger and Marsden, where some alpha particles impacting the foil were found to be deflected to large angles. Rutherford was able to explain the results by assuming most of the atomic mass to be concentrated in a very small nucleus. A model where the nucleus was composed of positively charged protons and uncharged neutrons was put forward by Heisenberg in 1932. Today a total of 117 different elements are known to exist. The chemical nature of an element is dictated by the structure of its electron cloud. The number of electrons orbiting a neutral atom (the atomic number) is the same as the number of protons (denoted as Z) contained in the nucleus. Atoms of the same element that contain a different number of neutrons (N) in their nuclei are called isotopes of that particular element. The change in neutron number has no effect on the chemical properties of an element but can have rather significant effect on the properties of the nucleus itself. There exists 256 isotopes that are stable, i.e. they do not undergo radioactive decay. Additionally about 80 radioactive isotopes exist naturally on this planet, some of which have been around since the formation of the Earth while others are continuously created in the decay of the primordial nuclides or due to cosmic radiation. The vast majority of different nuclear species that are known to exist are produced artificially using facilities such as particle accelerators or nuclear reactors. Most of these are very short-lived and rapidly decay into more stable isotopes. As an example, the nuclei studied in this work had lifetimes around milliseconds or seconds. The longest observed lifetimes of radioactive isotopes are as long as billions of years. The total number of known isotopes is currently more than 3100. These are displayed in the chart of the nuclides in figure 1.1.

Studies of the structure of the atomic nucleus have been ongoing ever since the existence of the nucleus was first deduced. Today these studies largely focus of the behaviour of nuclei in extreme conditions, such as high energy, high angular momentum or imbalance between the number of neutrons and protons in the nucleus. The work presented in this thesis involves the study of certain bismuth ($Z = 83$) and astatine ($Z = 85$) isotopes with a large deficiency of neutrons when compared with the most stable isotopes of these elements. A large problem hampering the study of very exotic nuclei such as these is the extreme difficulty in producing them. They can be created in nuclear reactions by shooting a beam of particles onto a target foil, resulting in a fusion reaction where the beam and target nuclei combine to form the final product. Unfortunately the probability of forming a specific nucleus is very small: most likely

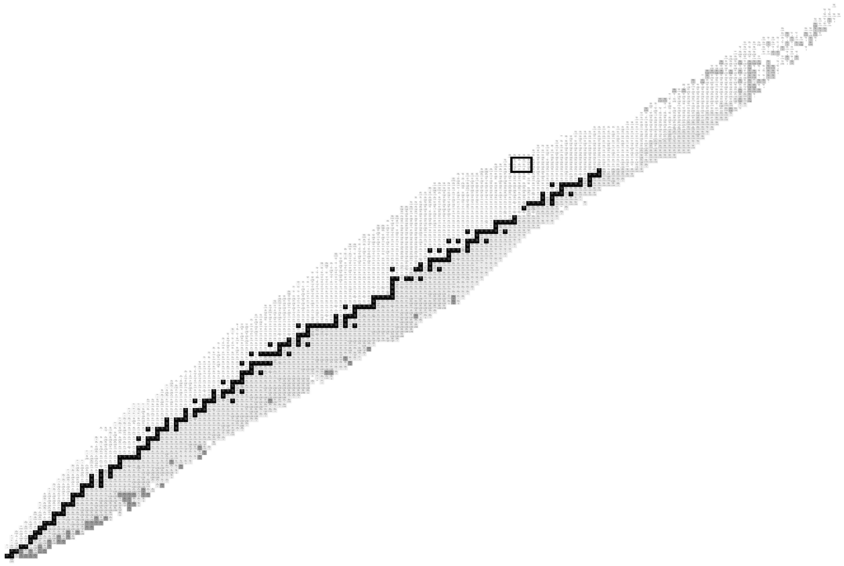

Figure 1.1: The nuclear chart, showing the currently known isotopes. Neutron number increases towards the right and proton number upwards. The filled black squares represent the stable isotopes, all the rest are radioactive. The nuclei studied in the present work (^{191}Bi, ^{194,195,196}At) lie inside the little rectangle.

the beam passes through the target missing all the target nuclei (the diameter of the nucleus is roughly 0.01 % of that of the atom). In the unlikely case that the beam particle meets a target nucleus, a variety of nuclear reactions can occur, only one of which is the fusion reaction. Even if the two nuclei do fuse together, the chances are that the product immediately breaks apart in a fission reaction. Finally, in order to obtain information of the fusion product, there is the problem of identifying it and detecting the radiation emitted by it. This is the needle in the haystack problem that need to be solved if these exotic nuclei are to be studied. As explained in chapter 3 of this thesis, this requires rather complex equipment and lengthy experiments - typically days or weeks.

The author has had the priviledge to participate in the preparation and carrying out of a large number of experiments for almost the entire duration of the first incarnation of the JUROGAM spectrometer. Additionally the author has carried the main responsibility of the maintenance and repair of the Ge-detectors and the associated automatic liquid nitrogen filling system. This period of time has resulted in a number of publications in peer-reviewed scientific journals; the ones of which this author has contributed are listed below. The results reported in this thesis are also the topic of the first three articles on the list.

Shape coexistence in the Pb region

M. Nyman, S. Eeckhaudt, T. Grahn, P.T. Greenlees, H. Kettunen, P. Jones, R. Julin, S. Juutinen, M. Leino, A.-P. Leppänen, P. Nieminen, J. Pakarinen, P. Rahkila, J. Sarén, C. Scholey, J. Sorri and J. Uusitalo,
In-beam and decay spectroscopy of ^{195}At
Proceedings of the 23rd International Nuclear Physics Conference, Tokyo, Japan, 3-8 June 2007, Elsevier B.V, Dorchester UK, 2008, p.227.

M. Nyman, S. Eeckhaudt, T. Grahn, P.T. Greenlees, H. Kettunen, P. Jones, R. Julin, S. Juutinen, M. Leino, A.-P. Leppänen, P. Nieminen, J. Pakarinen, P. Rahkila, J. Sarén, C. Scholey, J. Sorri and J. Uusitalo,
In-beam and decay spectroscopy of ^{195}At
To be published.

M. Nyman, S. Eeckhaudt, T. Grahn, P.T. Greenlees, H. Kettunen, P. Jones, R. Julin, S. Juutinen, M. Leino, A.-P. Leppänen, P. Nieminen, J. Pakarinen, P. Rahkila, J. Sarén, C. Scholey, J. Sorri and J. Uusitalo,
Superdeformation and non-yrast states in ^{191}Bi
To be published.

T. Grahn, A. Dewald, P.T. Greenlees, U. Jakobsson, J. Jolie, P. Jones, R. Julin, S. Juutinen, S. Ketelhut, T. Kröll, R. Krücken, M. Leino, P. Maierbeck, B. Melon, M. Nyman, R.D. Page, P. Peura, Th. Pissulla, P. Rahkila, J. Sarén, C. Scholey, J. Sorri and J. Uusitalo
Lifetime measurement in ^{195}Po
European Physical Journal A **39** 291 (2009).

D. O'Donnell, J. Simpson, C. Scholey, T. Bäck, P.T. Greenlees, U. Jakobsson, P. Jones, D.T. Joss, D.S. Judson, R. Julin, S. Juutinen, S. Ketelhut, M. Labiche, M. Leino, M. Nyman, R.D. Page, P. Peura, P. Rahkila, P. Ruotsalainen, M. Sandzelius, P.J. Sapple, J. Sarén, J. Thomson, J. Uusitalo and H.V. Watkins
First observation of excited states in ^{175}Hg
Physical Review C **79** 051304(R) (2009).

M. Sandzelius, E. Ganioğlu, B. Cederwall, B. Hadinia, K. Andgren, T. Bäck, T. Grahn, P. Greenlees, U. Jakobsson, A. Johnson, P.M. Jones, R. Julin, S. Juutinen, S. Ketelhut, A. Khaplanov, M. Leino, M. Nyman, P. Peura, P. Rahkila, J. Sarén, C. Scholey, J. Uusitalo and R. Wyss
First observation of excited states in ^{172}Hg
Physical Review C **79** 064315 (2009).

T. Grahn, A. Dewald, O. Möller, R. Julin, C.W. Beausang, S. Christen, I.G. Darby, S.

Eeckhaudt, P.T. Greenlees, A. Görgen, K. Helariutta, J. Jolie, P. Jones, S. Juutinen, H. Kettunen, T. Kröll, R. Krücken, Y. Le Coz, M. Leino, A.-P. Leppänen, P. Maierbeck, D.A. Meyer, B. Melon, P. Nieminen, M. Nyman, R.D. Page, J. Pakarinen, P. Petkov, P. Rahkila, B. Saha, M. Sandzelius, J. Sarén, C. Scholey, J. Uusitalo, M. Bender and P.-H. Heenen
Lifetimes of intruder states in ^{186}Pb, ^{188}Pb and ^{194}Po
Nuclear Physics A **801** 83 (2008).

K. Andgren, B. Cederwall, J. Uusitalo, A.N. Andreyev, S.J. Freeman, P.T. Greenlees, B. Hadinia, U. Jakobsson, A. Johnson, P.M. Jones, D.T. Joss, S. Juutinen, R. Julin, S. Ketelhut, A. Khaplanov, M. Leino, M. Nyman, R.D. Page, P. Rahkila, M. Sandzelius, P. Sapple, J. Sarén, C. Scholey, J. Simpson, J. Sorri, J. Thomson and R. Wyss
Excited states in the neutron-deficient nuclei ^{197,199,201}Rn
Physical Review C **77** 054303 (2008).

K. Andgren, U. Jakobsson, B. Cederwall, J. Uusitalo, T. Back, S.J. Freeman, P.T. Greenlees, B. Hadinia, A. Hugues, A. Johnson, P.M. Jones, D.T. Joss, S. Juutinen, R. Julin, S. Ketelhut, A. Khaplanov, M. Leino, M. Nyman, R.D. Page, P. Rahkila, M. Sandzelius, P. Sapple, J. Saren, C. Scholey, J. Simpson, J. Sorri, J. Thomson and R.Wyss
Gamma-ray spectroscopy of ^{197}At
Physical Review C **78** 044328 (2008).

J. Pakarinen, V. Hellemans, R. Julin, S. Juutinen, K. Heyde, P.-H. Heenen, M. Bender, I.G. Darby, S. Eeckhaudt, T. Enqvist, T. Grahn, P.T. Greenlees, F. Johnston-Theasby, P. Jones, H. Kettunen, M. Leino, A.-P. Leppänen, P. Nieminen, M. Nyman, R.D. Page, P.M. Raddon, P. Rahkila, C. Scholey, J. Uusitalo and R. Wadsworth
Investigation of nuclear collectivity in the neutron mid-shell nucleus ^{186}Pb
Physical Review C **75** 014302 (2007).

D.R. Wiseman, A.N. Andreyev, R.D. Page, M.B. Smith, I.G. Darby, S. Eeckhaudt, T. Grahn, P.T. Greenlees, P. Jones, R. Julin, S. Juutinen, H. Kettunen, M. Leino, A.-P. Leppänen, M. Nyman, J. Pakarinen, P. Rahkila, M. Sandzelius, J. Sarén, C. Scholey and J.Uusitalo
In-beam gamma-ray spectroscopy of ^{190,197}Po
European Physical Journal A **34** 275 (2007).

T. Grahn, A. Dewald, O. Möller, R. Julin, C.W. Beausang, S. Christen, I.G. Darby, S. Eeckhaudt, P.T. Greenlees, A. Görgen, K. Helariutta, J. Jolie, P. Jones, S. Juutinen, H. Kettunen, T. Kröll, R. Krücken, Y. Le Coz, M. Leino, A.-P. Leppänen, P. Maierbeck, D.A. Meyer, B. Melon, P. Nieminen, M. Nyman, R. D. Page, J. Pakarinen, P. Petkov, P. Rahkila, B. Saha, M. Sandzelius, J. Sarén, C. Scholey and J. Uusitalo
Collectivity and Configuration Mixing in ^{186,188}Pb and ^{194}Po
Physical Review Letters **97** 062501 (2006).

J. Pakarinen, I.G. Darby, S. Eeckhaudt, T. Enqvist, T. Grahn, P.T. Greenlees, V. Hellemans, K. Heyde, F. Johnston-Theasby, P. Jones, R. Julin, S. Juutinen, H. Kettunen, M. Leino, A.-P. Leppänen, P. Nieminen, M. Nyman, R.D. Page, P.M. Raddon, P. Rahkila, C. Scholey, J. Uusitalo and R.Wadsworth
Evidence for oblate structure in ^{186}Pb
Physical Review C **72** (2005) 011304.

Other topics

P.J.R. Mason, D.M. Cullen, C. Scholey, S. Eeckhaudt, T. Grahn, P.T. Greenlees, U. Jakobsson, P.M. Jones, R. Julin, S. Juutinen, S. Ketelhut, A.M. Kishada, M. Leino, A.-P.Leppänen, K. Mäntyniemi, P. Nieminen, M. Nyman, J. Pakarinen, P. Peura, P. Rahkila, S.V. Rigby, J. Sarén, J. Sorri, J. Uusitalo, B.J. Varley and M. Venhart
Prompt and delayed spectroscopy of ^{142}Tb using recoil-isomer tagging
Physical Review C **79** 024318 (2009).

S. Ketelhut, P.T. Greenlees, D. Ackermann, S. Antalic, E. Clément, I.G. Darby, O. Dorvaux, A. Drouart, S. Eeckhaudt, B.J.P. Gall, A. Görgen, T. Grahn, C. Gray-Jones, K. Hauschild, R.-D. Herzberg, F.P. Heßberger, U. Jakobsson, G.D. Jones, P. Jones, R. Julin, S. Juutinen, T.-L. Khoo, W. Korten, M. Leino, A.-P. Leppänen, J. Ljungvall, S. Moon, M. Nyman, A. Obertelli, J. Pakarinen, E. Parr, P. Papadakis, P. Peura, J. Piot, A. Pritchard, P. Rahkila, D. Rostron, P. Ruotsalainen, M. Sandzelius, J. Sarén, C. Scholey, J. Sorri, A. Steer, B. Sulignano, Ch. Theisen, J. Uusitalo, M. Venhart, M. Zielinska, M. Bender and P.-H. Heenen
Gamma-Ray Spectroscopy at the Limits: First Observation of Rotational Bands in ^{255}Lr
Physical Review Letters **102** 212501 (2009).

D. O'Donnell, T. Grahn, D.T. Joss, J. Simpson, C. Scholey, K. Andgren, L. Bianco, B. Cederwall, D.M. Cullen, A. Dewald, E.Ganioğlu, M.B. Gómez Hornillos, P.T. Greenlees, B. Hadinia, H. Iwasaki, U. Jakobsson, J. Jolie, P. Jones, D.S. Judson, R. Julin, S. Juutinen, S. Ketelhut, M. Labiche, M. Leino, N.M. Lumley, P.J.R. Mason, O.Möller, P. Nieminen, M. Nyman, R.D. Page, J. Pakarinen, E.S. Paul, M. Petri, A. Petts, P. Peura, N. Pietralla, Th. Pissulla, P. Rahkila, P. Ruotsalainen, M. Sandzelius, P.J. Sapple, J. Sarén, J. Sorri, J. Thomson, J. Uusitalo and H.V. Watkins
Spectroscopy of the neutron-deficient nucleus ^{167}Os
Physical Review C **79** 064309 (2009).

M.B. Gómez Hornillos, D. O'Donnell, J. Simpson, D.T. Joss, L. Bianco, B. Cederwall, T. Grahn, P.T. Greenlees, B. Hadinia, P. Jones, R. Julin, S. Juutinen, S. Ketelhut, M. Labiche, M. Leino, M. Nyman, R.D. Page, E.S. Paul, M. Petri, P. Peura, P. Rahkila, P. Ruotsalainen, M. Sandzelius, P.J. Sapple, J. Sarén, C. Scholey, J. Sorri, J. Thomson

and J. Uusitalo
Gamma-ray spectroscopy approaching the limits of existence of atomic nuclei: A study of the excited states of ^{168}Pt and ^{169}Pt
Physical Review C **79** 064314 (2009).

P.T. Greenlees, R.-D. Herzberg, S. Ketelhut, P.A. Butler, P. Chowdhury, T. Grahn, C. Gray-Jones, G.D. Jones, P. Jones, R. Julin, S. Juutinen, T.-L. Khoo, M. Leino, S. Moon, M. Nyman, J. Pakarinen, P. Rahkila, D. Rostron, J. Sarén, C. Scholey, J. Sorri, S.K. Tandel, J. Uusitalo and M. Venhart
High-K structure in ^{250}Fm and the deformed shell gaps at N=152 and Z=100
Physical Review C **78** 021303(R) (2008).

S.V. Rigby, D.M. Cullen, P.J.R. Mason, D.T. Scholes, C. Scholey, P. Rahkila, S. Eeckhaudt, T. Grahn, P. Greenlees, P.M. Jones, R. Julin, S. Juutinen, H. Kettunen, M. Leino, A.-P. Leppanen, P. Nieminen, M. Nyman, J. Pakarinen and J. Uusitalo
Decay of a proton $h_{11/2} \otimes$ neutron $h_{11/2}$ microsecond isomer in ^{136}Pm
Physical Review C **78** 034304 (2008).

L. Bianco, R.D. Page, D.T. Joss, J. Simpson, B. Cederwall, M.B. Gómez Hornillos, P.T. Greenlees, B. Hadinia, U. Jakobsson, P.M. Jones, R. Julin, S. Ketelhut, M. Labiche, M. Leino, M. Nyman, E.S. Paul, M. Petri, P. Peura, A. Puurunen, P. Rahkila, P. Ruotsalainen, M. Sandzelius, P.J. Sapple, J. Saren, C. Scholey, J. Thomson and J. Uusitalo
Alpha-decay branching ratios measured by gamma-ray tagging
Nuclear Instruments and Methods in Physics Research A **597** 189 (2008).

B.S. Nara Singh, A.N. Steer, D.G. Jenkins, R. Wadsworth, M.A. Bentley, P.J. Davies, R. Glover, N.S. Pattabiraman, C.J. Lister, T. Grahn, P.T. Greenlees, P. Jones, R. Julin, S. Juutinen, M. Leino, M. Nyman, J. Pakarinen, P. Rahkila, J. Sarén, C. Scholey, J. Sorri, J. Uusitalo, P.A. Butler, M. Dimmock, D.T. Joss, J. Thomson, B. Cederwall, B. Hadinia and M. Sandzelius
Coulomb shifts and shape changes in the mass 70 region
Physical Review C **75** 061301(R) (2007).

M. Petri, E.S. Paul, B. Cederwall, I.G. Darby, M.R. Dimmock, S. Eeckhaudt, E. Ganioglu, T. Grahn, P.T. Greenlees, B. Hadinia, P. Jones, D.T. Joss, R. Julin, S. Juutinen, S. Ketelhut, A. Khaplanov, M. Leino, L. Nelson, M. Nyman, R.D. Page, P. Rahkila, M. Sandzelius, J. Sarén, C. Scholey, J. Sorri, J. Uusitalo and R. Wadsworth
Nuclear levels in proton-unbound ^{109}I: Relative single-particle energies beyond the proton drip line
Physical Review C **76** 054301 (2007).

K. Lagergren, D.T. Joss, R. Wyss, B. Cederwall, C.J. Barton, S. Eeckhaudt, T. Grahn, P.T. Greenlees, B. Hadinia, P.M. Jones, R. Julin, S. Juutinen, D. Karlgren, H. Ket-

tunen, M. Leino, A.-P.Leppänen, P. Nieminen, M. Nyman, R.D. Page, J. Pakarinen, E.S. Paul, P. Rahkila, C. Scholey, J. Simpson, J. Uusitalo and D.R. Wiseman
High-spin states in the proton-unbound nucleus ^{161}Re
Physical Review C **74** 024316 (2006).

R.D. Herzberg, P.T. Greenlees, P.A. Butler, G.D. Jones, M. Venhart, I.G. Darby, S. Eeckhaudt, K. Eskola, T. Grahn, C. Gray-Jones, F.P. Heßberger, P. Jones, R. Julin, S. Juutinen, S. Ketelhut, W. Korten, M. Leino, A.-P. Leppänen, S. Moon, M. Nyman, R.D. Page, J. Pakarinen, A. Pritchard, P. Rahkila, J. Sarén, C. Scholey, A. Steer, Y. Sun, Ch. Theisen and J.Uusitalo,
Nuclear isomers in superheavy elements as stepping stones towards the island of stability
Nature **442** 896 (2006).

K. Lagergren, D.T. Joss, R. Wyss, B. Cederwall, C.J. Barton, S. Eeckhaudt, T. Grahn, P.T. Greenlees, B. Hadinia, P.M. Jones, R. Julin, S. Juutinen, D. Karlgren, H. Kettunen, M. Leino, A.-P. Leppänen, P. Nieminen, M. Nyman, R.D. Page, J. Pakarinen, E.S. Paul, P. Rahkila, C. Scholey, J. Simpson, J. Uusitalo and D.R. Wiseman,
High-spin states in the proton-unbound nucleus ^{161}Re
Physical Review C **74** 024316 (2006).

A.-P. Leppänen, J. Uusitalo, P.T. Greenlees, R.-D. Herzberg, N. Amzal, F. Becker, P.A. Butler, A.J.C. Chewter, J.F.C. Cocks, O. Dorvaux, S. Eeckhaudt, K. Eskola, J. Gerl, T. Grahn, N.J. Hammond, K. Hauschild, K. Helariutta, F.P. Heßberger, M. Houry, G.D. Jones, P.M. Jones, R. Julin, S. Juutinen, H. Kankaanpaa, H. Kettunen, T.L. Khoo, W. Korten, P. Kuusiniemi, Y. Le Coz, M. Leino, C.J. Lister, R. Lucas, M. Muikku, P. Nieminen, M. Nyman, R.D. Page, J. Pakarinen, P. Rahkila, P. Reiter, J. Sarén, Ch. Schlegel, C. Scholey, O. Stezowski, Ch. Theisen, W.H. Trzaska and H.J. Wollersheim,
Recoil-fission tagging of the transfermium nucleus ^{252}No
European Physical Journal A **28** 301 (2006).

A.N. Steer, D.G. Jenkins, R. Glover, B.S. Nara Singh, N.S. Pattabiraman, R. Wadsworth, S. Eeckhaudt, T. Grahn, P.T. Greenlees, P. Jones, R. Julin, S. Juutinen, M. Leino, M. Nyman, J. Pakarinen, P. Rahkila, J. Saren, C. Scholey, J. Sorri, J. Uusitalo, P.A. Butler, I.G. Darby, R.-D. Herzberg, D.T. Joss, R.D. Page, J. Thomson, R. Lemmon, J. Simpson and B. Blank
Recoil-beta tagging: A novel technique for studying proton-drip-line nuclei
Nuclear Instruments and Methods in Physics Research A **565** 630 (2006).

D.T. Joss, I.G. Darby, R.D. Page, J. Uusitalo, S. Eeckhaudt, T. Grahn, P.T. Greenlees, P.M. Jones, R. Julin, S. Juutinen, S. Ketelhut, M. Leino, A.-P. Leppänen, M. Nyman, J. Pakarinen, P. Rahkila, J. Saren, C. Scholey, A. Steer, A.J. Cannon, P.D. Stevenson, J.S. Al-Khalili, S. Ertürk, M. Venhart, B.Gall, B. Hadinia and J.Simpson,

Probing the limit of nuclear existence: Proton emission from ^{159}Re
Physics Letters B **641** 34 (2006).

C. Scholey, M. Sandzelius, S. Eeckhaudt, T. Grahn, P.T. Greenlees, P. Jones, R. Julin, S. Juutinen, M. Leino, A.-P. Leppänen, P. Nieminen, M. Nyman, J. Perkowski, J. Pakarinen, P. Rahkila, P.M. Rahkila, J. Uusitalo, K. Van de Vel, B. Cederwall, B. Hadinia, K. Lagergren, D.T. Joss, D.E. Appelbe, C.J. Barton, J. Simpson, D.D. Warner, I.G. Darby, R.D. Page, E.S. Paul and D. Wiseman
In-beam and decay spectroscopy of very neutron deficient iridium nuclei
Journal of Physics G **31** S1719 (2005).

S. Rigby, D.M. Cullen, D.T. Scholes, C. Scholey, P. Rahkila, S. Eeckhaudt, T. Grahn, P. Greenlees, P.M. Jones, R. Julin, S. Juutinen, H. Kettunen, M. Leino, A. Leppänen, P. Nieminen, M. Nyman, J. Pakarinen and J.Uusitalo
Mass-140 isomers near the proton dripline
Journal of Physics G **31** S1949 (2005).

B. Hadinia, B. Cederwall, K. Lagergren, J. Blomqvist, T. Back, S. Eeckhaudt, T. Grahn, P. Greenlees, A. Johnson, D.T. Joss, R. Julin, S. Juutinen, H. Kettunen, M. Leino, A.-P. Leppänen, R.J. Liotta, P. Nieminen, M. Nyman, J. Pakarinen, E.S. Paul, P. Rahkila, C. Scholey, J. Uusitalo, R. Wadsworth and D.R. Wiseman
First identification of gamma-ray transitions in ^{107}Te
Physical Review C **70** 064314 (2004).

2 Physics background

In this section some theoretical concepts relevant to the present work are introduced. Firstly various nuclear models are discussed. This is followed by a brief introduction to various nuclear decay processes, with emphasis on those relevant to this thesis. Lastly, some features encountered in the region of the nuclear chart where this work is centred are introduced.

2.1 Nuclear models

In modelling the atomic nucleus various different approaches can be adopted. One is to treat the nucleus as a system of N neutrons and Z protons interacting with each other. Although the range of the nuclear force has been observed to be very short, indicating that the nucleons only interact with their nearest neighbours, as N and Z increase this approach gets more and more complicated. A way to simplify the picture is to consider only the outermost valence nucleons as active players, while the rest form an inert core. Another approach is to consider the entire nucleus as a "macroscopic" entity, where many or all of the constituent nucleons contribute to collective behaviour, such as rotation and vibration of the nucleus. The two approaches can also be combined.

2.1.1 The spherical shell model

In the spirit of the highly successful atomic shell model a similar model was constructed for the nucleus. The idea is that the nucleons are bound in a potential well they themselves create. This is in contrast to the atomic model where the electrons orbit in a potential created by an external agent, the nucleus. There is adequate evidence for a shell structure in nuclei, such as large changes in proton and neutron separation energies, neutron capture cross sections and changes in nuclear radii occurring at the same values of proton or neutron numbers (the "magic numbers" 2, 8, 20, 28, 50, 82 and for neutrons 126). There is an ongoing debate as to the values of the next magic numbers characterizing the "island of stability" of the superheavy elements. Nuclei with magic numbers of protons and neutrons are analogous to the noble gases in case of atoms, i.e. they represent a closed shell configuration and a spherical shape. After a shell is filled there is an energy gap before the next shell, making magic nuclei especially stable systems. A realistic form of the nuclear potential is the Woods-Saxon potential:

$$V(r) = \frac{-V_0}{1 + e^{\frac{r - R_{\mathrm{av}}}{a}}} \ , \tag{2.1}$$

where V_0 is the depth of the potential well, R_{av} the mean radius of the nucleus and a the skin thickness, describing the diffuseness of the surface of the nucleus. This alone turns out to be insufficient to produce the observed energy levels and spacings. In addition, one must introduce a spin-orbit term analogous to atomic physics where the spin-orbit interaction (the interaction between the electron's magnetic moment with the magnetic field generated by its orbital motion) accounts for the observed fine structure in the energy levels. In the nuclear case though the interaction is much stronger (too strong in fact to be of electromagnetic origin) and opposite in sign, but it nevertheless produces the observed level spacings and magic numbers. The orbitals are labelled according to quantum numbers nl_j, where n = 1, 2, 3,... is the number of a given l state, l = s, p, d, f, g, h, i,... describes the orbital angular momentum in the spectroscopic notation (the corresponding quantum numbers are l = 0, 1, 2, 3, 4, 5, 6,...), and j is the total angular momentum quantum number of the orbital. The degenaracy of an orbital, i.e. the maximum number of protons or neutrons the orbital can contain is $2j + 1$. This is due to the possible values of magnetic substates being $m_j = -j,..., j$.

In the shell model approach only quite light nuclei can be treated such that all the constituent nucleons are taken into account. In heavier nuclei the nucleons filling the orbitals up to the last closed shell are treated as an inert core and the remaining valence nucleons then give rise to the observed energy levels. A schematic representation showing the evolution of shell model energy levels with different potentials is shown in figure 2.1. The spherical shell model works well in describing nuclei close to the closed shells defined by the magic numbers. As an example, the spin and parity of ^{209}Bi ($Z = 83$ and $N = 126$) is observed to be $9/2^-$, as would be expected based on figure 2.1. Indeed, the $9/2^-$ state has been observed to be the ground state even in such extremely neutron deficient nuclei as $^{191}_{83}\mathrm{Bi}_{108}$ studied in this thesis.

2.1.2 Nuclear deformation and collective models

In addition to the single-particle excitations, the nucleus can also exhibit collective excitation modes, such as vibration and rotation. This is typical for nuclei located outside closed shells. The nuclei studied in this thesis belong to this category, as their neutron numbers lie close to the neutron midshell between magic numbers 82 and 126.

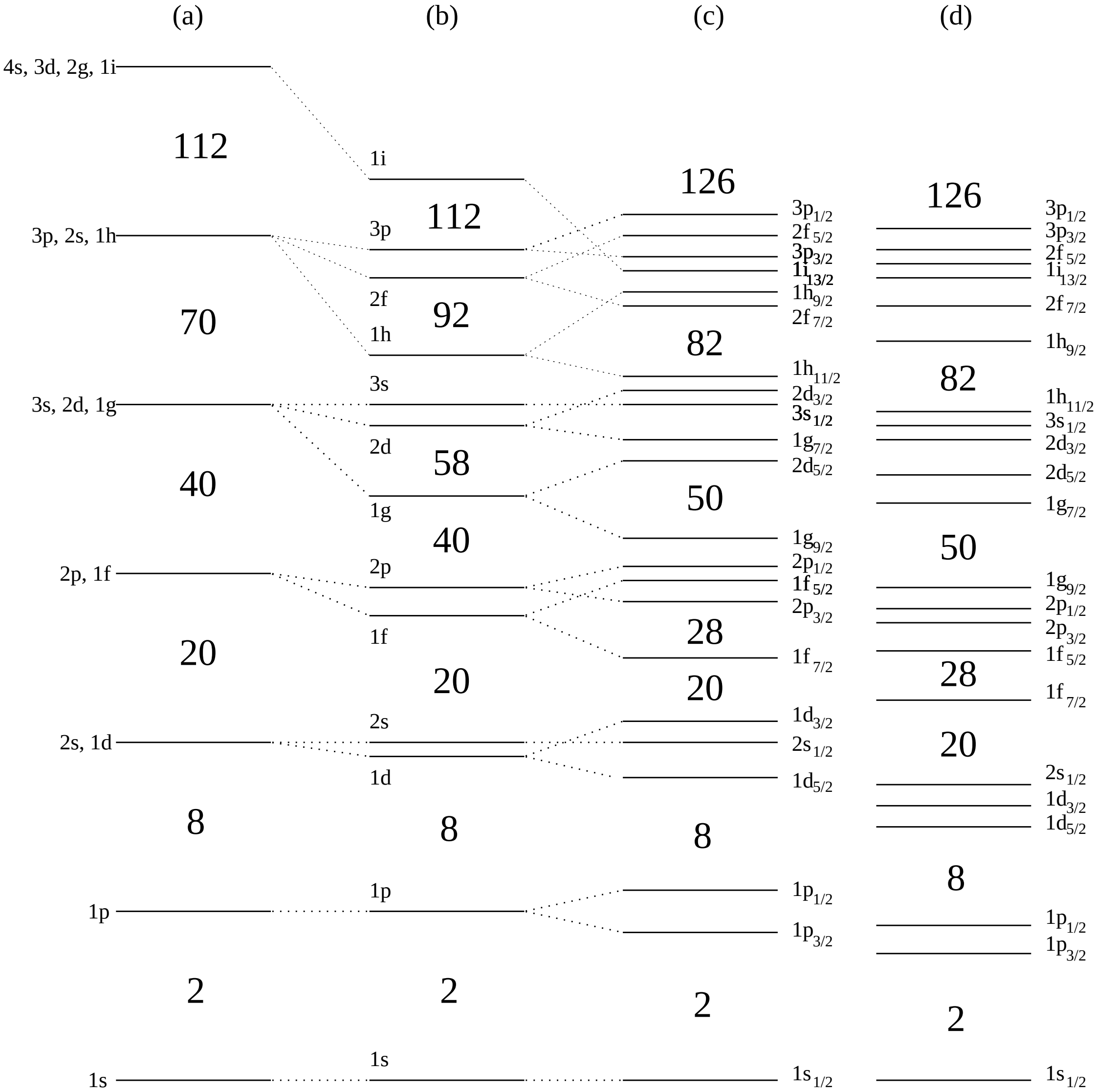

Figure 2.1: A schematic view of single-particle energy levels in various potentials relevant to nuclear structure. The energy spectrum of a simple harmonic oscillator potential is labelled with (a), followed by a Woods-Saxon potential (b) and a Woods-Saxon potential with spin-orbit interaction (c). The corresponding magic numbers are indicated between the major shells. It is obvious that the magic numbers actually observed in nuclei (2, 8, 20, 28, 50, 82, 126) emerge only with the introduction of a strong spin-orbit interaction. The last sequence of energy levels (d) displays the effect of mass of the nucleus, i.e. the increasing size of the potential well. The case presented here corresponds to a nucleus around $A \sim 190$, which is relevant for this thesis. It is notable how the level ordering changes between (c) and (d).

The proton nnumbers on the other hand ($Z = 83, 85$) lie in the vicinity of the $Z = 82$ closed shell.

Collective excitations include a time-dependent or static nuclear deformation, which can be quantified using various deformation parameters. The nuclear surface can be described in spherical coordinates by means of a spherical harmonic expansion:

$$R(\theta,\phi) = c(\alpha_{\mathrm{LM}})R_{\mathrm{av}}\left[1+\sum_{\mathrm{L=2}}^{\infty}\sum_{\mathrm{M=-L}}^{\mathrm{L}}\alpha_{\mathrm{LM}}Y_{\mathrm{LM}}(\theta,\phi)\right] , \qquad (2.2)$$

where the L = 1 terms are not included as they represent merely a displacement of the center of mass. The $c(\alpha_{\mathrm{LM}})$ factor is added to conserve the volume of a sphere with radius R_{av}. Often one can consider the case of quadrupole deformation only (L = 2). In that case it is customary to write $\alpha_{20} = \beta_2\cos\gamma$ and $\alpha_{22} = 1/\sqrt{2}\beta_2\sin\gamma$, resulting in another expression for R:

$$R(\theta,\phi,t) = R_{\mathrm{av}}\left[1+\frac{1}{4}\sqrt{\frac{5}{\pi}}\beta_2\left(\cos\gamma(3\cos^2\theta-1)+\sqrt{3}\sin\gamma\sin^2\theta\cos(2\phi)\right)\right] . \qquad (2.3)$$

The deformation parameter β_2 determines the magnitude of the deformation while the γ parameter determines the shape of the nucleus with respect to the three principal axes. Axially symmetric shapes occur at $\gamma = 0°, \pm 60°, \pm 120°$, etc. According to the Lund convention [And76] collective shapes have $-60° \geq \gamma \geq 0°$, with $\gamma = -60°$ corresponding to an oblate shape (compressed along the symmetry axis) and $\gamma = 0°$ to a prolate shape (stretched along the symmetry axis). It is worth noting that one can also describe these shapes by changing the sign of β_2, in which case $\beta_2 < 0$ is oblate and $\beta_2 > 0$ prolate. In the Lund convention β_2 is always positive.

Examples of oblate and prolate shapes are sketched in figure 2.2. The deformations have been chosen to represent the shapes of typical normally deformed and superdeformed nuclei. In superdeformed nuclei the ratio between the major and minor axes of the ellipsoid can approach 2 : 1. In normally deformed nuclei this ratio is of the order of 1.3 : 1.

Nuclear vibration

A nucleus undergoing vibrations around some equilibrium shape can be described in a similar way as equation 2.2:

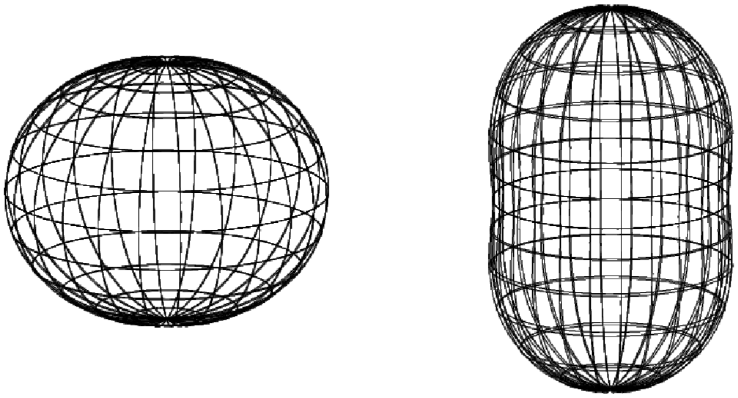

Figure 2.2: A normally deformed oblate nucleus (left, $\beta_2 = -0.2$) and a superdeformed prolate nucleus (right, $\beta_2 = 0.5$). The narrowing waist that appears in the superdeformed prolate nucleus becomes more pronounced as the deformation increases and is due to the exclusion of higher order terms in equation 2.2.

$$R(\theta,\phi) = R_{\mathrm{av}}(1 + \sum_{\mathrm{L=1}}^{\infty} \sum_{\mathrm{M=-L}}^{\mathrm{L}} \alpha_{\mathrm{LM}}(t) Y_{\mathrm{LM}}(\theta,\phi)) \ , \tag{2.4}$$

where the vibration is described by the time-dependant amplitudes $\alpha_{\mathrm{LM}}(t)$. Vibrations where the multipolarity $\mathrm{L} = 1$ are called dipole vibrations and as noted in the previous section, correspond to a translation of the center of mass of the nucleus, and therefore cannot be the result of internal forces. The next highest multipolarity, $\mathrm{L} = 2$ or quadrupole vibration, has two different modes. If the oscillation occurs along the symmetry axis (i.e. axial symmetry is preserved at all times), it is called β vibration. If the vibration occurs perpendicular to the symmetry axis, where $\gamma \neq 0°$, the vibration is called a γ vibration. In this case the instantaneous shape of the vibrating nucleus is not axially symmetric, but the average shape is.

The quantum of vibrational energy is called a phonon. Adding one $\mathrm{L} = 2$ vibrational energy quantum (a quadrupole phonon) to the 0^+ ground state of an even-even nucleus results in a state with spin and parity $I^\pi = 2^+$. Addition of two quadrupole phonons results in a triplet of states: 0^+, 2^+ and 4^+. In an idealized case these states are degenerate at an excitation energy twice the energy of the single phonon 2^+ state. The expected energy spectrum is presented in figure 2.3.

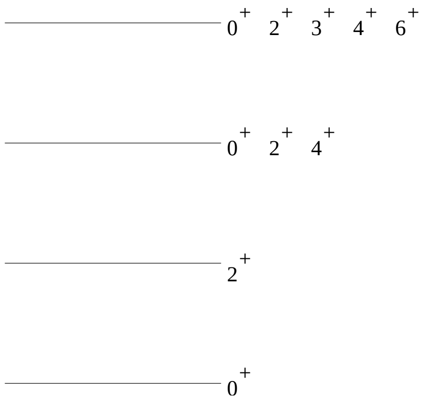

Figure 2.3: The energy levels of an ideal quadrupole vibrator. The levels forming the two-phonon triplet and three-phonon quintuplet are not exactly degenerate in real nuclei.

Nuclear rotation

Figure 2.4 shows a prolate deformed, rotating core orbited by a single valence nucleon and the various quantum numbers used to characterize the system.

The full expression for the level energies of a rotating nucleus, as given in [Boh75] for the first few K values, reads

$$\begin{aligned} E(I,K) &= E_K + AI(I+1) + BI^2(I+1)^2 + CI^3(I+1)^3 + ... \\ &+ \begin{cases} (-1)^{I+1/2}(I+1/2)(A_1 + B_1 I(I+1) + ...) & K = 1/2 \\ (-1)^{I+1} I(I+1)(A_2 + B_2 I(I+1) + ...) & K = 1 \\ (-1)^{I+3/2}(I-1/2)(I+1/2)(I+3/2)(A_3 + B_3 I(I+1) + ...) & K = 3/2 \\ (-1)^{I}(I-1)I(I+1)(I+2)(A_4 + B_4 I(I+1) + ...) & K = 2\ , \end{cases} \end{aligned} \tag{2.5}$$

where E_K is the bandhead energy, I the total angular momentum and K is the projection of the total angular momentum onto the symmetry axis. It is customary to replace the $I(I+1)$ terms by $I(I+1) - K^2$. It is important to note that the only first order correction term occurs for $K = 1/2$. The moment of inertia $\mathcal{J}$ enters the equation via

$$A = \frac{\hbar^2}{2\mathcal{J}} \tag{2.6}$$

and

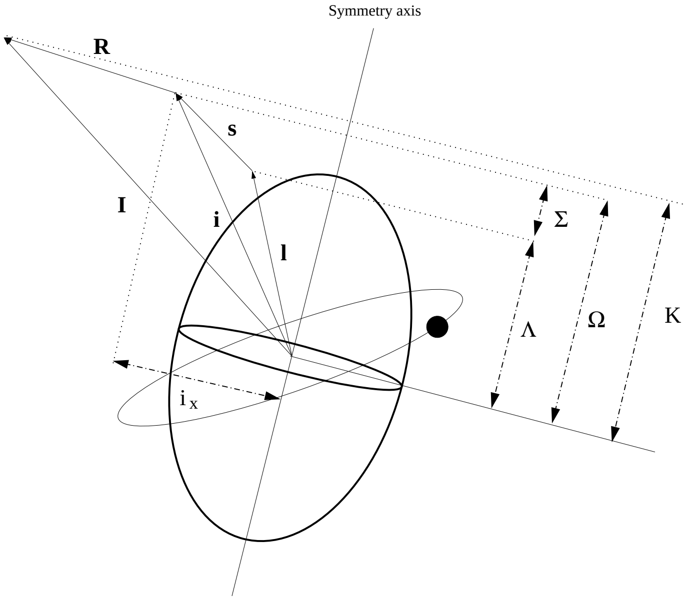

Figure 2.4: Quantum numbers used to characterize the system for a deformed, rotating core and orbiting valence nucleon. The total angular momentum quantum number, **I**, has contributions both from the valence nucleon, $\mathbf{i} = \mathbf{l} + \mathbf{s}$, and the core, **R**. In a case of several valence nucleons $\Omega = \sum_{\mathrm{i}=1}^{\mathrm{n}} \Omega_{\mathrm{i}}$. The axis of rotation is parallel to the vector **R**.

$$A_1 = \frac{\hbar^2}{2\mathcal{J}} a \ . \tag{2.7}$$

The constant a is known as the decoupling parameter. An alternative expression for the rotational energy levels is the ab-formula, which also includes the concept of a variable moment of inertia.

$$E(I) = a\left(\sqrt{1 + bI(I+1)} - 1\right) \ . \tag{2.8}$$

The substitution of the $I(I+1)$ term with $I(I+1) - K^2$ and the first order correction term for the $K = 1/2$ case can also be done with the ab-formula.

2.1.3 The Nilsson model

If the nuclear potential is not spherically symmetric, i.e. the nucleus is deformed, the simple shell model picture must be modified. This was first examined by Nilsson [Nil55]. In the Nilsson model the $2j+1$ degeneracy of the spherical case is broken, i.e. the energy of a given level depends on the component of i on the symmetry axis of the deformed core. The energy levels are labelled as $\Omega^\pi[\mathrm{Nn_z}\Lambda]$, where N is the principal quantum number of the oscillator shell, $\mathrm{n_z}$ the number of oscillator quanta along the symmetry axis (defined to be the z-axis), Λ the projection of orbital angular momentum l onto the z-axis and $\Omega = \Lambda \pm 1/2$ is the projection of total angular momentum j onto the z-axis. The levels $\Omega^\pi[Nn_\mathrm{z}\Lambda]$ are only twofold degenerate (two particles with $\pm\Omega$). The original Nilsson model was based on the anisotropic harmonic oscillator potential, with spin-orbit and l^2 terms added. Calculations have also been carried out using a more realistic, deformed Woods-Saxon potential. Plots of level energies as a function of deformation are called Nilsson diagrams, regardless of the potential used.

2.1.4 The cranked shell model

In the cranked shell model the single particle energy levels are calculated in the reference frame of the rotating, deformed core. This was first proposed by Inglis [Ing54] and later refined by Frauendorf and Bengtsson [Ben79]. The Woods-Saxon potential was included in the model by Nazarewicz a few years later [Naz85]. Analyzing data using the cranked shell model (CSM) is based on the experimental Routhian, which for even-even nuclei is defined by

$$E_\mathrm{exp}(I) = \frac{E(I+1)+E(I-1)}{2} - \omega(I)I_x(I)\ , \tag{2.9}$$

where the frequency parameter ω and x-component of angular momentum I_x are defined as

$$\omega(I) = \frac{E(I+1)-E(I-1)}{I_x(I+1)-I_x(I-1)} \tag{2.10}$$

$$I_x(I) = \sqrt{(I(I+1))^2 - K^2}\ . \tag{2.11}$$

Normally Routhians are evaluated based on a reference configuration using the quantities $e(\omega)$ and $i_x(\omega)$:

$$e(\omega) = E_\mathrm{exp}(\omega) - E_\mathrm{ref}(\omega) \tag{2.12}$$

$$i_x(\omega) = I_\mathrm{x,exp}(\omega) - I_\mathrm{x,ref}(\omega)\ . \tag{2.13}$$

Typically the quantity defined in equations 2.12 and 2.13 are called the experimental quasiparticle Routhian and alignment. The Routhian and the x-component of angular momentum for the reference configuration can be written in terms of the Harris parameters $\mathcal{J}_0$ and $\mathcal{J}_1$, [Har65]:

$$I_{\mathrm{x,ref}}(\omega) = \mathcal{J}_0\omega + \mathcal{J}_1\omega^3 \tag{2.14}$$

$$E_{\mathrm{ref}}(\omega) = -\frac{\mathcal{J}_0}{2}\omega^2 - \frac{\mathcal{J}_1}{4}\omega^4 + \frac{\hbar^2}{8\mathcal{J}_0} \; . \tag{2.15}$$

The two-fold degeneracy ($\pm\Omega$) is removed by the Coriolis and centrifugal forces under rotation when $K \neq 0$. The phenomenon is known as signature splitting.

Two quantities that measure a change in the moment of inertia are the dynamical ($\mathcal{J}^{(1)}$) and kinetic ($\mathcal{J}^{(2)}$) moments of inertia, defined as

$$\mathcal{J}^{(1)} = I_x \left(\frac{dE(I)}{dI_x}\right)^{-1} \hbar^2 = \hbar\frac{I_x}{\omega} \tag{2.16}$$

$$\mathcal{J}^{(2)} = \left(\frac{d^2E(I)}{dI_x^2}\right)^{-1} \hbar^2 = \hbar\frac{dI_x}{d\omega} \; . \tag{2.17}$$

The quantities I_x and ω are defined in equations 2.11 and 2.10.

2.2 Nuclear decay

In a decay process a nucleus transforms into another by emitting one or more particles. The emitted particle can be an electron, proton, neutron, alpha-particle, or a heavier particle. Emission of particles heavier than an alpha particle are rare. Very heavy systems can also break into two or more pieces in a spontaneous fission process. The amount of a certain radioactive species as a function of time follows the exponential decay law:

$$N(t) = N_0 e^{-\lambda t} \; , \tag{2.18}$$

where N_0 is the number of atoms in question at time $t = 0$ and the constant λ is the decay probability per unit time. The decay probability is related to the mean lifetime of the initial state (τ) and the half-life ($t_{1/2}$) by

$$\lambda = \frac{\ln 2}{t_{1/2}} = \frac{1}{\tau} \ . \tag{2.19}$$

If the decay products are also radioactive then their number as a function of time becomes

$$N(t) = N_0 \frac{\lambda_1}{\lambda_2 - \lambda_1}(e^{-\lambda_1 t} - e^{-\lambda_2 t}) \ , \tag{2.20}$$

where λ_1 and λ_2 are the decay probabilities of the first and second decaying species, respectively. These are often referred to as mother and daughter nuclei.

The most common decay processes are alpha and beta decay. Beta decay is a weak interaction process where a proton turns into a neutron or vice versa and a beta particle and a neutrino are ejected from the nucleus. The β-particle is either an electron or positron (antielectron), traditionally symbolized by β^- or β^+. β^+ decay is energetically possible only if the reaction Q-value is larger than $2m_{\mathrm{e}}c^2 \approx 1.022$ MeV. Another process called electron capture (EC) is always possible for β^+ decaying nuclei and will compete with β^+ decay. In EC an atomic electron is absorbed by the nucleus and a proton is converted into a neutron accompanied by the emission of a neutrino and X rays.

In this thesis alpha decay was used as a tool to identify different nuclei. Alpha decay is a process where an alpha particle (${}^4_2$He nucleus) forms inside the nucleus and then tunnels through the potential barrier. Consequently the proton and neutron numbers decrease by two units:

$${}^A_Z\mathrm{M}_N \rightarrow {}^{A-4}_{Z-2}\mathrm{D}_{N-2} + \alpha \ , \tag{2.21}$$

where M stands for mother nucleus and D for daughter nucleus. The total energy released in the decay, called the Q-value, is divided between the alpha particle and the daughter nucleus.

$$E_\alpha = \frac{Q}{1 + m_\alpha/m_{\mathrm{D}}} \ , \tag{2.22}$$

where m_D is the mass of the daughter nucleus and m_α that of the alpha particle. The decay will occur spontaneously only if $Q > 0$.

The alpha-decay half-life has been observed to depend, in a smooth manner, on the decay energy: the half-life in inversely proportional to the decay energy ($t_{1/2} \propto 1/\sqrt{E}$). This is known as the Geiger-Nuttal rule. A semi-empirical formula to describe the relationship between the half-life and the alpha-particle energy was introduced by Taagepera and Nurmia [Taa61]

$$\log_{10} t_{1/2} = 1.61(ZE_\alpha^{-1/2} - Z^{2/3}) - 28.9 \ , \tag{2.23}$$

where Z is the atomic number of the daughter nucleus, the half-life $t_{1/2}$ is given in years and the alpha-particle energy E_α is in MeV.

The hindrance factor, HF, is defined as the ratio of the measured half-life to a theoretical estimate, such as one calculated from equation 2.23.

$$HF = \frac{t_{1/2,\mathrm{exp}}}{t_{1/2,\mathrm{calc}}} \ . \tag{2.24}$$

If the initial and final states involved in the decay have the same spin, parity and underlying configuration the alpha decay is said to be favoured (or unhindered) and the hindrance factor is $HF < 4$. Otherwise the hindrance factor can be significantly larger.

2.3 Electromagnetic transitions

Transitions between different energy states in nuclei result in the emission of radiation. Unlike in decay processes the nucleus itself doesn't change its proton or neutron number. The energy released in the process either results in the emission of a photon or is transferred to an atomic electron. In the latter case the electron is emitted, followed by X rays when the resulting vacancy is filled.

2.3.1 Gamma-ray emission

The nuclear charge distribution can be described in terms of multipoles containing spherical harmonics. A certain multipole radiation field is labelled as σL, where σ = E means electric and σ = M magnetic field. L = 0,1,2,... is called the multipole order and the angular momentum carried away by the gamma ray equals $\mathrm{L}\hbar$. The lowest multipoles are named such that L = 0 is monopole, L = 1 is dipole, L = 2 is quadrupole, L = 3 is octupole and L = 4 is hexadecapole. In this scheme an electromagnetic transition with $\sigma\mathrm{L}$ = M1 is called a magnetic dipole transition, $\sigma\mathrm{L}$ = E2 an electric quadrupole transition and so on. Two selection rules regarding the angular momentum carried away by the photon and the parities of the initial and final nuclear states are:

$$\mid I_{\mathrm{i}} - I_{\mathrm{f}} \mid \leq \mathrm{L} \leq I_{\mathrm{i}} + I_{\mathrm{f}} \tag{2.25}$$

$$\pi_{\mathrm{i}}\pi_{\mathrm{f}} = \begin{cases} (-1)^{\mathrm{L}} & \text{for EL} \\ (-1)^{\mathrm{L}+1} & \text{for ML} \end{cases} \quad . \tag{2.26}$$

There is an important exception to the angular momentum selection rule: there are no monopole transitions in which a single photon is emitted. This means that for $I_{\mathrm{i}} = I_{\mathrm{f}}$ the lowest possible gamma ray multipole is a dipole. For a given transition energy the lowest allowed multipole is dominant.

If the spin of either the initial or final state is known then the other can be determined by identifying the multipolarity of the transition. On way this can be achieved is an angular distribution measurement. After a heavy-ion fusion-evaporation reaction the fusion products have their spins aligned in a plane perpendicular to the beam axis. If the detection angle is defined such that $\theta = 0^\circ$ corresponds to the beam direction, the variation of gamma ray intensity can be written as

$$W(\theta) = \mathrm{A}_0 + \mathrm{A}_2 P_2(\cos\theta) + \mathrm{A}_4 P_4(\cos\theta) \ , \tag{2.27}$$

where P_{k} are the Legendre polynomials and coefficients A_{k} are expressed as a product of an attenuation coefficient and the corresponding coefficient for completely aligned spins: $\mathrm{A}_{\mathrm{k}} = \alpha_{\mathrm{k}}\mathrm{A}_{\mathrm{max}}$. The details of the procedure and the necessary coefficients are presented in reference [Yam67].

Theoretical estimates for gamma-ray transition probabilities can be derived. These are called Weisskopf single particle estimates. Listed in table 2.1 are the Weisskopf estimates of transition probabilities for electric and magnetic transitions with $\mathrm{L} \leq 5$. It is important to remember that the Weisskopf estimates give the transition probability only for a gamma-ray emission. If there is significant internal conversion, the total transition probability will be the sum of the gamma-ray emission and the internal conversion transition probabilities. It should also be noted that for collective

Table 2.1: Weisskopf single particle estimates (λ_{W}) for transition probabilities. The transition energy is given in units of MeV and A is the mass number of the decaying nucleus.

σL	λ_{W} (1/s)	σL	λ_{W} (1/s)
E1	$1.023 \times 10^{14} E_\gamma^3 A^{2/3}$	M1	$3.184 \times 10^{13} E_\gamma^3$
E2	$7.265 \times 10^{7} E_\gamma^5 A^{4/3}$	M2	$2.262 \times 10^{7} E_\gamma^5 A^{2/3}$
E3	$3.385 \times 10^{1} E_\gamma^7 A^{2}$	M3	$1.054 \times 10^{1} E_\gamma^7 A^{4/3}$
E4	$1.065 \times 10^{-5} E_\gamma^9 A^{8/3}$	M4	$3.316 \times 10^{-6} E_\gamma^9 A^{2}$
E5	$2.391 \times 10^{-12} E_\gamma^{11} A^{10/3}$	M5	$7.442 \times 10^{-13} E_\gamma^{11} A^{8/3}$

transitions the transition probabilities can be several orders of magnitude larger than the Weisskopf estimates.

2.3.2 Internal conversion

Internal conversion is a process that competes with the emission of gamma rays. In this case the transition energy is transferred to an atomic electron by means of the electromagnetic multipole field. The electron is then ejected from the atom with a kinetic energy

$$T_{\mathrm{e}} = E_\gamma - B \ , \tag{2.28}$$

where B is the binding energy of the electron. The internal conversion process is followed by characteristic X-ray emission, as the vacancy left by the ejected electron is filled. The probability of internal conversion increases with increasing multipole order, decreasing transition energy and increasing atomic number of the nucleus. It also depends on whether the transition is electric or magnetic in character. The ratio between the internal conversion transition probability and the gamma-ray emission transition probability defines the total internal conversion coefficient (α) for the transition:

$$\alpha = \frac{\lambda_{\mathrm{e}}}{\lambda_\gamma} \ , \tag{2.29}$$

from which it follows that the total transition probability is

$$\lambda_{\mathrm{t}} = (1+\alpha)\lambda_\gamma \ . \tag{2.30}$$

The total conversion coefficient is the sum of contributions from different atomic shells:

$$\alpha = \sum_{\mathrm{i}} \alpha_{\mathrm{i}} \; . \tag{2.31}$$

The internal conversion process is entirely dominant in the case of E0 transitions, in which decay via gamma-ray emission is forbidden.

2.4 Features in nuclear structure around $A \sim 190$

The neutron-deficient nuclei in the $A \sim 190$ mass region are characterized by various competing nuclear shapes. Deformation at low excitation energies is driven by the excitation of protons across the $Z = 82$ shell gap [Hey83], [Woo92]. The magnitude of this gap is about 4 MeV around the closed neutron shell at $N = 126$, but decreases in energy when approaching the neutron midshell at $N = 104$. The decrease is due to the pairing force together with the attractive proton-neutron residual interaction combining to lower the energies of the particle-hole excitations. The minimum value for the energy gap occurs at the midshell where the number of interactions is maximised. In terms of the collective model these excitations manifest themselves as a macroscopic shape change of the nucleus. This can also be seen from the Nilsson diagram (figure 2.5) where the shell gaps disappear when the deformation increases due to the splitting of the spherical shell-model states. The shell model two-particle two-hole (2p-2h) and 4p-4h (or many-particle many-hole) configurations correspond in the mean field approach to oblate and prolate shapes, respectively.

The systematics of the various states that will be discussed below are illustrated in figure 2.6. Also a Nilsson diagram using a Woods-Saxon potential with universal parameters was constructed. It shows the behaviour of the various orbitals associated with these states as a function of deformation parameter β_2. The necessary computer programs, based on reference [Cwi87], were obtained from reference [Pau99]. The resulting Nilsson diagram can be seen in figure 2.5.

2.4.1 Even-even nuclei

In lead ($Z = 82$) nuclei, although the 0^+ ground states remain spherical, low-lying deformed 0^+ states have been observed. The first evidence of such states in $^{192-198}$Pb was observed when studying the β-decay of bismuth isotopes [Dup84]. In ^{190}Pb the low-lying intruder 0^+ state was first discovered in an alpha-decay experiment [Dup85].

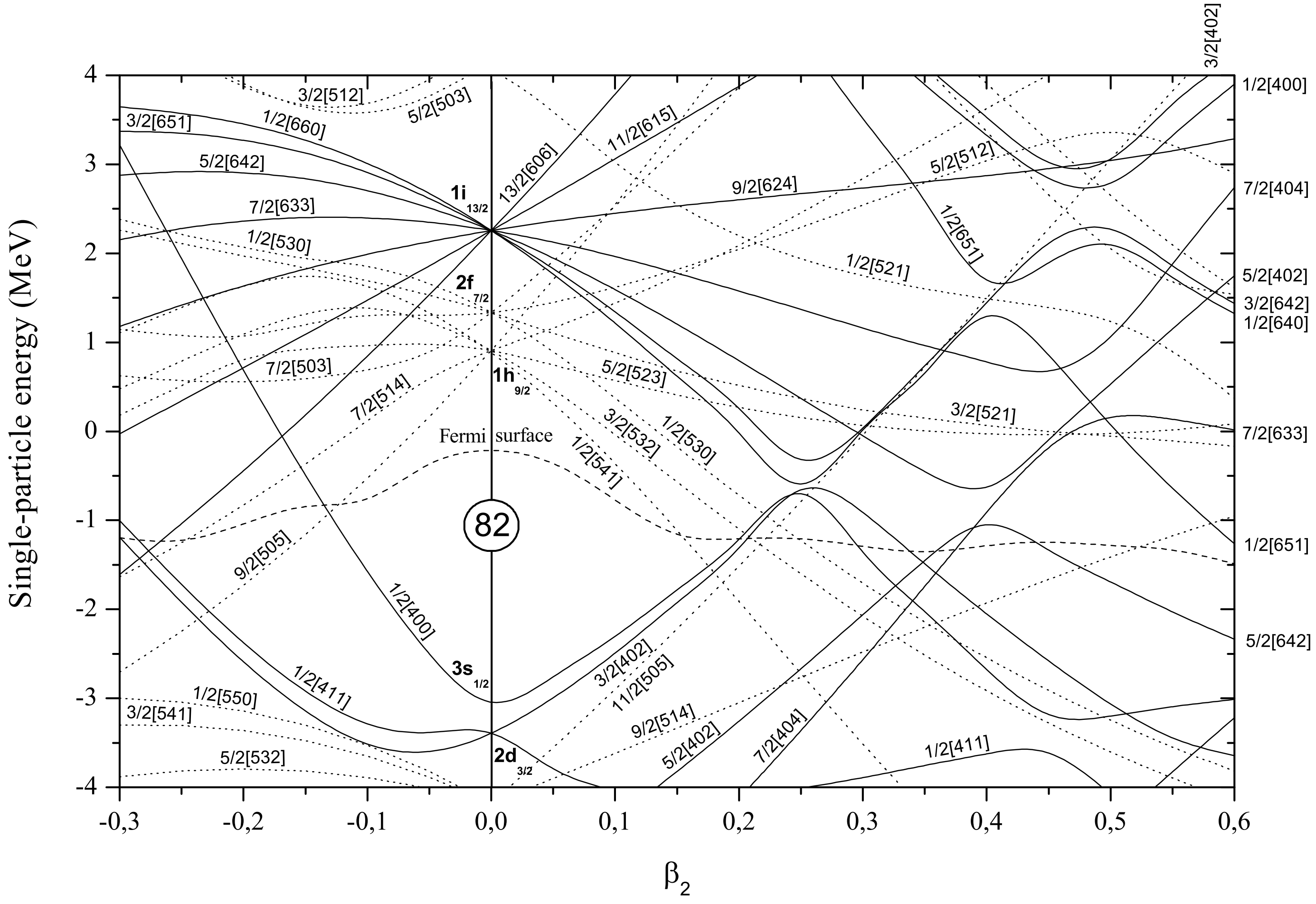

Figure 2.5: A Nilsson diagram for protons calculated using a Woods-Saxon potential for $^{191}_{83}\mathrm{Bi}_{108}$. The β_4 deformation parameter was set to zero.

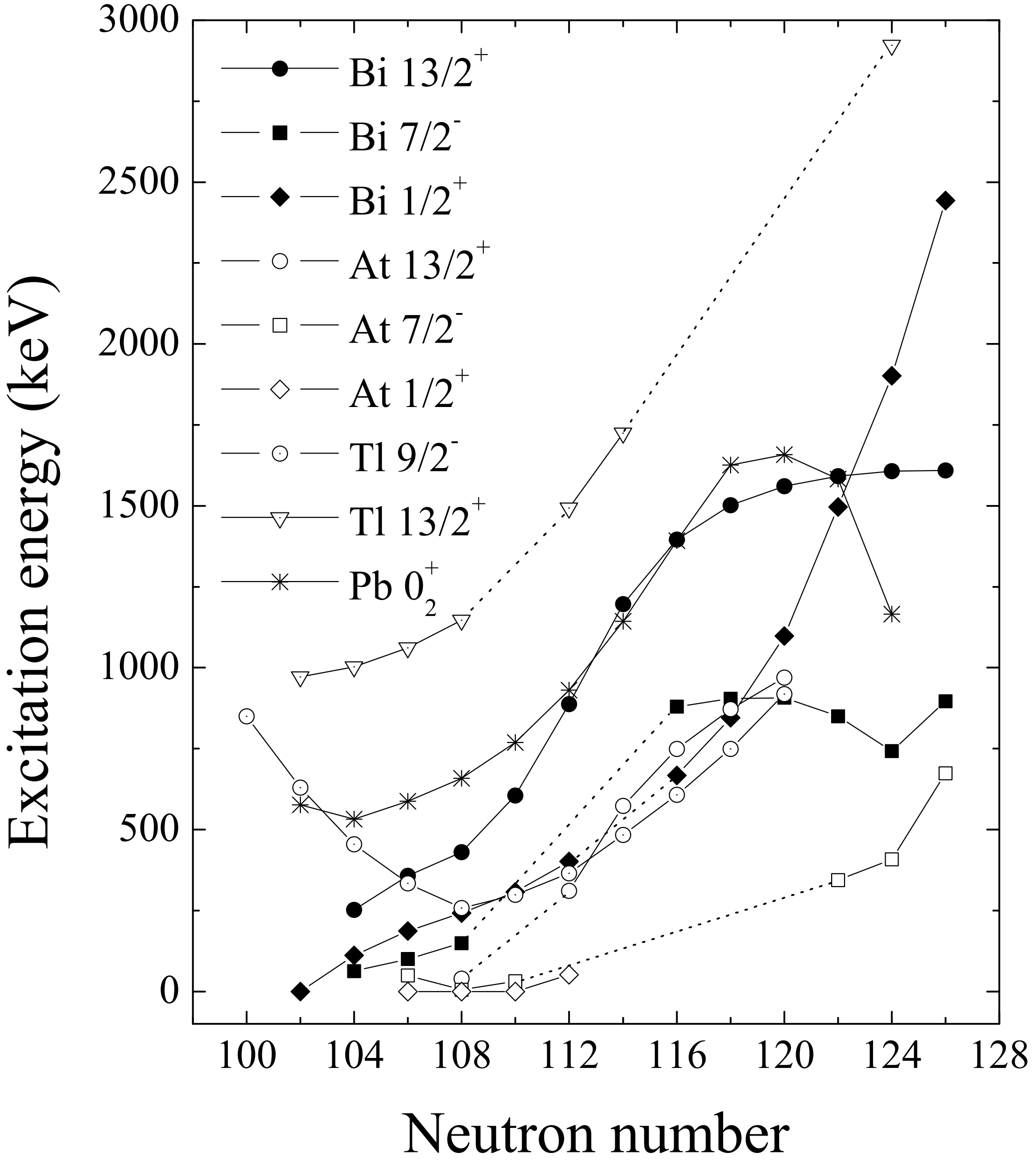

Figure 2.6: Level systematics of various low-lying levels in bismuth and astatine isotopes.

These states were interpreted as deformed two-particle two-hole (2p-2h) configurations. In ^{188}Pb the oblate 2p-2h state was first reported in [Bij96] and the prolate 0^+ state was found later [All98]. In ^{186}Pb the lowest two excited states are the oblate (532 keV) and prolate (650 keV) 0^+ states, as reported in [And00]. The verification of the shapes associated with these states requires the observation of rotational bands built on top of them. In the heavier lead isotopes, although the presence of the 2p-2h intruder states is well established from decay experiments, no cogent evidence of collective bands has been found. In ^{190}Pb some evidence of coexisting oblate and prolate configurations has been reported [Dra98] and in ^{188}Pb a possible non-yrast oblate band has also been observed [Dra04]. In the lighter isotopes $^{182-188}$Pb well developed prolate yrast bands have been discovered [Hee93] [Bax93] [Coc98] [Jen00]. Also, recently a non-yrast band has been observed in ^{186}Pb and associated with an oblate shape [Pak05b]. It should be noted that the low-lying 0^+ states are likely to be highly mixed, as predicted by IBM calculations [Fos03]. The shape coexistence and shape mixing in the neutron-deficient Pb isotopes has also been explored from a more microscopic point of view, see reference [Ben04].

In polonium ($Z = 84$) nuclei the low-lying collective bands have been assigned an oblate character down to ^{192}Po [Hel99], whereas a configuration interpreted as 6p-4h has been observed in ^{190}Po, indicating the onset of prolate deformation [Vel03] [Wis07]. The lighter Po isotopes are currently inaccessible for in-beam gamma-ray spectroscopy due to the extremely low production cross-sections. A review of multiparticle-multihole excitations in Hg, Pb and Po isotopes can be found in [Jul01].

2.4.2 Odd-even nuclei

In odd-mass nuclei the valence nucleon and its coupling to the core determines the spins and parities of the various states. Typically alpha decay is used to make these assignments, with unhindered ($HF \lesssim 4$) decays occurring between states with similar configurations.

Thallium ($Z = 81$) is the alpha decay daughter of bismuth. The ground states of all known odd-mass Tl isotopes are the $1/2^+$ states where the odd proton occupies the $3s_{1/2}$ orbital. The state can be viewed as a 0p-1h structure, as the major shell $50 \geq Z \geq 82$ is filled except for the one hole. An excited $9/2^-$ state, where the valence proton is elevated across the $Z = 82$ gap (1p-2h), exhibits a parabolic behaviour with an energy minimum close to the neutron mid-shell. Competing oblate and prolate nuclear shapes emerge in the neutron-deficient Tl isotopes, identified by the characteristic rotational band structures observed in in-beam gamma-ray spectroscopic measurements [New74] [Kre88] [Rev94] [Rev95] [Lan95]. The lowest band arises from the coupling of the $1h_{9/2}$ proton (9/2[505] Nilsson orbital) to the weakly oblate ($\beta_2 \approx 0.15$) ground state of the mercury (Z = 80) core. Competing with the $\pi h_{9/2}$ band two low-K rotational structures emerge in ^{187,189}Tl [Rev95]. These are interpreted as the coupling of the $1h_{9/2}$ and $1i_{13/2}$ protons to the prolate 0^+ states of the Hg core. These prolate 0^+ states lie at 523 keV in ^{186}Hg and at 825 keV in ^{188}Hg. The associated rotational bands have also been observed [Ma93] [Har83]. In addition to the prolate bands a decoupled low-K oblate band presumably associated with the $1h_{11/2}$ orbital has been observed in ^{189}Tl. The prolate bands are not observed in the heavier Tl isotopes, as the prolate 0^+ bandhead lies significantly higher in energy, for example at 1300 keV in the case of ^{190}Hg [Kor91]. Finally, a high-K oblate band associated with the 13/2[606] Nilsson orbital has been observed in ^{191}Tl, but not in the lighter isotopes. The 9/2[505] oblate bands in ^{189,191,193}Tl nuclei all show a backbending phenomenon due to the alignment of the spins of a $i_{13/2}$ neutron pair [Hüb86]. The alignment gain is somewhat smaller ($\Delta i_{\mathrm{x}} \sim$ 7-9 $\hbar$) in the thallium isotopes than in the core Hg nuclei ($\Delta i_{\mathrm{x}} \sim$ 11 $\hbar$). This is explained by differences in γ-softness between theTl and Hg nuclei.

In bismuth isotopes a nearly spherical $9/2^-$ state has been observed to persist as the ground state down to ^{187}Bi. This state is characterized by the valence proton occupying the $1h_{9/2}$ orbital. The odd-mass bismuth isotopes remain uncollective down to ^{195}Bi and can be understood within the shell-model framework [Lön86] [Cha86] [Pie85]. In contrast in ^{191,193}Bi strongly coupled rotational bands based on the 13/2[606] and mixed 7/2[514] + 7/2[503] Nilsson states have been observed, indicating oblate deformation [Nie04]. The collectivity of these states is presumed to originate from the coupling of the valence proton to the oblate 2p-2h intruder configuration in the Pb core.

A $1/2^+$ state, formed by exciting a proton from the $3s_{1/2}$ orbital across the Z=82 shell gap, appears at decreasing excitation energies towards and beyond the neutron midshell [Coe85], possibly becoming the ground state in ^{185}Bi [And04a]. This state is one of several possibilities for 2p-1h excitations involving the various orbitals in the $50 \leq Z \leq 82$ shell ($3s_{1/2}$, $2d_{3/2}$, $1h_{11/2}$, $2d_{5/2}$, $1g_{7/2}$). The $1/2^+$ state is the lowest energy configuration of these and is known in all odd-mass Bi nuclei with $A \leq 209$. The states involving the $2d_{3/2}$ and $2d_{5/2}$ orbitals have been observed only down to ^{199}Bi [Alp69] [Bra80]. The $1/2^+$ state follows the same steeply decreasing trend in excitation energy as the oblate 2p-2h 0^+ states in Pb nuclei down to ^{189}Bi, as can be seen from figure 2.6. The 1p-2h $9/2^-$ intruder states in Tl isotopes also display the same behaviour down to $N = 110$. However, the energies of the $1/2^+$ states in Bi then slope down, indicating that energetically a more favourable configuration comes into play. This could be a prolate 2p-1h excitation, which also lies close to the Fermi-surface, as can be observed from figure 2.1. In reference [Hür04b] it was suggested that the observed rotational band built on the $1/2^+$ state in ^{189}Bi was based on the prolate 1/2[400] Nilsson orbital.

The $13/2^+$ states are formed by exciting the odd proton to the $1i_{13/2}$ orbital. The excitation energy of these states as a function of neutron number behaves somewhat differently from that of the 2p-1h intruder states, as is evident from figure 2.6. The energy remains rather constant until sloping down steeply at $N = 116$. The energies then show signs of levelling off until another drop down occurs after $N = 106$, similar to the behaviour of the $1/2^+$ intruder states. This marks the change from oblate deformation in ^{191,193}Bi [Nie04] to prolate deformation in ^{187,189}Bi [Hür04a]. This shape change is most clearly seen experimentally in the change from strongly coupled bands in ^{191,193}Bi to decoupled bands ^{187,189}Bi where the observed rotational bands are nearly identical to those seen in the even-even lead core. Again, the collectivity observed in $^{187-193}$Bi is suggested to arise from the coupling of the $1i_{13/2}$ proton to a deformed 0^+ intruder state in the lead core.

In astatine ($Z = 85$) isotopes the 4p-1h $1/2^+$ intruder state becomes the ground state already in ^{195}At ($N = 110$) in contrast to $N = 102$ observed in the bismuth isotopes, and remains so down to the lightest known At nuclei [Ket03a], [Ket03b]. The $9/2^-$ state with the odd proton occupying the $1h_{9/2}$ orbital, which remains the ground state down to ^{197}At, is not observed at all in ^{195}At and lighter odd-mass At isotopes. Instead, a low-lying $7/2^-$ state is seen. It was proposed by Kettunen *et al.*, [Ket03a], that a configuration where the last proton occupies the 7/2[514] oblate Nilsson orbital becomes energetically favoured compared to the spherical $(\pi 1h_{9/2})^3$ configuration, thus driving the oblate $7/2^-$ state below the $9/2^-$ level. A low-lying $13/2^+$ isomeric state is also observed, with its excitation energy rapidly decreasing with neutron number $N \leq 116$, as is observed also in bismuth nuclei. This state is similar in configuration as the corresponding state in Bi, namely the odd proton coupled to the even-even polonium core.

2.4.3 Odd-odd nuclei

Odd-odd nuclei present a formidable challenge for theoreticians and experimentalists alike. This is due to the large level density produced by the multiplets of states arising from the coupling of the valence proton and neutron. Some of these states can also become isomeric. Further complicating the situation is the possible presence of collective bands based on some of these configurations.

Alpha decay studies have been used to probe the low-lying states in doubly-odd nuclei in the $A \sim 190$ mass region. The decay of odd-odd Bi isotopes has been used for systematic study of the Tl daughter nuclei [Huy88] [Dup91] [And03a] [And03b]. These studies extend down to the alpha decay of ^{184}Bi. The alpha decays of heavier elements (At, Fr) have been studied, although somewhat less data exists [Enq96] [Uus05] [And06]. A typical feature in doubly odd nuclei in this region is the presence of two low-lying alpha-decaying isomeric states, one having a relatively low spin and the other a high spin. The excitation energies of these states are usually not known, although one of them is obviously always the ground state of the nucleus in question. For example in odd-odd Bi isotopes the configurations of these states are interpreted as $(\pi 1h_{9/2} \otimes \nu 3p_{3/2})3^+$ and $(\pi 1h_{9/2} \otimes \nu 1i_{13/2})10^-$.

2.4.4 Magnetic rotation

Collective bands based on high-j isomers were found in doubly-odd Tl isotopes decades ago, see [Kre81a] [Kre81b] and references therein. These were interpreted as $\pi 1h_{9/2} \otimes \nu 1i_{13/2}$ configurations, where the proton and neutron spins were coupled perpendicular to each other. Since then collective rotation-like structures have been observed in near-spherical nuclei, the first such example being ^{199}Pb. They were initially interpreted as similar collective oblate bands [Bal92], but later the measured small values for quadrupole deformation and other peculiarities (such as $B(\mathrm{M1})/B(\mathrm{E2})$ and $\mathcal{J}^{(2)}/B(\mathrm{E2})$ ratios) of these bands [Nef95] [Cla97] led to the introduction of a new form of nuclear excitation, namely magnetic rotation. As the name indicates, this is different from the rotation of a charge distribution that constitutes a deformed nucleus, which could be called electric rotation. The underlying structure that gives rise to magnetic rotation includes high angular momentum particle and hole orbitals which, when coupled perpendicular to each other, generate a large transverse component of the magnetic moment vector. This breaks the spherical symmetry of the system and its rotation around the total angular momentum vector results in a cascade of strongly enhanced M1 transitions between levels whose excitation energy is proportional to the square of the angular momentum. The increase in angular momentum in the band is generated by the alignment of the spins of the associated particles and holes into the direction of the total angular momentum of the system. It was shown by Frauendorf, using the tilted-axis cranking model, that this coupling scheme accounts for the observed properties of the aforementioned bands [Fra93] [Fra97]. As the gradual alignment of the individual spins of the particle and hole resembles the closing of the blades of a pair of shears, the term shears band was introduced [Bal94]. In the $A \sim 190$ region shears bands have been found in various Hg, Pb and Bi isotopes [Jai00]. For a review of magnetic rotation in nuclei see reference [Hüb05].

2.4.5 Superdeformation

A deformed nucleus, as defined by equation 2.2, with the ratio between the long and short axis around 1:2 is called superdeformed. This corresponds to a β_2 value in the vicinity of 0.5. The first hints of nuclei at these very elongated shapes were related to the observation of fission isomers [Pol62] [Per62], with superdeformation proposed as an explanation by Strutinsky in 1967 [Str67]. The first discrete rotational band with characteristics of superdeformation was discovered by Twin *et al.* in ^{152}Dy [Twi86], although evidence for the existence of such bands in ^{152}Dy had been obtained earlier [Nya84] [Twi85]. Since then extensive experimental and theoretical work has been carried out and a large number of superdeformed bands have been discovered in a variety of nuclei in different mass regions ($20 \leq A \leq 240$). The fission isomers are found in various nuclei with $233 \leq A \leq 245$. The most recent compilation of data, [Sin02], lists 320 superdeformed bands and 47 fission isomers in 146 different nuclides. In the $A \sim 190$ mass region superdeformation was first found in ^{191}Hg [Moo89] and since then more than 80 bands have been discovered in various Au, Hg, Tl, Pb, Bi and Po isotopes.

One characteristic feature of superdeformation is the decay out pattern from the superdeformed (SD) states to normally deformed (ND) states. The process requires tunneling through the barrier separating the superdeformed potential well from the normally deformed one. A sufficiently high tunneling probability allows for the quantum mechanical mixing between the SD energy levels and the ND states lying at similar excitation energies on the other side of the barrier. This mixing then increases the transition probabilities to other ND states lying lower in energy. As the level density high up in the ND well is large, the decay intensity is divided between a large number of pathways, usually involving two or more steps, and can for the most part be regarded as a “quasi-continuum”. However, it is possible that some discrete transitions will carry a sufficient amount of the total intensity to be observed. In mass regions $A \sim 150$ and $A \sim 190$ it has been possible to detect these transitions in only a very few cases: ^{152}Dy [Lau02], ^{163}Lu [Jen02], ^{194}Hg [Kho96], ^{194}Pb [Lop96] and more recently in ^{192}Pb [Wil03], ^{191}Hg [Sie04] and ^{196}Pb [Wil05b]. In nuclei lighter than $A = 150$ linking transitions have been observed in numerous cases, although it is worth mentioning that some of these bands, while highly deformed, may not be associated with the SD minimum in the nuclear potential. The transitions linking the SD and ND states are typically high energy (> 2 MeV) and low intensity, making their detection challenging, even with efficient Ge-detector arrays.

The most neutron deficient lead isotope in which superdeformation has been observed is ^{190}Pb ($N = 108$) [Wil05a]. Some theoretical studies predict ^{190}Pb to be the lightest Pb isotope in which a stable SD minimum exists [Sat91] [Kri92]. In polonium nuclei ^{194}Po is predicted to be the lightest isotope having a SD minimum [Sat91]. In bismuth isotopes both experimental and theoretical data are sparse. Prior to the work presented in this thesis only three SD bands have been observed in Bi nuclei, in ^{195,196,197}Bi one assigned to each [Cla95] [Cla96].

3 Experimental techniques

In the first part of this chapter the experimental apparatus and techniques are presented. That is followed by a brief description of the data acquisition system and some remarks relevant to the analysis of data.

3.1 Fusion evaporation reactions

Producing very neutron-deficient nuclei is difficult. The production cross sections are small, typically from the region of millibarns down to nanobarns. Cross sections lower than this are too small for in-beam spectroscopy measurements with current technology. The most effective production method of neutron-deficient nuclei is the fusion evaporation reaction. In a heavy ion induced fusion evaporation reaction the beam particle and target nucleus fuse together, forming a compound nucleus which is immediately after formation at a highly excited state. The compound nucleus sheds energy by evaporating particles, followed by the emission of gamma rays. The minimum energy required to achieve fusion is determined by the Coulomb barrier between the projectile and the target nucleus. Assuming spherical nuclei this is approximately given by the equation

$$B_{\mathrm{C}} \approx \frac{Z_{\mathrm{p}} Z_{\mathrm{t}}}{A_{\mathrm{p}}^{1/3} + A_{\mathrm{t}}^{1/3}} \ , \tag{3.1}$$

where the subscripts p and t refer to the projectile and target nucleus, respectively. The height of the barrier B_{C} is obtained in MeV. The excitation energy of the compound system is

$$E^{*} = E_{\mathrm{CM}} + Q \ , \tag{3.2}$$

where E_{CM} is kinetic energy in the the centre of mass reference frame of the system:

$$E_{\mathrm{CM}} = \frac{m_{\mathrm{t}}}{m_{\mathrm{p}} + m_{\mathrm{t}}} E_{\mathrm{LAB}} \ , \tag{3.3}$$

where E_{LAB} is the energy of the projectile in the laboratory reference frame. One of the reactions used in the present work is ^{109}Ag(^{86}Kr,4n)^{191}Bi. The Coulomb barrier for this reaction, calculated using equation 3.1, is $B_{\mathrm{C}} = 184$ MeV. The excitation energy of the compound system, with a beam energy $E_{\mathrm{LAB}} = 380$ MeV, is $E^{*} = 41$ MeV.

The steps involved in the formation of a compound nucleus in a fusion evaporation reaction and its subsequent de-excitation are presented in figure 3.1. After the beam particle hits the target nucleus, a compound nucleus is formed. In the case of heavy nuclei, such as the ones studied in this work, the compound nucleus is likely to immediately undergo fission. If the compound nucleus survives without breaking apart, it releases energy by evaporating particles (neutrons, protons or alpha particles). The final product of the reaction depends on the number and type of particles evaporated, and typically there is more than one reaction channel open (such as 2n, 3n, p2n and so on). After particle evaporation the de-excitation of the fusion evaporation product continues via the emission of gamma rays. At first the gamma-ray emission occurs in a region of high level density, resulting in statistical gamma rays. Finally the de-excitation proceeds to the ground state of the nucleus mainly along the yrast line (defined by the lowest energy states for a given angular momentum). These gamma rays are the ones that can be used to extract information of the excited states of the nucleus. This whole process takes of the order of 10^{-9} s, after which the fusion evaporation product has reached its ground state (or an isomeric state). At timescales like this the fusion product, whose velocity after the impact is a few percent of the speed of light, travels a distance in the order of one centimeter. This assumes of course that the target foil is thin enough so that the fusion products are not stopped or drastically slowed down.

3.2 Experimental set-up

The ions used as projectiles in the experiments discussed in this thesis were produced using the 14.6 GHz Electron Cyclotron Resonance Ion Source (ECRIS) at the JYFL Accelerator Laboratory [Koi01]. In an ECR ion source the atoms are ionized in collisions with electrons that are heated by microwaves. The resulting plasma is confined using magnetic fields. The ions extracted from the ion source were then injected into the $K = 130$ MeV cyclotron [Hei95], accelerated to the required energy and transported to the experimental area. The measurement system consisted of the JUROGAM gamma-ray spectrometer, the gas-filled recoil reparator RITU and the GREAT focal plane spectrometer. A schematic drawing of the experimental setup is shown in figure 3.2. In the following chapters the main components of the system are briefly described.

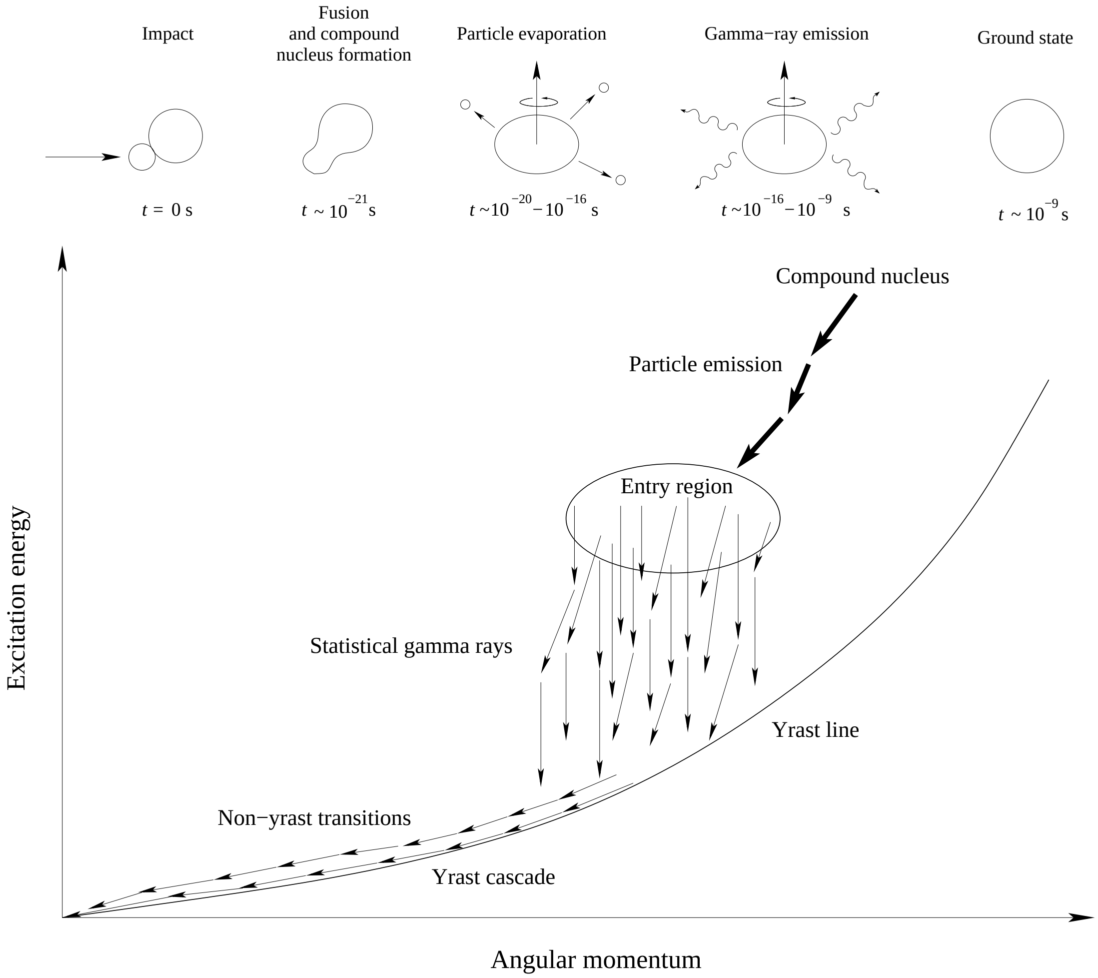

Figure 3.1: Schematic view of the steps involved in a fusion evaporation reaction and the subsequent decay of the compound nucleus. It is worth noting that the timescales characteristic of the different processes differ by several orders of magnitude.

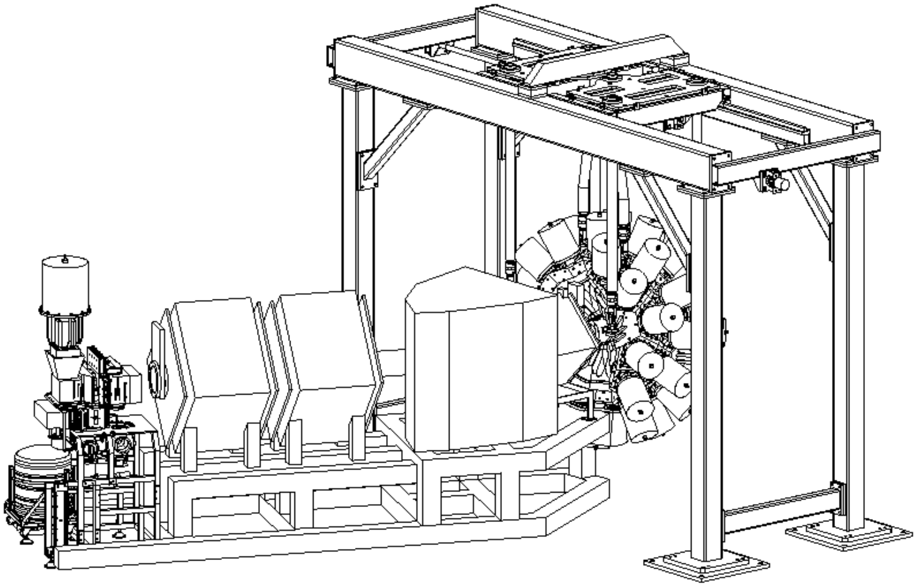

Figure 3.2: The equipment used in the present work. On the right is the JUROGAM Ge-detector array consisting of 43 escape-suppressed Ge-detectors arranged spherically around the target. The gas-filled recoil separator RITU comprising of a quadrupole magnet, dipole magnet and another two quadrupoles is located after the Ge-detector array. The ions transported through RITU are implanted in the Si-detector inside the GREAT spectrometer. A clover Ge detector is located above the GREAT vacuum chamber and a planar Ge detector is inside the chamber behind the Si detector, its liquid nitrogen dewar is visible below the chamber. The beam line is not shown. Figure courtesy of Dave Seddon, University of Liverpool.

3.2.1 The JUROGAM Ge-detector array

The detection of gamma rays using germanium detectors is based on the incident radiation liberating charge carriers the detector material. The resulting charge is the collected using an electric field applied across the detector element, which is essentially a large, reverse biased semiconductor diode. The initial free electrons that result in the ionization are produced by three principal processes: photoelectric effect, Compton scattering and pair formation. In photoelectric effect the gamma ray is absorbed by an atom and the energy transferred to an atomic electron, causing it to be ejected. Compton scattering is an inelastic scattering between the gamma ray and a loosely bound atomic electron. In the pair formation process the incoming photon is converted into an electron-positron pair. The pair production process only becomes possible with gamma-ray energies higher than 1.022 MeV.

Compton scattering results in a degraded peak-to-total value as the gamma rays escaping the detector without depositing their full energy cause a continuous structure in the low-energy part of a gamma-ray spectrum. The peak-to-total can be improved to some extent by an anti-compton shield that surrounds the Ge-detector. The shields are typically made of bismuth germanate (BGO), a scintillator material. The operating principle of an anti-Compton shield is to reject events where a signal is recorded simultaneously in the Ge-detector and in the BGO shield, indicating a gamma ray that has scattered out of the Ge crystal.

The JUROGAM array consists of 43 detector modules consisting of a HPGe (High-Purity Germanium) detector and a BGO (Bismuth Germanate) anti-Compton shield, the associated electronics, the support frame and liquid nitrogen cooling equipment. It is based on the EUROGAM I [Nol90] and EUROGAM II arrays, which were operational in 1992-1993 and in 1994-1996, respectively. The Ge-detectors used with JUROGAM are EUROGAM Phase I [Beu92] and GASP [Ros93] types. The detector modules are arranged in six rings around the target, see table 3.1. A schematic view of a GASP type detector can be seen in figure 3.3.

The detectors are collimated with lead collimators, which limits the solid angle covered by the detector. The collimators are usually equipped with 1 mm thick copper absorbers to reduce the counting rate due to X-rays. The array has a total photopeak efficiency of about 4.2 % measured at 1.332 MeV. The detectors are cooled with liquid nitrogen (LN_2) and are filled with LN_2 at 8 hour intervals. The filling system is automatic and requires relatively little human intervention during normal operations. The same system is also used for the Ge-detectors of the GREAT spectrometer. The technical details of JUROGAM are discussed at some length in [Pak05a].

In measurements where the reaction products are in motion when they emit radiation, which was the case in the present work, the Doppler effect has some consequences that

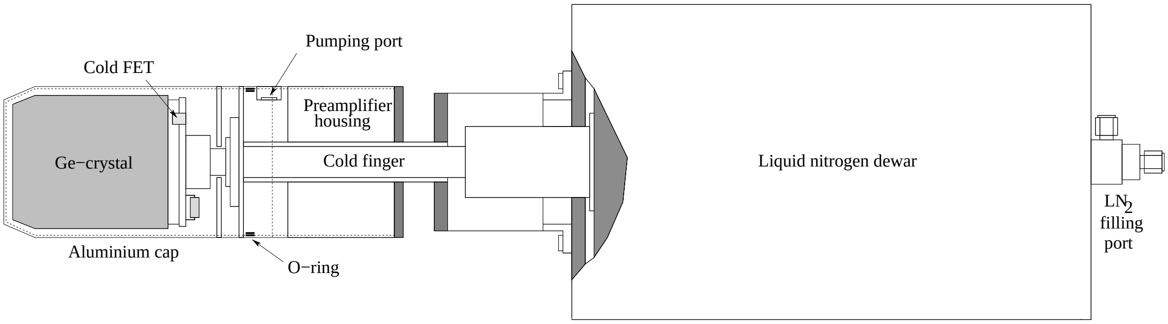

Figure 3.3: A schematic view of a GASP type HPGe detector, adopted from [Cov96]. The insulating vacuum of the dewar and the vacuum of the cryostat are connected and can be pumped through the same port. The preamplifier and associated wiring are omitted in the interests of clarity. The preamplifier is located outside the cryostat vacuum and can be accessed without venting the detector.

Table 3.1: The arrangement of detector modules in the JUROGAM array. The angle θ is measured with respect to the beam direction. The vicinity of the first quadrupole magnet of RITU makes it impossible to place detectors at small forward angles.

Ring	Number of detectors	θ (°)
1	5	157.60
2	10	133.57
3	10	107.94
4	5	94.16
5	5	85.84
6	8	72.05

need to be taken into account. The Doppler shift causes the wavelength of detected gamma rays vary between detectors at different angles with respect to the velocity vector of the nucleus. Since the detector angles in the JUROGAM array are well known, this effect can be compensated for when analyzing the gamma-ray spectra. However, since each individual detector represents a finite solid angle determined by the size of the Ge-crystal and its distance from the target area, the Doppler shifts at different parts of the detector vary. This causes a broadening of the peaks that can only be reduced by decreasing the opening angle of the detectors, i.e. using segmented Ge-crystals. In the JUROGAM spectrometer the effect of Doppler broadening is comparable to the intrinsic energy resolution of the Ge-detectors. As an example, the energy resolution for the JUROGAM array taken at $E_\gamma \sim 300$ keV was $FWHM \approx 2.2$ keV when measured from calibration data (a stationary source). From in-beam data, with the nuclei travelling at a velocity of about $0.04c$, the resolution at 300 keV was $FWHM \approx 3.2$ keV. The equations for calculating the Doppler shift and Doppler broadening are given below:

$$E_\gamma = E_0 \left(1 + \frac{v}{c}\cos\theta\right) \tag{3.4}$$

$$\Delta E_\gamma = E_0 \frac{v}{c} \Delta\theta \sin\theta \ , \tag{3.5}$$

where E_γ is the Doppler shifted gamma-ray energy, ΔE_γ the Doppler broadening, v/c the velocity of the radiation source compared to the speed of light, θ the angle of the detector with respect to the velocity vector of the source and $\Delta\theta$ the opening angle of the detector.

3.2.2 The recoil separator RITU

Recoil separators use magnetic or electric fields to separate the fusion products from the primary beam and, if possible, other reaction products. The design of these instruments is always a trade-off between mass resolving power and transmission efficiency. Typically at least one dipole magnet is used as a separating element. One way to improve the efficiency is to use low-pressure gas inside the dipole magnet [Coh58], [Ghi88]. In the following the gas-filled recoil separator RITU (Recoil Ion Transport Unit) [Lei95] is briefly described. A recent overview of gas-filled separators can be found in reference [Lei03].

RITU was originally designed for studies of heavy elements using asymmetric fusion-evaporation reactions. It has also proved successful in the studies of neutron-deficient nuclei at mass region $A \sim 110 - 190$ accessed by more symmetric reactions. The ion-optical configuration of RITU is QDQQ, meaning Quadrupole-Dipole-Quadrupole-Quadrupole. The first quadrupole focuses the fusion producs recoiling from the target in vertical direction, which matches the shape of the recoil distribution to the acceptance of the separator. This increases the transmission of the separator. The dipole magnet is the separating element and the beam is dumped inside the dipole chamber. The last two quadrupole magnets focus the reaction products exiting the dipole magnet to the focal plane of the separator.

The separator is filled with low-pressure (< 1 mbar) helium gas. The focal plane detector system is insulated from the gas by a thin mylar window, whereas the beamline upstream of the target chamber uses differential pumping to evacuate the helium, thus avoiding the necessity to use a window system. A window mounted close to the target position would increase the amount of background radiation in the JUROGAM Ge detectors. The fusion products exit the target with a wide distribution of charge states and momentum. In a vacuum mode separator the different charge states follow separate trajectories, resulting in a wide spatial distribution for the recoils at the focal plane of the separator. In practise only a few charge states can be be collected at the focal plane of the separator. A method to improve the transmission efficiency of a separator is to fill it with dilute gas. Usually, as is the case with RITU, helium is used. The ions experience a large number of charge changing collisions with the helium atoms inside the separator. The net result is that while passing through the separator the charge state of the ions fluctuate around an average charge state. Therefore the trajectories of the ions are also close to an average trajectory, thus enabling an efficient collection of fusion products.

For typical heavy-ion fusion reactions the transmission efficiency for gas-filled separators is in the vicinity of 20 % - 30 %. The downside is the lack of mass resolving power, meaning that all different isotopes produced in the fusion evaporation reaction will be transported to the separator focal plane and need to be identified by their characteristic decays. Along with the fusion products some amount of scattered beam, target like particles, protons and alpha particles will be transmitted to the focal plane.

3.2.3 The GREAT spectrometer

For the identification of fusion products of interest a sophisticated detector system is needed. The system used in the present work is called the GREAT (Gamma Recoil Electron Alpha Tagging) spectrometer [Pag03]. The spectrometer consists of various detectors, which will be briefly described in the following sections. A schematic picture of the spectrometer is presented in figure 3.4.

The Gas counter

A multiwire proportional counter (MWPC) filled with isobutane (C_4H_{10}) is the first detector downstream with respect of the beam direction from the RITU separator. The entrance window of the MWPC is 131 mm × 50 mm. The MWPC consists of an anode foil (20 μg/cm^2 aluminised mylar) and two cathode wire planes at 3 mm distance from the anode in either side. The cathode wires are 50 μm in diameter, spaced 1 mm from each other and made out of gold-coated tungsten. The normal operating voltage is 470 V. Two thin mylar windows, having a combined thickness of about 340 μg/cm^2, are used to confine the isobutane, whose pressure typically is 3-4 mbar. The ions transmitted through the separator pass through the MWPC before being implanted in the silicon detector about 20 cm downstream. The energy loss of the ions in the MWPC and the flight time between the MWPC and the DSSD can be used to distinguish fusion products from scattered beam particles. The MWPC also separates the vacuum chamber of GREAT from the helium gas inside RITU.

The implantation detector

The two double-sided silicon strip detectors (DSSD) form the core of the GREAT spectrometer. The ions transmitted through RITU and the MWPC hit the DSSD and are implanted into it, typically at a depth of about 10 μm, depending on the reaction used. The DSSDs are currently available in three thicknesses: 100 μm, 300 μm and 700 μm. The 300 μm one was used in the present work. The DSSDs are 60 mm × 40 mm in size. They have 60 vertical strips on the front side and 40 horizontal strips on the back, giving a total of 4800 pixels 1 mm^2 in size. The characteristic decays of the implanted ions can then be used to identify the different radioactive species.

The PIN diodes

Surrounding the DSSDs, on the upstream side with respect to the direction of the incoming ions, there are 28 PIN diodes. They are 28 mm × 28 mm in size, with a thickness of 500 μm. As the range of alpha particles in silicon exceeds the typical implantation depth of the recoils, some alphas escape from the DSSD and can be detected with the PINs, thereby increasing the total alpha particle detection efficiency. Alternatively they can be used to detect conversion electrons from the decays of isomeric states of the implanted recoils.

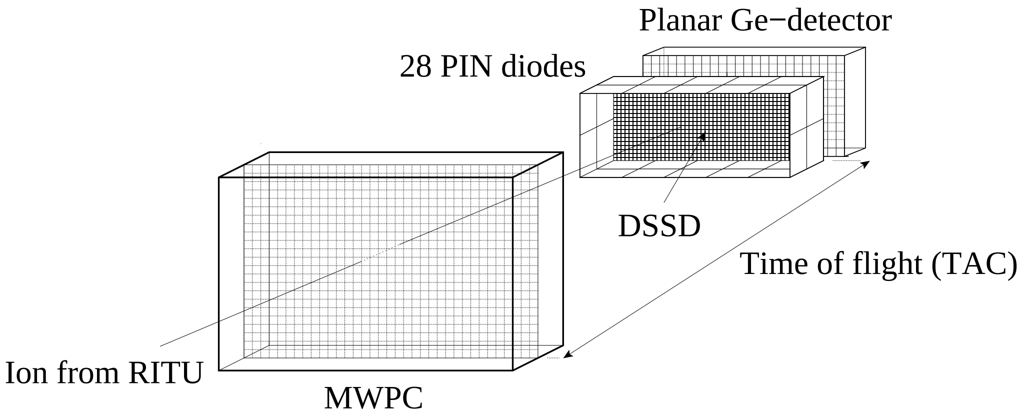

Figure 3.4: A schematic representation of the detectors the GREAT spectrometer comprised of. These detectors as well as the preamplifiers for the DSSD are housed inside the GREAT vacuum chamber. The planar Ge-detector has its own cryostat and a thin beryllium entrance window on the side facing the DSSD. The implantation detector is actually comprised of two double-sided silicon strip detectors mounted side by side. A time-to-amplitude converter (TAC) is used to measure the flight time of the ions between the MWPC and the DSSD. A large clover Ge-detector, not shown in the figure, is located outside the vacuum chamber directly above the DSSDs. Also shown is one possible trajectory for a particle exiting the RITU separator. In reality the recoil distribution covers most of the implantation detector.

The planar Ge-detector

Located at a distance of 3 mm behind the DSSD is the planar Ge-detector, which is intended for detection of X-rays and low-energy γ rays . The detector is housed inside its own cryostat and equipped with a 500 μm thick beryllium entrance window to minimize the attenuation of low-energy radiation. The size of the detector is 12 cm × 6 cm × 1.5 cm and it has 24 vertical strips on the front side and 12 horizontal strips on the back.

The clover Ge-detector

A large volume Ge-detector for detection of high energy γ rays is located above the DSSD. It consists of four n-type crystals arranged in the same cryostat in a geometry resembling a four-leafed clover, hence the name. The crystals themselves are four-fold segmented, giving a total of 16 active regions. The detector is surrounded by an anti-Compton BGO shield.

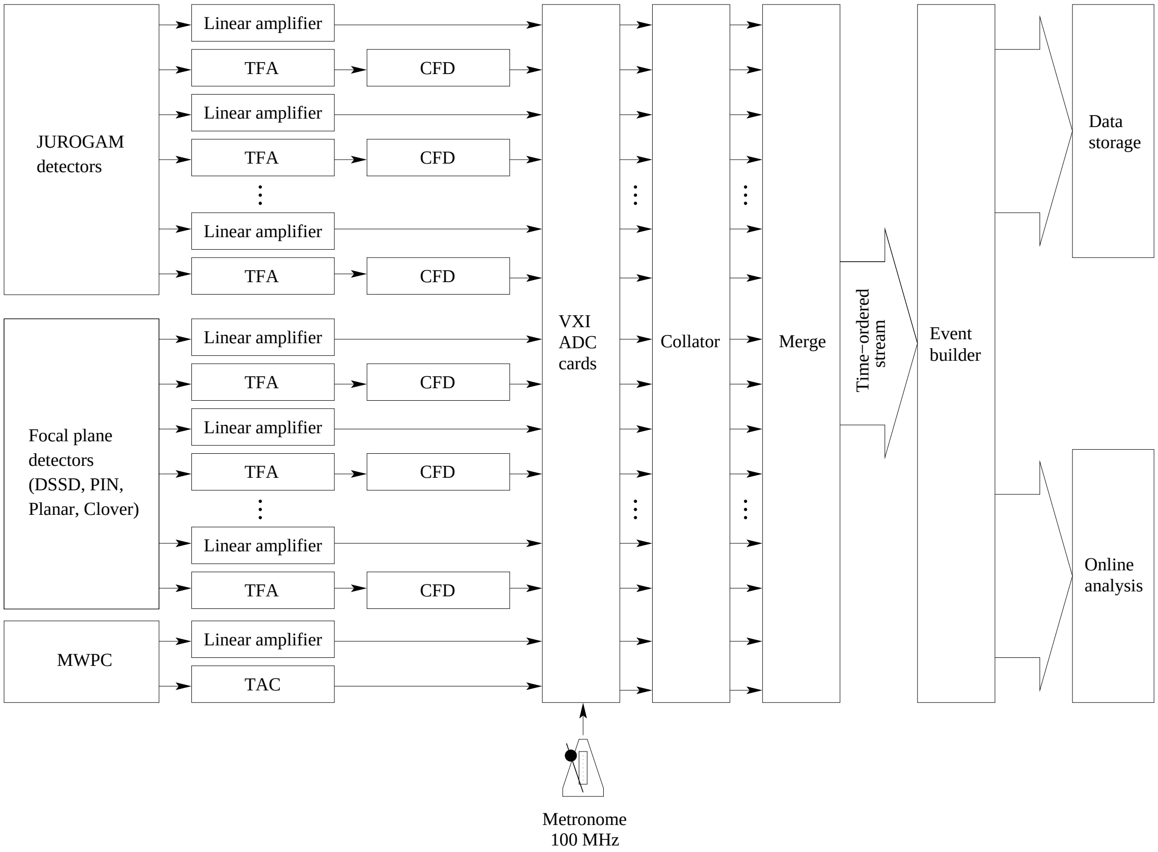

Figure 3.5: The Total Data Readout system used in the present work represented as a block diagram.

3.3 Data acquisition

The experimental set-up used in the present work employs the Total Data Readout (TDR) system [Laz01]. In a conventional system employed in tagging experiments a common hardware trigger is used to initiate a time window for data collection. New data cannot be collected during this time as the system is still processing the triggered event. This time in which the system is blocked to collection of new data is called dead time. In the TDR system the dead time problem is minimized by eliminating the hardware trigger and running all the channels independently. In this case the only contribution to the dead time comes from the processing of the individual signals. A schematic representation of the data acquisition system used in the present work is presented in figure 3.5.

The front-end electronics consists of NIM (Nuclear Instrumentation Module) and CAMAC (Computer Automated Measurement And Control) standard modules. Each electronics channel receives a signal from the preamplifier of an individual detector.

Two different signals are needed: one with information of the energy deposited in the detector and another one corresponding to the time of the event. Energy signals are processed with linear amplifiers and fed into VXI (VME eXtensions for Instrumentation) analog to digital converters (ADC). The associated timing signal is shaped by a Timing Filter Amplifiers (TFA) and a fast logic signal is then generated by Constant Fraction Discriminators (CFD) and used as a gate for the ADCs. The flight time between the MWPC and DSSD is measured using a time to amplitude converter (TAC). A 100 MHz clock is then used to timestamp the different signals. The unit that takes care of timestamping and the synchronization of the ADCs is called the Metronome module. The output of each ADC is then arranged into a time-ordered stream in the collator and the different streams are combined in the data merge unit. The resulting single time-ordered data stream is sent to the event builder where the data is pre-filtered using a software trigger. In an RDT experiment is the implantation detector OR gate, meaning that data from the JUROGAM detectors is only collected within a specific (typically 5 μs) time window preceeding any event in the implantation detector. Finally the data is sent to storage (magnetic tape or hard disk) as well as to an online analysis computer. The online and offline data sorting was done using the GRAIN software [Rah08].

3.3.1 Correlation techniques and data analysis

In order to distinguish the gamma rays belonging to a specific isotope from a vast background arising from excitation of target and beam nuclei, fission and competing reaction channels, sophisticated correlation methods are required. One must be able to distinguish the recoils from other events in the implantation detector, identify the reaction channels of interest and correlate them with the gamma rays detected at the target position in the JUROGAM spectrometer. Furthermore, in order to study the relative positions of excited states in the nuclei of interest, coincidence relationships between the gamma rays needs to be evaluated. In the following sections these steps are briefly described.

Recoil identification

The recognition of the nuclei of interest relies on the detection of the characteristic decays of these nuclei and, possibly, their decay products as well. The initial recoil identification is done based on the energy loss in the gas detector and the time-of-flight between the gas detector and the DSSD. As an example figure 3.6 shows the energy deposited in the MWPC plotted as a function of the time of flight from the reaction ^{147}Sm(^{51}V,3n)^{195}At (beam energy 232 MeV), showing the separation between recoils and scattered beam.

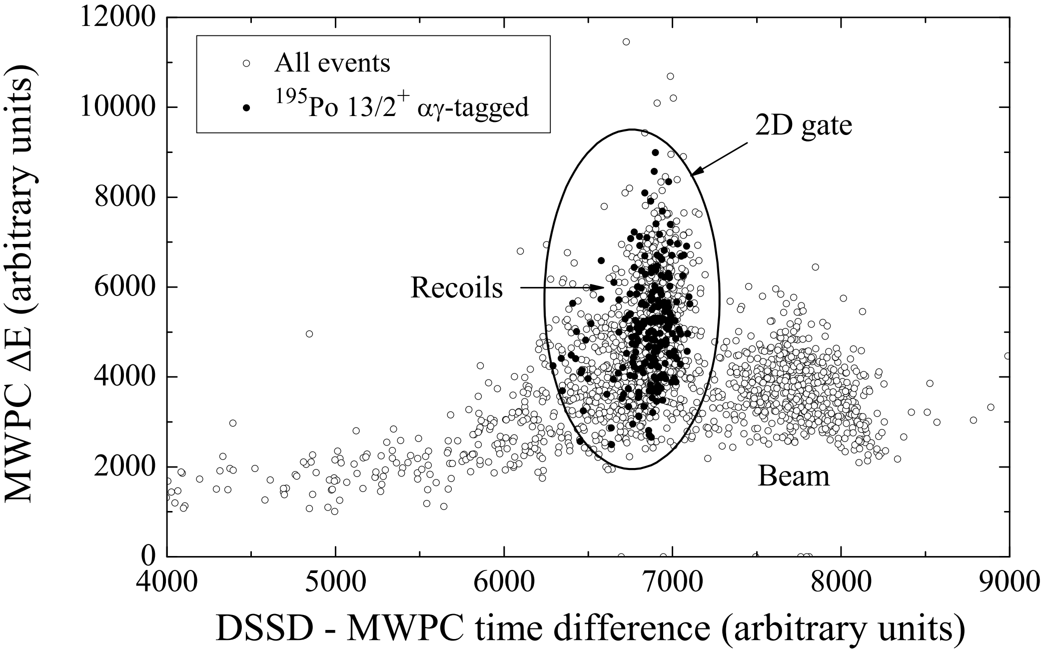

Figure 3.6: Energy loss in the MWPC as a function of time of flight between the MWPC and the DSSD, generated from data obtained in the ^{195}At experiment (reaction ^{147}Sm(^{51}V,3n)^{195}At). The two-dimensional gate used to distinguish between the fusion products and scattered beam is also shown. The most abundant fusion product in the experiment was ^{195}Po, and its known properties were used to verify the recoil distribution. The filled circles indicate events that have been correlated with the alpha decay of the $13/2^+$ state in ^{195}Po (E_α = 6699 keV) as well as an observation of a prompt 319 keV gamma ray known to feed this $13/2^+$ state. This clearly shows the region in the matrix where the fusion products are located. The data included in the figure is only a small fraction of the entire experiment, but sufficient to show the shape of the distributions.

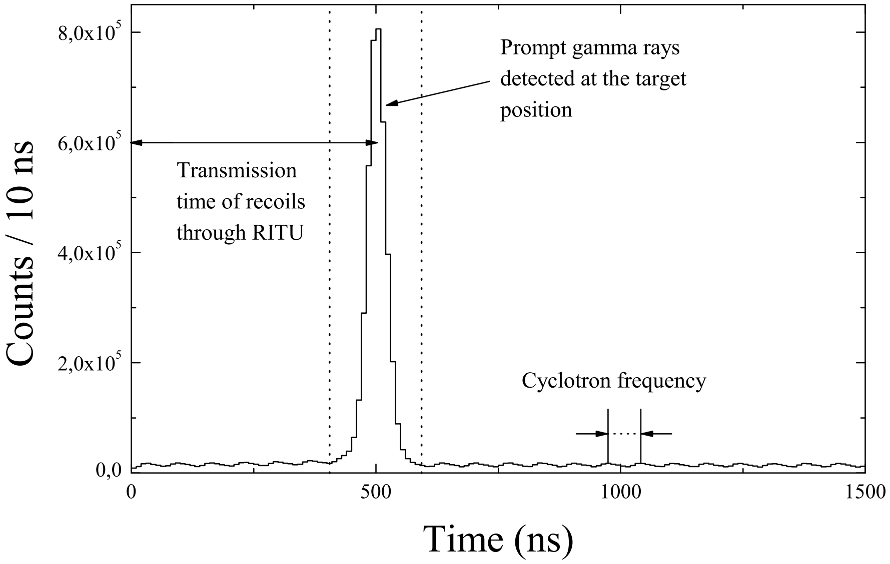

Figure 3.7: Time-of-flight distribution between gamma rays observed at the target position in the JUROGAM array and the implantation of recoils in the DSSD. The time gate applied for prompt gamma rays is indicated with the vertical dashed lines. Data is taken from the ^{191}Bi experiment.

Recoil-Decay-Tagging

After the recoil is identified, the pixellation of the implantation detector can be utilized to observe its subsequent alpha decay. As long as the counting rate per pixel is not too high compared to the half-life of the decaying nucleus, a decay event within a predetermined search time can be reliably correlated with the preceding implantation of the recoil in the same detector pixel. As an alpha decay occurring in the DSSD generates no signal in the MWPC this anticoincidence condition can be used to identify genuine decay events. Different alpha decaying nuclei can be separated by their characteristic decay energies and half-lives. Sometimes it is also possible to use the alpha decays of the daughter nuclei (recoil-alpha-alpha correlations) for further selectivity. The prompt gamma rays associated with the recoils of interest can be distinguished from the background due to the known flight time of the recoils from the target to the DSSD. A suitable time gate can be established to select the gamma rays emitted by the recoil at the target area. This technique is referred to as Recoil-Decay-Tagging (RDT). If the decay of the recoil is not used for identification the term used is recoil gating (RG). Figure 3.7 presents the time spectrum between gamma rays observed with the JUROGAM spectrometer and the implantation of recoils into the DSSD.

Half-life determination from low-statistics data

The determination of a decay half-life involves the analysis of the time distributions between the implantation of a parent nucleus and the subsequent decay events. If the available statistics is sufficient, the decay half-life can be determined by plotting the number of detected events versus decay time and fitting the exponential decay curve to that data. In the case of low statistics this method is unreliable or even impossible (an extreme case is having only one event). With low statistics the decay half-life can be determined using the method of maximum likelihood, where the life time of an activity is the arithmetic mean of the N individual life times corrected for the finite search time [Seg65]:

$$\tau = \frac{1}{\mathrm{N}} \sum_{\mathrm{n}=1}^{\mathrm{N}} \tau_{\mathrm{n}} + \frac{T}{e^{T/\tau} - 1} , \tag{3.6}$$

where the last term takes into account the effect of the finite search time, T. Using the 68.3 % confidence level, the lower and upper limits for the life time, τ_{L} and τ_{U} can be calculated from equations given in [Sch84]:

$$\tau_{\mathrm{L}} = \frac{\tau}{1 + 1/\sqrt{N}} \tag{3.7}$$

$$\tau_{\mathrm{U}} = \frac{\tau}{1 - 1/\sqrt{N}} . \tag{3.8}$$

The 68.3 % (1σ) confidence level is the one used throughout the present work.

Gamma-gamma coincidence analysis

As the fusion products rapidly de-excite by a cascade of gamma-rays, with a system composed of multiple detectors it is possible to observe two or more gamma rays from a given cascade. Gamma-rays following each other in rapid succession are said to be in coincidence with each other. As the relative ordering of excited states in a given nucleus dictate which gamma rays can be observed in coincidence and which belong to mutually exclusive decay paths, the coincidence data can be used to establish a level scheme. The coincidence analysis includes constructing a two-dimensional matrix of events consisting of two or more observed gamma rays. The coincidence relationships can then be examined by placing gates on the $\gamma\gamma$-matrix (i.e. taking slices from the two-dimensional histogram), which reveals the gamma rays detected in coincidence with the gating gamma ray. If the statistics are sufficient higher dimensional matrices can be used, such as a $\gamma\gamma\gamma$-cube. In the present work only two-dimensional matrices were used. Analysis of the gamma ray data was carried out using the RadWare software package [Rad95a], [Rad95b].

3.3.2 Calibrations

The Ge-detectors were calibrated using ^{152}Eu and ^{133}Ba calibration sources. The 16384 channel ADCs used in the system are known to have a non-linear behaviour in the lowest 10 % of the channels. The JUROGAM energy calibration therefore consists of two parts. First the relationship between ADC channel numbers and the energy deposited in the detectors was established above the nonlinear region by fitting a second order polynomial to the data obtained from the calibration sources (quadratic calibration). The nonlinear region can then be described by using the low-energy peaks from calibration data and examining the difference between the known energies and the ones obtained from the quadratic calibration. An exponential damped sine function was fitted to the data and the final corrected energy (E_{C}) reads

$$E_{\mathrm{C}} = E_{\mathrm{Q}} - ae^{-bE_{\mathrm{U}}}\sin(cE_{\mathrm{U}} + d) \ , \tag{3.9}$$

where E_{Q} is the energy obtained from the quadratic calibration and E_{U} the uncalibrated energy (i.e. the ADC channel number). The values for parameters a, b, c, d were obtained by fitting for each ADC channel individually. Figure 3.8 displays the difference between the actual energy and the noncorrected energy for one of the JUROGAM ADCs and the fitted function that is subtracted to obtain the corrected energy.

The efficiency and energy calibrations for the JUROGAM array were done using the ^{152}Eu and ^{133}Ba calibration sources. The resulting efficiency curves for the whole array and the individual detector rings can be seen in figure 3.9.

The DSSD was calibrated in the ^{195}At experiment using a three line alpha source permanently installed inside the GREAT vacuum chamber. The source consists of isotopes ^{239}Pu, ^{241}Am and ^{244}Cm. In the ^{191}Bi experiment the statistics was high enough for calibrating the DSSD strips using the alpha decay data from the experiment itself. It should be noted that when using an external calibration source one observes only the alpha-particle energy whereas in the case of an implanted nuclus the sum signal from the alpha particle and the recoiling daughter nucleus is detected.

Energy calibration for the PIN diodes was done using a ^{133}Ba conversion electron source also mounted inside the vacuum chamber. Focal plane Ge-detectors were en-

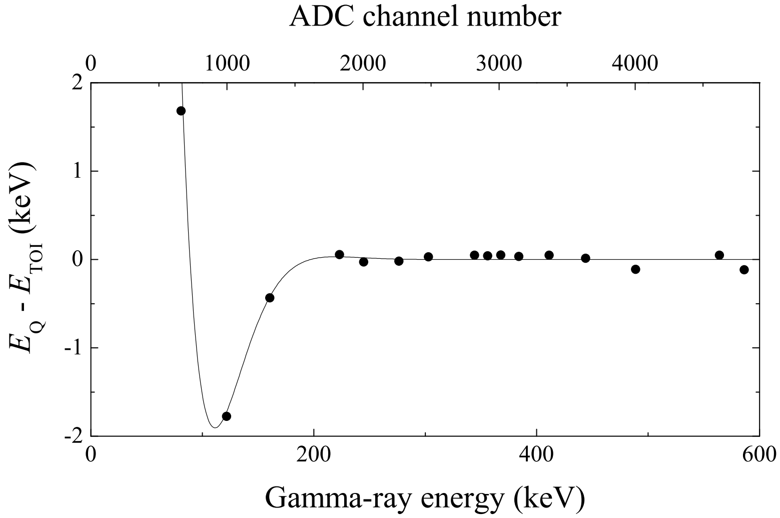

Figure 3.8: The difference between the gamma-ray energy obtained from the standard quadratic calibration (E_{quad}) and the known energy (E_{TOI}) taken from Table of Isotopes [Fir96] for one of the JUROGAM ADCs. The correction function included in equation 3.9 is also displayed.

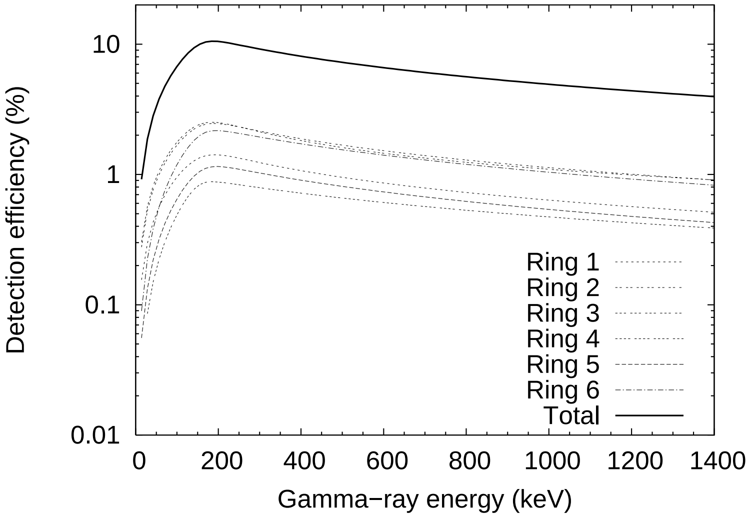

Figure 3.9: Absolute peak detection efficiency of the JUROGAM spectrometer and its constituent detector rings.

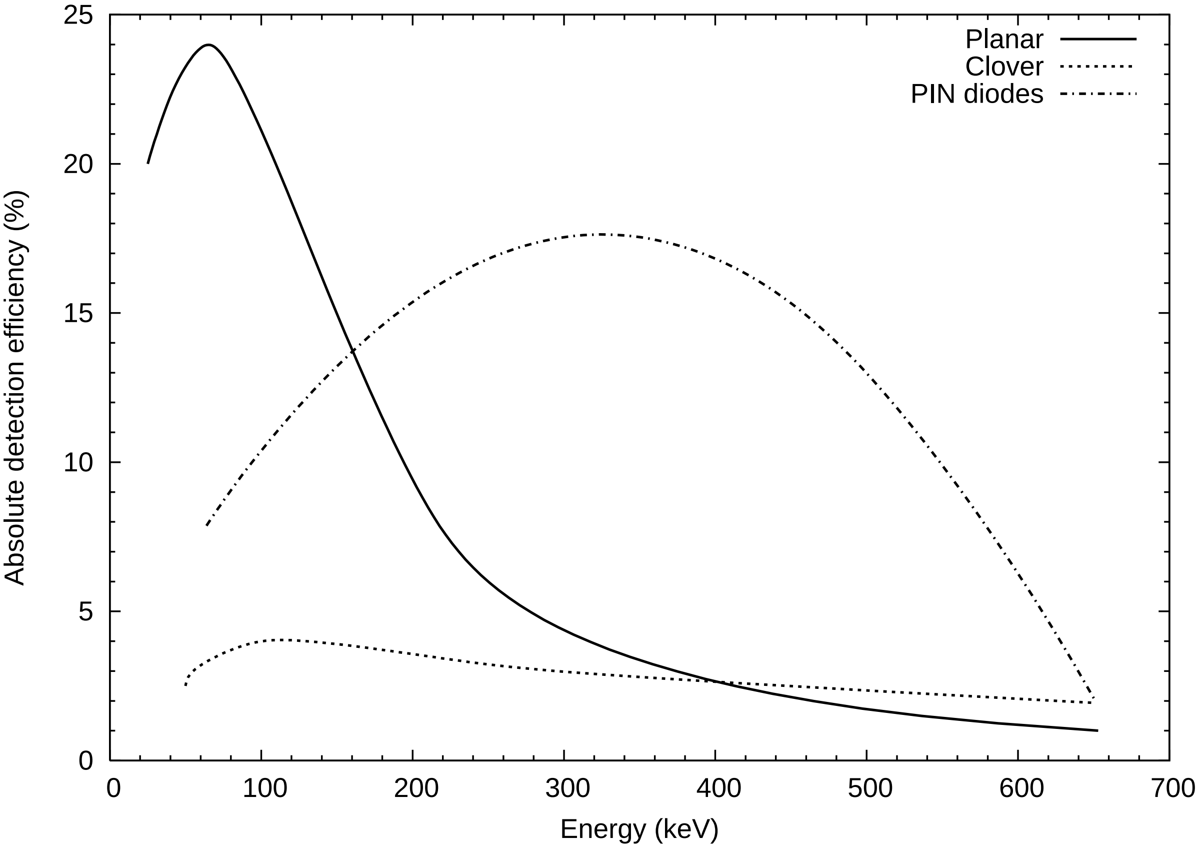

Figure 3.10: Simulated peak efficiency curves for the PIN diodes (electron detection efficiency) and the planar and clover Ge-detctors (gamma-ray detection efficiency) of the GREAT spectrometer, drawn using data taken from [And04b]. The clover is positioned outside the vacuum chamber directly above the DSSD and used in a "non-add-back" mode, i.e. each crystal works as a separate detector. This is the configuration used in the experiments discussed in this thesis.

ergy calibrated using external ^{152}Eu and ^{133}Ba sources. The efficiency calibration for the focal plane detector system relies on simulations by Andreyev [And04b]. This is because for accurate efficiency calibration the source would need to be implanted inside the DSSD similarly to the experimental conditions. This poses obvious practical difficulties. The simulated detection efficiencies of the focal plane detectors are presented in figure 3.10.

4 Spectroscopy of ^{191}Bi

The isotopes ^{191,193}Bi were studied at JYFL in an earlier experiment and the results reported in reference [Nie04]. Strongly coupled rotational bands built on the $\pi i_{13/2}$ and the mixed $\pi h_{9/2}/\pi f_{7/2}$ configurations were observed in both isotopes. Bands feeding the $1/2^+$ isomer were also observed in both nuclei. The deduced level structures of these $1/2^+$ bands were somewhat dissimilar, indicating some structural change between the two isotopes. Finally, a number of isomeric states were observed in both nuclei.

The purpose of the present experiment was to perform a detailed spectroscopic study of ^{191}Bi utilizing the improved experimental system. Some questions that remained unanswered in the previous experiment included: the level structure on top of the $1/2^+$ intruder state, the observation of the negative parity band down to its assumed $7/2^-$ band head and the possibility of a prolate $i_{13/2}$ band. The reaction used in the present experiment was ^{109}Ag(^{86}Kr,4n)^{191}Bi. The energy of the krypton beam from the K130 cyclotron was 380 MeV. Several target foils were tested during the experiment. Their thicknesses were 300, 440, 510, 530, 580 and 600 μg/cm^2. A stacked target made using the 300 μg/cm^2 and 510 μg/cm^2 foils was used for the majority of the experiment. A cross section for this reaction was estimated to be approximately 670 μb.

^{191}Bi has two alpha decaying states: the $9/2^-$ ground state ($E_\alpha = 6308(3)$, $I_{\text{rel}} = 97.0(3)$ % and $E_\alpha = 6639(5)$ keV, $I_{\text{rel}} = 3.0(3)$ %) and the $1/2^+$ intruder state lying at 242 keV ($E_\alpha = 6870(3)$ keV). The long half life of the $9/2^-$ ground state of ^{191}Bi, 12.4 s, complicates the alpha tagging technique due to the large amount of random correlations with long-lived beta decaying Pb and Tl isotopes produced in pxn and αxn evaporation channels. On the other hand, the half-life of the $1/2^+$ state, 121 ms, is very well suited for alpha tagging. The decay modes of the ground state are α-decay and β^+-decay, with the alpha branch being $b_\alpha = 51(10)$ %. The $1/2^+$ intruder state doesn't have a beta-decay branch, but has an E3 transition competing with the alpha decay. The alpha branch of the $1/2^+$ state is $b_\alpha = 68(5)$ %. The 93 keV E3 transition is not observed directly. The decay data is taken from reference [Ket03a].

The clover Ge detector was not available at the time of the experiment, so the gamma ray detection at the RITU focal plane relied solely on the planar Ge detector.

4.1 Band 1 - $\mathbf{i}_{13/2}$

The yrast band feeding the $13/2^+$ isomeric state appears in the spectrum tagged with the alpha decays of the $9/2^-$ ground state. The $13/2^+$ state decays to the ground state via a 430 keV M2 transition with a half-life of 562 ns. The total gamma-ray spectrum tagged with the alpha decays of the $9/2^-$ ground state in ^{191}Bi is presented in panel (a) of figure 4.1. While the yrast band transitions of ^{191}Bi dominate, the large background is evident from the figure. The recoil-alpha search time was 12 s.

The band built on the $13/2^+$ isomeric state was established up to spin $21/2^+$ in reference [Nie04] and the placement of levels was confirmed by analysis of the present data. The level scheme of ^{191}Bi is shown in figure 4.2. Gamma rays observed when gating with the 318 keV transition can be seen in panel (b) of figure 4.1. A candidate for the first transition to extend the band to higher spins is the peak at 385 keV. The 385 keV transition appears to be in coincidence with all the M1 transitions de-exciting the $21/2^+$ state and is thus assigned to be the $23/2^+$ to $21/2^+$ transition in the cascade. The $23/2^+$ to $19/2^+$ E2 transition at 632 keV can also be placed in the level scheme based on coincidences. The 596 keV transition is a self-coincident doublet, which together with the observation of a 212 keV transition in coincidence with the yrast band allow the placement of these two as de-exciting the $25/2^+$ state at 2195 keV. Finally, a 509 keV gamma ray can be seen in panel (b) of figure 4.1. This transition is coincident only with the 318 keV gamma ray and is thus placed to feed the $15/2^+$ level. Transitions at 468 and 494 keV appear to be in coincidence with each other, as well as with members of the yrast band from the $21/2^+$ level downwards. This can be seen clearly from panel (c) of figure 4.1. The 468 keV gamma ray is therefore proposed to feed the $21/2^+$ state with the 494 keV gamma ray placed on top of it.

Gating with the 212 keV transition reveals a cascade of low energy gamma rays: a 150 keV one and partially overlapping 162 and 164 keV transitions. A spectrum where gates on the 212 keV and 164 keV transitions are summed is presented in panel (d) of figure 4.1. The spectrum has rather large background, but the M1 transitions of the yrast cascade down from $25/2^+$ are all visible. Thus the 164, 150, 162 and (tentatively) 244 keV transitions are placed on top of that band. Their ordering is based on intensity arguments. The coincidence spectra in figure 4.1 were generated from $9/2^-$ alpha tagged gamma-gamma matrix. All the above conclusions were also verified using recoil gated $\gamma\gamma$-data.

The multipolarities of the transitions were examined by studying the angular distributions. The experimental intensity ratios $R_{\text{exp}} = I(157.60°)/I(85.84° + 94.19°)$ are listed in table 4.1. They support a dipole character for the 318, 278, 248 and 385 keV gamma rays. The calculated value for a pure $15/2 \rightarrow 13/2$ M1 transition

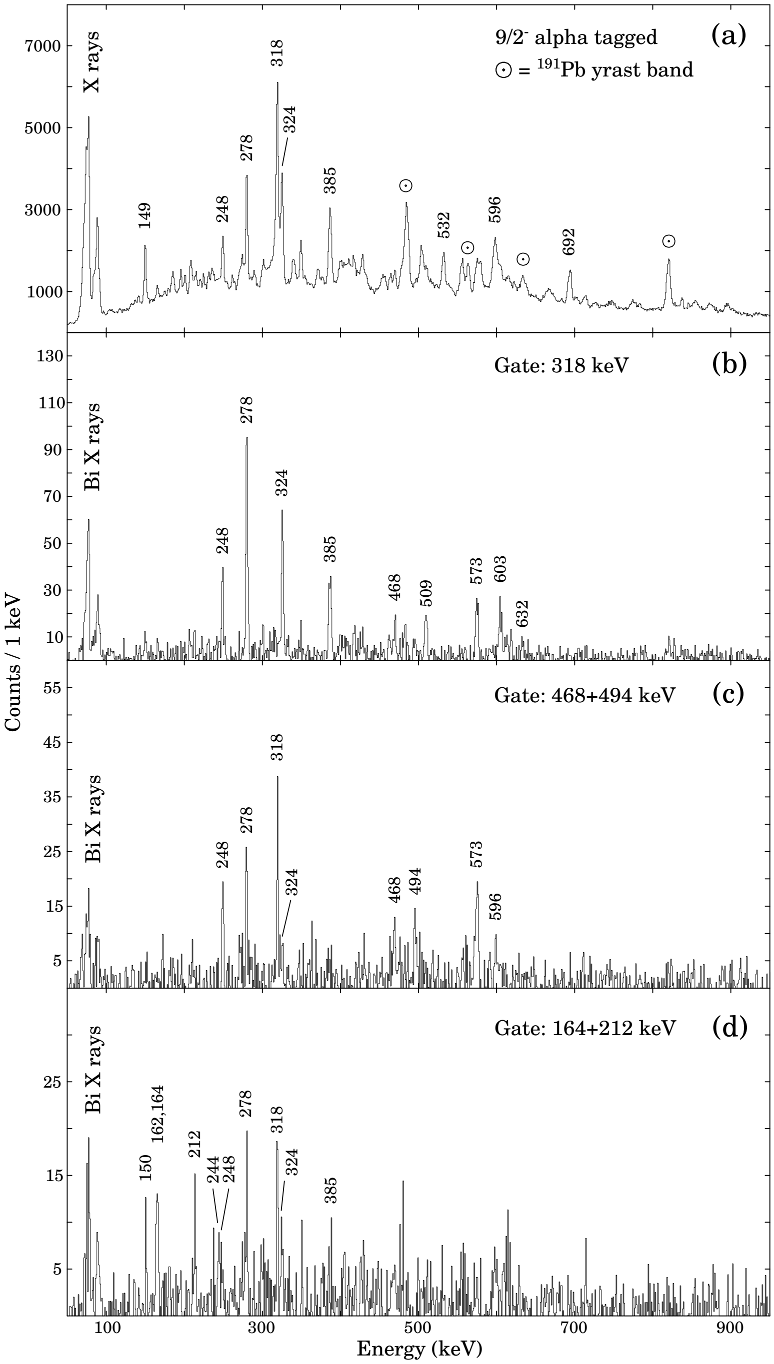

Figure 4.1: (a) Prompt gamma rays tagged with alpha decays of the $9/2^-$ ground state in ^{191}Bi. The spectrum has a large background due to the long (12.4 s) half-life of ^{191}Bi. Peaks originating from ^{191}Bi are labelled with their energies and four lowest yrast band transitions in ^{191}Pb, the most abundant background activity, are also indicated. Background peaks from other nuclei, such as ^{190,192}Pb and ^{188,189}Tl are also visible. (b) A gamma-ray spectrum gated with the 318 keV transition known to feed the $13/2^+$ isomeric state. (c) A sum of gates placed on the 468 keV and 494 keV transitions which are placed to feed the $21/2^+$ level in the yrast band. (d) A sum of gates placed on the 164 keV and 212 keV transitions placed on top of the $1_{13/2}$ band.

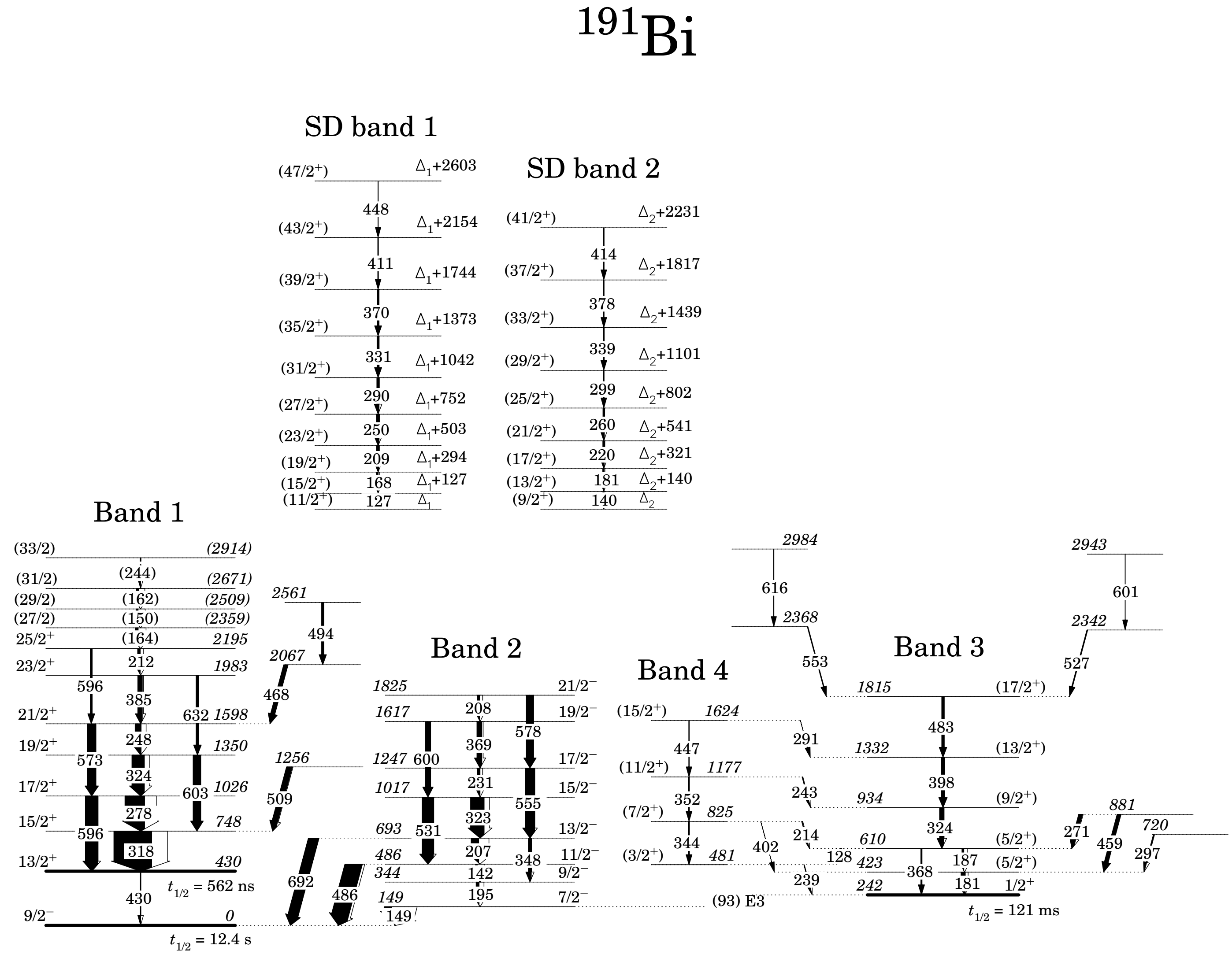

Figure 4.2: Level scheme of ^{191}Bi.

is $R_{\mathrm{theor}} = 0.67$. The theoretical value for a $17/2 \rightarrow 13/2$ E2 transition is 1.73. The theoretical values were calculated using data from reference [Yam67]. Due to the large number of closely lying lines the angular distributions of the high energy members of the band could not be determined accurately. However, based on the dipole character of the interband transitions, an E2 multipolarity is assumed.

In addition to the oblate $\mathrm{i}_{13/2}$ proton configuration, a prolate $\pi \mathrm{i}_{13/2}$ minimum is predicted to exist. These prolate bands have not been observed in ^{191,193}Bi. In the lighter isotopes ^{187,189}Bi gamma-ray cascades interpreted as prolate $\pi \mathrm{i}_{13/2}$ bands have been identified [Hür04a]. As reported in [Nie04], a tentative $21/2^+$ level in ^{191}Bi at 1736 keV was given as a possible member of the prolate $\pi \mathrm{i}_{13/2}$ band. Based on extrapolation from the lighter Bi isotopes the prolate $21/2^+$ state would be expected to lie at an excitation energy of ~1.5 MeV. In the present experiment however this $21/2^+$ level was not observed. Rather, as can be seen from the level scheme, a level at 2067 keV tentatively assigned a spin and parity of $25/2^+$ was identified. Whether this and the level observed at 2561 keV are indeed members of the prolate band need to be confirmed in a future experiment. The excitation energies, based on systematics, do support this conclusion.

Table 4.1: Measured transition energies, gamma ray intensities normalized to that of the 318 keV transition and spins and parities of the initial and final states. Also the angular distribution intensity ratios, R_{exp}, are included when their determination was possible.

E_γ (keV)	I_γ (%)	E_{i} (keV)	I_{i}^{π}	I_{f}^{π}	R_{exp}
126.6(4)	2.6(8)	$\Delta_1 + 127$	$(19/2^+)$	$(15/2^+)$	
128.3(7)	8(4)	610	$5/2^+$	$(3/2^+)$	
140.3(6)	1.9(5)	$\Delta_2 + 140$	$(17/2^+)$	$(13/2^+)$	
142.0(9)	50(20)	486	$(11/2^-)$	$(9/2^-)$	
148.5(5)	190(50)	149	$(7/2^-)$	$(9/2^-)$	0.9(3)
149.8(8)	60(30)	2509	(29/2)	(27/2)	
160.5(9)	1.5(9)	881	$(9/2^+)$	$(7/2^+)$	
162.1(14)	60(40)	2671	(31/2)	(29/2)	
164.3(8)	80(30)	2359	(27/2)	(25/2)	
167.7(4)	4.6(9)	$\Delta_1 + 294$	$(23/2^+)$	$(19/2^+)$	
180.6(5)	113(7)	423	$5/2^+$	$1/2^+$	
180.6(9)	3.5(12)	$\Delta_2 + 321$	$(21/2^+)$	$(17/2^+)$	
187.0(4)	48(5)	610	$5/2^+$	$5/2^+$	
194.6(9)	80(30)	343	$(9/2^-)$	$(7/2^-)$	1.4(6)
206.6(9)	200(60)	692	$13/2^-$	$11/2^-$	1.3(4)
208.4(9)	60(30)	1825	$21/2^-$	$19/2^-$	
208.7(3)	5.9(11)	$\Delta_1 + 503$	$(23/2^+)$	$(19/2^+)$	
212.2(9)	70(50)	2195	$(25/2^+)$	$(23/2^+)$	

Table 4.1 – Continued.

E_γ (keV)	I_γ (%)	E_i (keV)	I^π_i	I^π_f	R_exp
214.5(8)	5(3)	825	$(7/2^+)$	$5/2^+$	
214.3(10)	7(3)	934	$(9/2^+)$	$(7/2^+)$	
220.5(7)	4.1(9)	$\Delta_2 + 541$	$(25/2^+)$	$(21/2^+)$	
230.7(6)	7(4)	1247	$19/2^-$	$17/2^-$	
239.2(13)	7(2)	481	$(3/2^+)$	$1/2^+$	
243.2(10)	12(3)	1177	$(11/2^+)$	$(9/2^+)$	
243.8(11)	50(30)	2914	$(33/2)$	$(31/2)$	
247.8(5)	160(40)	1598	$21/2^+$	$19/2^+$	0.53(14)
249.5(4)	7.0(13)	$\Delta_1 + 752$	$(31/2^+)$	$(27/2^+)$	
260.1(5)	3.9(8)	$\Delta_2 + 802$	$(29/2^+)$	$(25/2^+)$	
270.9(6)	9(3)	881		$(5/2^+)$	
278.3(5)	520(90)	1026	$17/2^+$	$15/2^+$	0.68(14)
290.0(4)	6(2)	$\Delta_1 + 1042$	$(35/2^+)$	$(31/2^+)$	
296.9(11)	21(4)	720		$(5/2^+)$	
299.1(6)	1.5(12)	$\Delta_2 + 1101$	$(33/2^+)$	$(29/2^+)$	
317.7(6)	1000(150)	748	$15/2^+$	$13/2^+$	0.7(3)
323.4(6)	360(110)	1017	$15/2^-$	$13/2^-$	
324.2(4)	110(9)	934	$9/2^+$	$5/2^+$	
324.2(5)	330(70)	1350	$19/2^+$	$17/2^+$	1.1(3)
330.7(4)	5.2(15)	$\Delta_1 + 1373$	$(39/2^+)$	$(35/2^+)$	
338.7(5)	2.3(13)	$\Delta_2 + 1439$	$(37/2^+)$	$(33/2^+)$	
344.1(7)	23(3)	825	$7/2^+$	$3/2^+$	
348.0(9)	80(50)	692	$13/2^-$	$9/2^-$	0.8(3)
351.9(5)	22(4)	1177	$11/2^+$	$7/2^+$	
355.4(4)	11(3)				
368.5(14)	30(4)	610	$5/2^+$	$1/2^+$	0.8(2)
369.0(7)	130(40)	1618	$19/2^-$	$17/2^-$	
370.4(9)	4.9(15)	$\Delta_1 + 1744$	$(43/2^+)$	$(39/2^+)$	
377.6(5)	1.6(13)	$\Delta_2 + 1817$	$(41/2^+)$	$(37/2^+)$	
384.8(7)	120(30)	1983	$23/2^+$	$21/2^+$	0.50(12)
398.3(5)	87(6)	1332	$13/2^+$	$9/2^+$	
402.0(11)	<3	825	$7/2^+$	$(5/2^+)$	
410.8(5)	1.8(10)	$\Delta_1 + 2154$	$(47/2^+)$	$(43/2^+)$	
413.6(9)	1.7(13)	$\Delta_2 + 2231$	$(45/2^+)$	$(41/2^+)$	
448.3(5)	0.9(7)	$\Delta_1 + 2603$	$(51/2^+)$	$(47/2^+)$	
459.0(7)	21(3)	881		$(5/2^+)$	
468.2(6)	110(40)	2067	$(25/2^+)$	$21/2^+$	
475.3(10)	13(3)	1357			
482.8(10)	66(6)	1815	$17/2^+$	$3/2^+$	

Table 4.1 – Continued.

E_γ (keV)	I_γ (%)	E_i (keV)	I^π_i	I^π_f	R_exp
486.0(5)	450(90)	486	$11/2^-$	$9/2^-$	1.2(7)
494.0(8)	60(30)	2561	$(29/2^+)$	$(25/2^+)$	
508.7(10)	150(50)	1257			
527.0(7)	23(4)	2342		$17/2^+$	
531.3(6)	300(60)	1017	$15/2^-$	$11/2^-$	1.1(5)
542.5(5)	10(3)				
553.2(7)	18(3)	2368		$17/2^+$	
555.0(7)	250(50)	1247	$17/2^-$	$13/2^-$	0.9(3)
572.9(8)	220(40)	1598	$21/2^+$	$17/2^+$	0.8(5)
577.9(9)	190(70)	1825	$21/2^-$	$17/2^-$	1.5(9)
584.1(6)	6(2)				
594.9(6)	6(2)				
596.0(9)	330(30)	1026	$17/2^+$	$13/2^+$	0.8(4)
596.4(1.5)	50(20)	(2195)	$(25/2^+)$	$23/2^+$	
600.4(11)	140(60)	1618	$19/2^-$	$15/2^-$	
601.1(6)	4(3)	2943			
602.8(10)	200(30)	1350	$19/2^+$	$15/2^+$	
615.5(6)	6(3)	2984			
620.4(7)	5(2)				
632.0(7)	70(30)	1983	$23/2^+$	$19/2^+$	1.5(11)
692.3(5)	270(60)	692	$13/2^-$	$9/2^-$	1.3(8)

4.2 Band 2 - $h_{9/2}/f_{7/2}$

Band 2 was assigned a mixed $h_{9/2}/f_{7/2}$ character in reference [Nie04]. From the present data it was possible to confirm the level assignments up to spin 15/2 and extend the band to a $21/2^-$ level. Also, in [Nie04], the transitions down to the band head were unobserved, although a 195 keV gamma ray was tentatively placed to feed the $7/2^-$ state at 149 keV. In figure 4.3 recoil gated gamma-ray spectra with a gates placed at 207 keV and at 555 keV are shown. The peaks belonging to the negative parity band can be identified. It also appears that the 207 keV gamma ray is self-coincident. Furthermore, the 531 keV transition is also in coincidence with a gamma ray at 208 keV. A weak line at 142 keV is visible in both spectra in figure 4.3. This is assigned

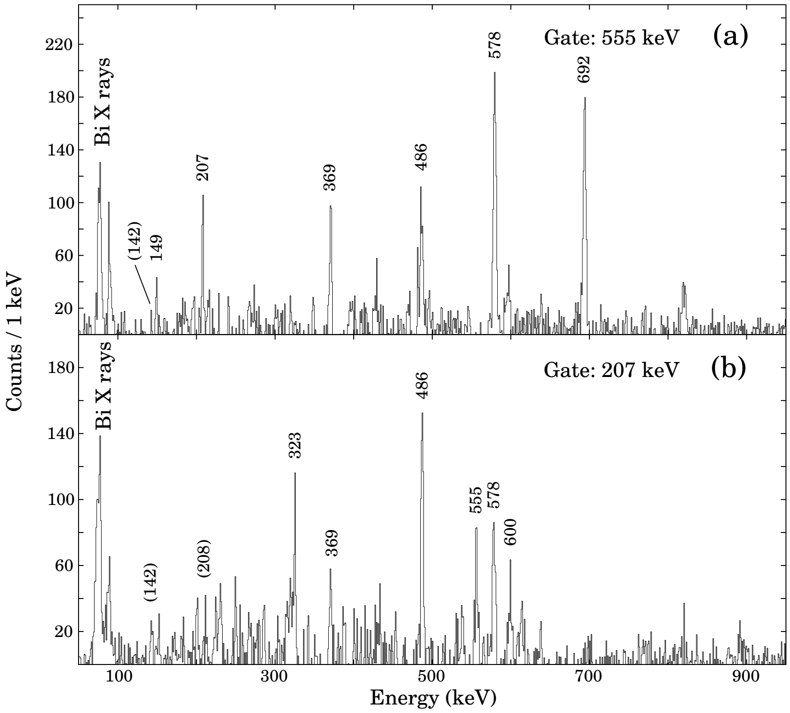

Figure 4.3: (a) Recoil gated gamma spectrum showing gamma rays in coincidence with the 555 keV transition in ^{191}Bi and (b) with the 207 keV (doublet) transition. Peaks arising from background activities can also be seen in both spectra; the ones labelled with their energies have been assigned to ^{191}Bi.

to be the $11/2^-$ to $9/2^-$ transition in the negative parity band, based both on weak coincidences and energy sum rationale. The angular distribution measurements were again hampered by overlapping gamma lines and lack of statistics.

4.3 Bands 3 and 4 - feeding the $1/2^+$ intruder state

Eight gamma-ray transitions were assigned to feed the $1/2^+$ intruder state in the previous study, but only four were placed into the level scheme. The alpha tagged singles gamma-ray spectrum from the present experiment is displayed in panel (a) of figure 4.4. The recoil-alpha search time was 500 ms. The current data was sufficient for coincidence analysis to be performed.

Panels (b), (c) and (d) of figure 4.4 present gamma-ray spectra gated with the 181, 187 and 324 keV transitions, respectively. These are placed to be the three lowest transitions in the band feeding the $1/2^+$ state, with the 368 keV transition in parallel with the lowest two. It is clear from the coincidence spectra and relative intensities that the band proceeds up to the $17/2^+$ level as depicted in the level scheme in figure 4.2. Above this the band appears to split into two parts with quite similar transition energies.

Examination of the relative X-ray intensities seen in panels (b) and (c) of figure 4.4 hints at the possibility of different multipolarities for the 181 and 187 keV transition. The fact that less X rays are seen when gating with the 187 keV gamma ray as compared to gating with the 181 keV transition suggests that the internal conversion coefficient for the 187 keV gamma ray is larger than that for the 181 keV one. This can be evaluated by examining the intensities of the 181 and 187 keV gamma rays when gating with the 324 keV transition (panel (c) in figure 4.4). This allows the conversion coefficients for the two transitions to be calculated. The results are $\alpha_{181} = 0.8(2)$ and $\alpha_{187} = 2.3(5)$. This would indicate an E2 multipolarity for the 181 keV transition ($\alpha_{\mathrm{E2},181} = 0.64$) and M1 for the 187 keV gamma ray ($\alpha_{\mathrm{M1},187} = 1.72$).

Two rather strong transitions are observed to directly feed the $(5/2^+)$ level: 297 keV and 459 keV. They establish energy levels at 720 keV and 881 keV, respectively. The 271 keV gamma ray can be placed in the level scheme based on both energy sum and coincidence arguments. Gating with the 239 keV gamma ray reveals a coincidence with 344 and 352 keV transitions. Energy sum and coincidence arguments can then be used to construct the side band as seen in figure 4.2. The tentative spin assignments are made assuming the band to be the unfavoured signature partner of the cascade built on top of the $1/2^+$ state.

The angular distribution analysis is complicated at low angular momentum by the de-orientation of the recoils [Bil86]. Therefore, nothing conclusive can be said about the multipolarities of the transitions feeding the $1/2^+$ intruder state based on this information (see table 4.1).

4.4 Superdeformed bands

A number of weak peaks in the $1/2^+$ alpha-tagged gamma-ray singles spectrum (marked with $\oplus$ in figure 5.13) are separated by approximately 40 keV, an interval in close resemblance to superdeformed bands found in some neighbouring nuclei. Panel (b) of figure 4.5 presents a spectrum with the sum of gates placed on transitions at 127, 168, 209, 250, 290 and 331 keV. It turns out that the transitions at energies 127, 168, 209, 250, 290, 331, 371, 410 and 448 keV are all mutually coincident. For the observed band to be a manifestation of a rotating superdeformed nucleus the transitions need to have an E2 multipolarity. The K X-ray intensities in panel (b) of figure 4.5 is 18(5) counts. The expected intensities for the sum gate of figure 4.5, calculated

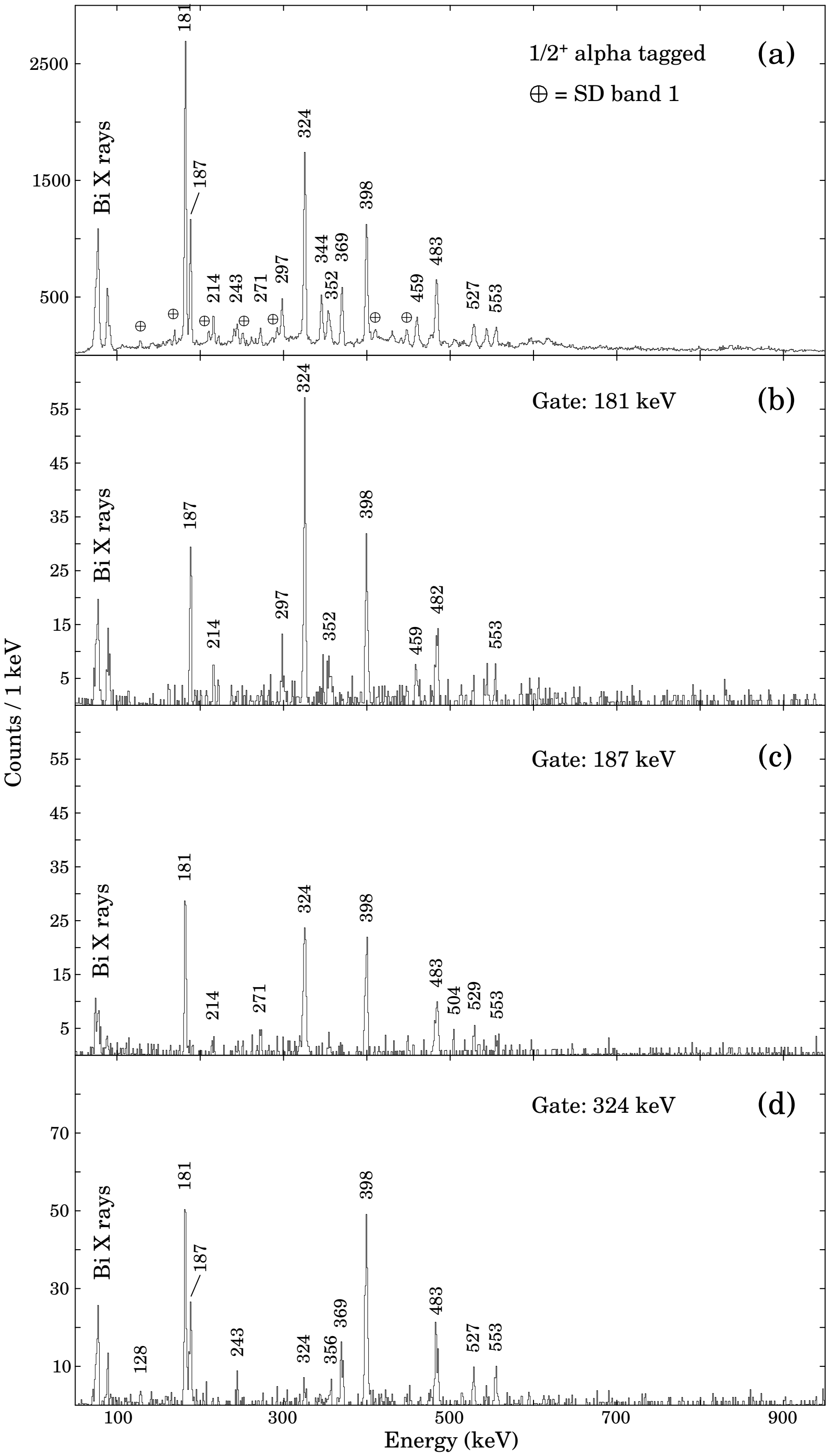

Figure 4.4: (a) Gamma rays detected with the JUROGAM spectrometer and tagged with the 6870 keV alpha decays from the $1/2^{+}$ intruder state in ^{191}Bi. (b), (c) and (d) Gamma-ray spectra gated with the 181, 187 and 324 keV transitions, respectively.

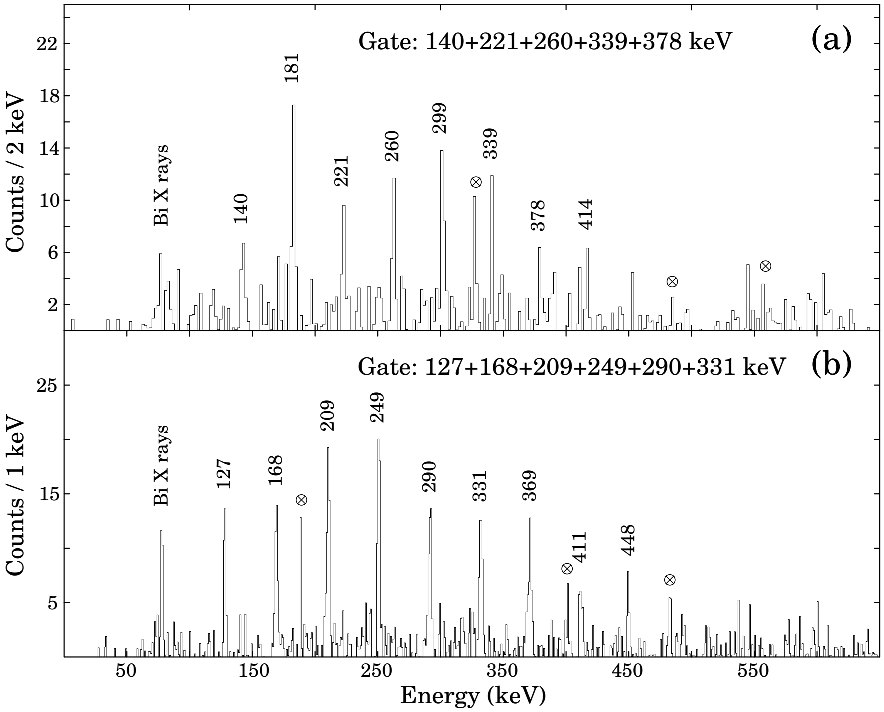

Figure 4.5: The superdeformed bands assigned to ^{191}Bi. Gamma rays feeding the $1/2^+$ state are marked in the spectra with ⊗ symbols.

based on conversion coefficients and the number of counts in the gating transitions in the $\gamma\gamma$-matrix, are 42(7) and 12(4) for M1 and E2 multipolarities, respectively. This allows the transitions in the band to be assigned an E2 multipolarity, indicating that the band indeed arises from a rotation of a deformed nucleus and not from magnetic rotation.

As can be seen from figure 4.5, some transitions feeding the $1/2^+$ state appear in the gated spectra. This not entirely unexpected as the spectra are produced by summing several gates. The presence of these transitions, marked with ⊗ symbols in figure 4.5, is due to slightly contaminated gates and background subtraction. Furthermore, these contaminant lines are different in the two spectra and the presence of the 187 keV peak but not the 181 keV one (panel (b) of figure 4.5) would not be possible in the case of a true coincidence, see the level scheme in figure 4.2.

A weaker band with transition energies of 140, 181, 221, 260, 299, 339, 378 and 414 keV can also be observed (panel (a) of figure 4.5). It is evident that there are no strong linking transitions between the bands, as no transitions from one band appear in the spectrum gated with transitions of the other band.

The absolute excitation energies of the superdeformed states can only be determined by observing the linking transitions to normally deformed states. There are typically a large number of these transitions and their energies are high, of the order of a few MeV, making their observation problematic. No evidence for such linking transitions could be found from the present data. It should also be noted that the observable energy range in this experiment only extended up to 2 MeV. It is possible that some or all of the linking transitions lie above this energy.

Another question regarding the decay out of the SD bands is whether they also feed the $9/2^-$ ground state. Unfortunately, as can be seen when comparing figures 4.1 and 4.4, the background in the $9/2^-$ alpha tagged spectrum is much larger than in the $1/2^+$ tagged spectrum due to the strong population of the $9/2^-$ state as well as the long half-life. No trace of the SD transitions are seen in the $9/2^-$ tagged spectrum, nor in $\gamma\gamma$-coincidence spectra, but it is possible that they are, if present, engulfed in the large background. Accurate determination of the decay out branching ratio for the SD bands could not be determined from the present data. Very roughly it can be estimated that more than 30 % of the SD intensity feeds the $1/2^+$ intruder state.

The superdeformed bands were found from the data obtained by tagging with the alpha decays of the $1/2^+$ state. The observation of such weakly populated bands is a manifestation of the high selectivity that can be obtained by alpha tagging. Thanks to this such a high quality gamma-ray spectrum can be produced that transitions belonging to the SD bands can be seen already in the alpha tagged singles spectrum. Also only alpha tagged $\gamma\gamma$-data was sufficient for identifying the bands. The present work is the first time a superdeformed band has been observed in a tagging experiment.

5 Spectroscopy of astatine isotopes

5.1 ^{195}At

The decay properties of ^{195}At were first reported by Yashita and Leino in the early 1980's [Yas83] [Lei83]. Combined, these two studies established two alpha-particle energies and half-lives for the alpha decay of ^{195}At. Later Enqvist *et al.* performed a more detailed study using the RITU recoil separator and found a wide energy distribution corresponding to the alpha decay of ^{195}At [Enq96]. They proposed the summing of conversion electron and alpha particle signals in the implantation detector as a possible explanation for the complicated spectrum. They were also able to measure the decay properties of the $1/2^+$ intruder state for the first time.

The results of the latest decay study of ^{195}At have been reported by Kettunen *et al.* [Ket03a]. The experiment was also performed in Jyväskylä using the RITU recoil separator. ^{195}At was produced in the fusion-evaporation reaction ^{147}Sm(^{51}V,3n)^{195}At as a side-product of an experiment aimed at studying ^{195}Rn. A decay scheme displaying the low-energy states in ^{195}At and its daughter nucleus ^{191}Bi is presented in figure 5.1. Before discussing the results from the current work a brief review of the previous results is appropriate.

The π(4p-1h) $1/2^+$ state was determined to be the ground state of ^{195}At and a $7/2^-$ state where the last proton occupies the 7/2[514] Nilsson orbital was established as the first excited state. Alpha decays from both of these states were observed. The $(\pi h_{9/2})^3$ $9/2^-$ state, which is the ground state in the heavier odd-mass astatine isotopes, was not observed. The appearance of a low-lying $7/2^-$ state was explained by a change in deformation between the three-proton configurations in ^{197}At and ^{195}At. As can be seen in the Nilsson diagram (see figure 2.5), at oblate deformations the 85th proton will occupy the 7/2[514] orbital. The unhindered alpha decay of the $7/2^-$ state also lead to the identification of the corresponding state in the daughter nucleus ^{191}Bi. Also an E3 branch between the $1/2^+$ and $7/2^-$ states in ^{191}Bi was deduced. The gamma-ray transition was not observed directly, but rather deduced from alpha-alpha correlations.

Together with the unobserved $9/2^-$ state the excitation energy of the $13/2^+$ state remains an open question. The $13/2^+$ state has been observed in both neighbouring astatine isotopes, ^{193}At and ^{197}At, as can be seen from figure 5.2. In ^{193}At it was even observed to have an alpha-decay branch, as reported in [Ket03b]. The possible decay paths of the $13/2^+$ state in ^{195}At will be discussed at length in the following sections.

The aim of the present work was to perform an in-beam (for the first time) and decay spectroscopic study of ^{195}At. Gamma-ray transitions in ^{195}At have not been previously observed. In this work the ^{195}At nuclei were produced in the fusion evaporation reaction ^{147}Sm(^{51}V,3n)^{195}At. The vanadinium beam was accelerated using the K = 130 MeV cyclotron to an energy of 230 MeV. The thickness of the samarium target foil was 750 μg/cm^2. The beam intensity was approximately 10 pnA during the experiment, with total beam on target time of $\sim$ 140 hours. The cross section for this reaction was estimated to be approximately 3 μb from the present experiment.

One of the two Double-sided Silicon Strip Detectors making up the implantation detector suffered from a degraded energy resolution during the experiment. Due to this only data from the good detector (DSSD-A) was mostly used in the analysis. Instances where data from the other detector (DSSD-B) was useful are mentioned explicitly in the text.

5.1.1 Decay spectroscopy of ^{195}At

The alpha-decay spectrum measured in the present work is presented in figure 5.3. The part of the spectrum corresponding to the decay of the $7/2^-$ state in ^{195}At is influenced by electron summing. The third peak between the 7075 keV and 7221 keV alpha peaks originates from the summing of the signals of the 7075 keV alpha particle and the K conversion electron of the following 149 keV M1 gamma decay ($E_{\mathrm{e,K}} \approx 58$ keV) [Ket03a]. The events between the 7075 keV peak and the sum peak arise from cases where the conversion electron has left only part of its energy in the detector. Lesser contributions come from higher energy L and M conversion electrons.

An alpha-alpha matrix was generated from the data collected with DSSD-A. The recoil-mother search time was 4 s and the mother-daughter search time was 80 s. The resulting matrix is presented in figure 5.4. The various groups are explained in table 5.1.

Decays of the $7/2^-$ and $1/2^+$ states

The $7/2^-$ state at 32 keV decays via alpha emission to the $7/2^-$ state in ^{191}Bi at 149 keV (E_α = 7075(4) keV, I_{rel} = 95.5(5) %) and to the $9/2^-$ ground state (e_α = 7221(4) keV, I_{rel} = 4.5(5) %) [Ket03a]. The competing E3 gamma-ray transition to the $1/2^+$ ground state in ^{195}At has not been observed previously. As the transition would be highly converted ($\alpha = 1.5 \times 10^5$) the detection of gamma rays is out of

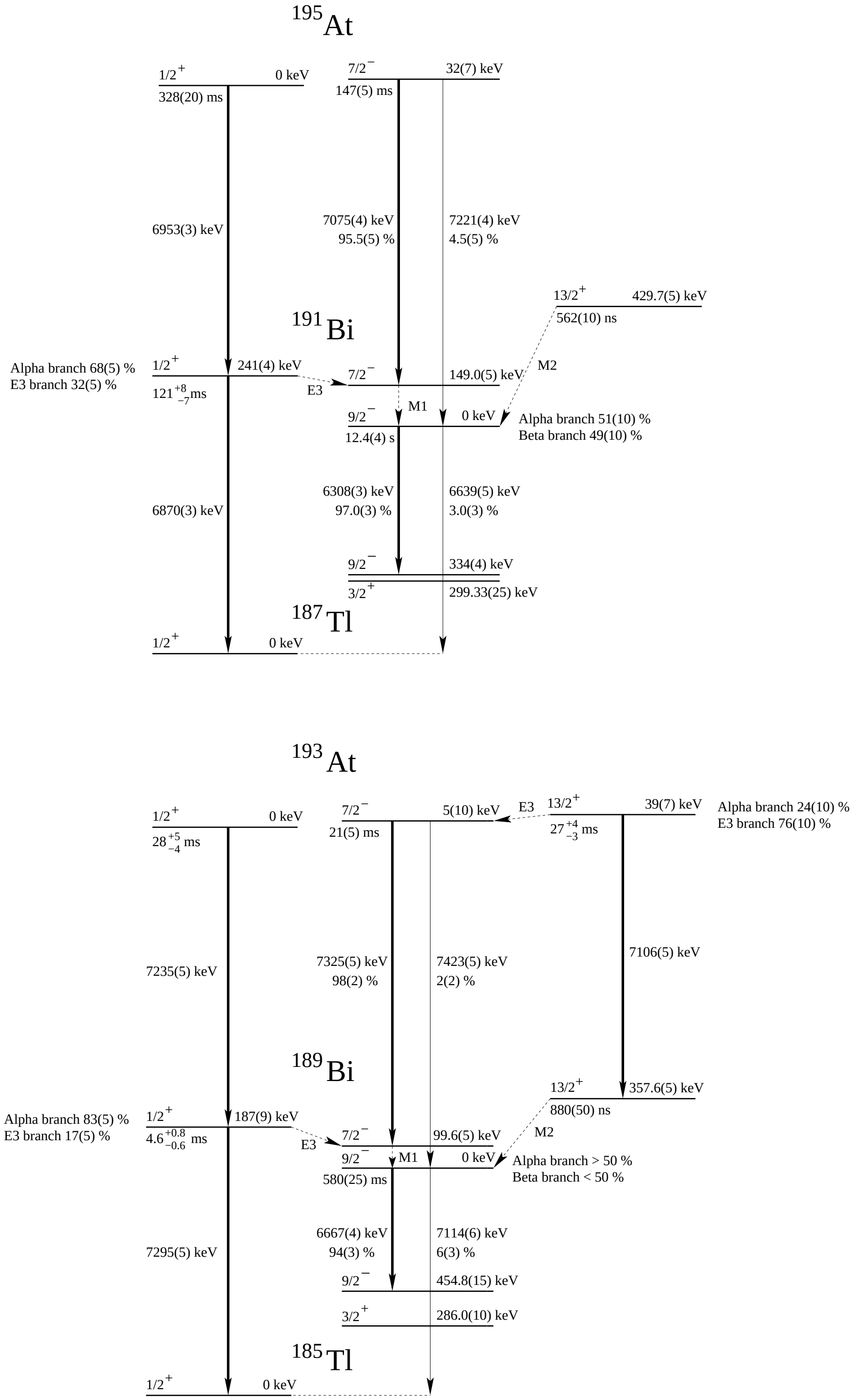

Figure 5.1: Decay schemes of ^{195}At (top) and ^{193}At (bottom) along wit their respective alpha-decay daughter nuclei. The schemes are based largely on references [Ket03a] and [Ket03b]. Additional data was obtained from [Nie04], [Van07], [Bas09] and [Wu05]. In the case of more than one alpha-decay branches from the same state, their relative intensities are given below the alpha-particle energy. If another decay mode competes with alpha decay, those intensities are written down next to the state in question; otherwise the alpha branch is 100 %.

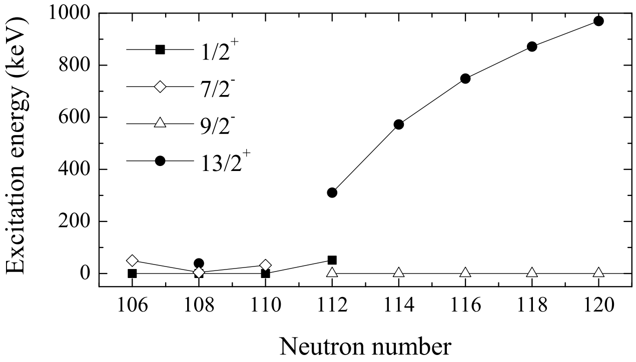

Figure 5.2: Energy systematics of the low-lying levels in odd-mass astatine isotopes. ^{195}At corresponds to neutron number $N = 110$.

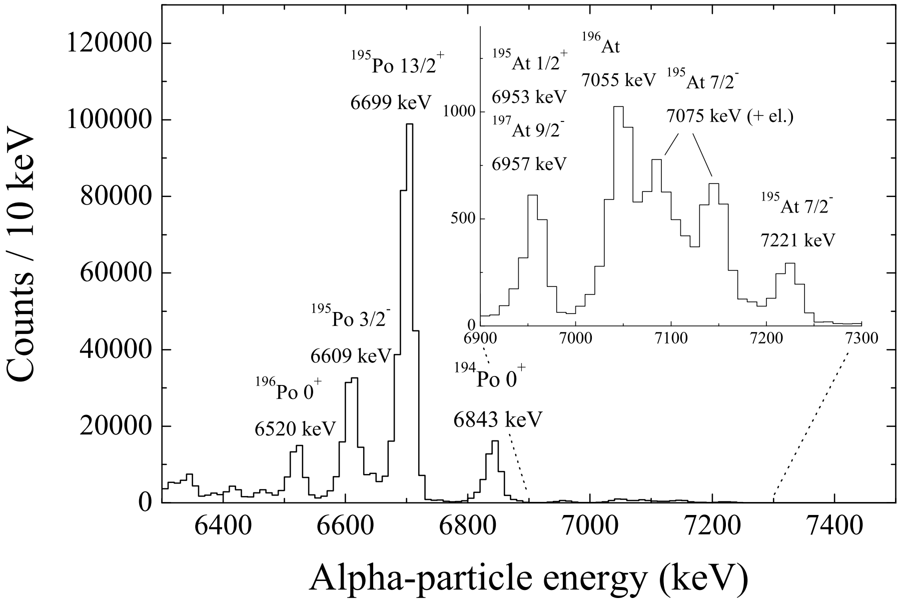

Figure 5.3: An alpha-particle energy spectrum from the reaction ^{147}Sm(^{51}V^{10+},3n)^{195}At collected with the DSSD-A detector. The origin of the three peaks in the decay of the $7/2^-$ state of ^{195}At is due to alpha-electron summing and further explained in the text. The decay of ^{194}At consists of a wide distribution of events between 7000 keV and 7300 keV. The presence of ^{197}At is due to the ^{147}Sm target also containing heavier samarium isotopes as impurities.

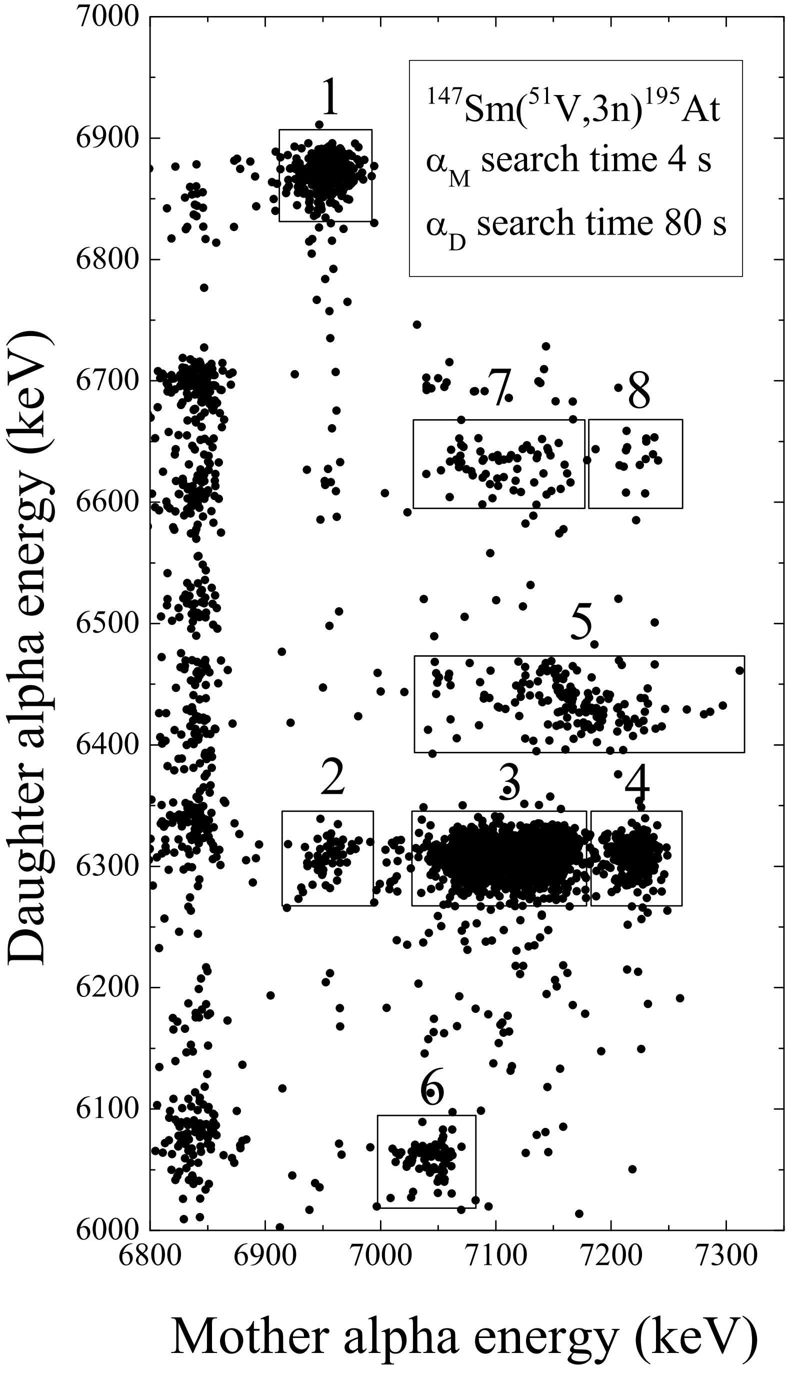

Figure 5.4: An alpha-alpha matrix from the ^{195}At experiment. The origin of the groups are explained in table 5.1.

Table 5.1: The groups observed in the alpha-alpha matrix. The spins and parities of the initial and final states involved in the alpha decays are also listed. For the odd-odd isotopes ^{194,196}At the possible spins and parities of the decaying states are discussed in chapter 6.3.

No	Mother	Decay	E_α (keV)	Daughter	Decay	E_α (keV)
1	^{195}At	$1/2^+ \rightarrow 1/2^+$	6953	^{191}Bi	$1/2^+ \rightarrow 1/2^+$	6870
2	^{195}At	$1/2^+ \rightarrow 1/2^+$	6953	^{191}Bi	$9/2^- \rightarrow 9/2^-$	6308
3	^{195}At	$7/2^- \rightarrow 7/2^-$	7075	^{191}Bi	$9/2^- \rightarrow 9/2^-$	6308
4	^{195}At	$7/2^- \rightarrow 9/2^-$	7221	^{191}Bi	$9/2^- \rightarrow 9/2^-$	6308
5	^{194}At		7000-7300	^{190}Bi		6431, 6456
6	^{196}At		7055	^{192}Bi		6060
7	^{195}At	$7/2^- \rightarrow 7/2^-$	7075	^{191}Bi	$9/2^- \rightarrow 1/2^+$	6639
8	^{195}At	$7/2^- \rightarrow 9/2^-$	7221	^{191}Bi	$9/2^- \rightarrow 1/2^+$	6639

the question. The L and M conversion electrons have energies of about 15 keV and 30 keV, respectively, which were too low to be observed in the present experiment. However, there is an indirect way to observe the E3 branch: to examine the time differences between the implantation of a recoil and the subsequent alpha decay of the $1/2^+$ state. Since the alpha-decaying $1/2^+$ state has both prompt feeding and delayed feeding through the E3 branch from the $7/2^-$ state, the recoil-alpha time distribution consists of two components (equations 2.18 and 2.20). In order to sufficiently reduce background alpha-alpha correlations were required. A recoil-alpha time spectrum was constructed from the events in group 1 in the alpha-alpha matrix (figure 5.4). The E3 branch was determined by fitting a function consisting of the two components to the data. The fraction of the $1/2^+$ state feeding proceeding via the E3 branch was extracted from the fit and the corresponding branching ratio for the $7/2^-$ state decay was then calculated. The result was $b_{\mathrm{E3}} = 12(4)$ %. It is also possible to extract the half life of the $1/2^+$ state from the fit, the result being $t_{1/2} = 290(20)$ ms. This is slightly shorter than the value obtained in reference [Ket03a]. This is not surprising since the E3 branch from the $7/2^-$ state, which has a shorter half-life, was not taken into account in that work. The half-life of the $7/2^-$ state was not a free parameter in the fit; a fixed value form the present data, 143(3) ms, was used. The time spectra for both the $1/2^+$ and $7/2^-$ state decays are presented in figure 5.5. The E3 branch can also be estimated based on prompt gamma rays feeding the $1/2^+$ state. This is discussed in section 5.1.4.

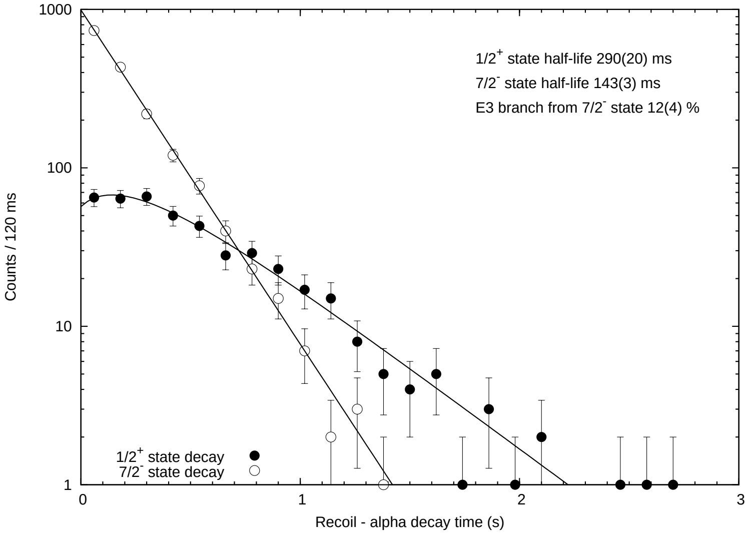

Figure 5.5: Recoil-alpha time distributions for the $1/2^+$ and $7/2^-$ states. A function consisting of two components (equations 2.18 and 2.20) describing the prompt and delayed feeding of the $1/2^+$ state was fitted to the data. The decay of the $7/2^-$ state is included to highlight the effect of the delayed feeding to the $1/2^+$ state decay curve.

The decay of the $13/2^+$ state

As can be seen from figure 5.2 a $13/2^+$ state has been observed in both ^{197}At and ^{193}At, but not in ^{195}At. In ^{197}At the $13/2^+$ state decays via an M2 transition to the $9/2^-$ ground state. The gamma-ray energy is 310.7(1) keV and the lifetime $\tau = 8(2)$ μs [Smi99]. In ^{193}At the $13/2^+$ state at an excitation energy of 39(7) keV decays mainly via an E3 transition to the $7/2^-$ state at 5(10) keV. A 24(10) % alpha decay branch feeding the corresponding $13/2^+$ state in the daughter nucleus ^{189}Bi was also observed [Ket03b]. The decay scheme of ^{193}At is displayed in figure 5.1.

Based on systematics shown in figure 5.2 the state is expected to lie somewhere below 200 keV in ^{195}At. Two different scenarios regarding the decay modes of this state seem likely. In the first case the situation would be similar to ^{193}At, and the decay would proceed via two competing processes: an E3 transition to the $7/2^-$ state and an alpha decay to the $13/2^+$ state in ^{191}Bi. The second possibility would include the $9/2^-$ state that also remains unobserved in ^{195}At. If this state were to lie between the $13/2^+$ and $7/2^-$ states the former would decay via an M2 transition to the $9/2^-$ level. This would then be followed by an M1 transition to the $7/2^-$ state. The M2 transition would be too fast for an alpha decay from the $13/2^+$ state to compete with it. Finally, should the $13/2^+$ level lie sufficiently high in energy, it would be possible that the $11/2^-$ member of the $\Omega = 7/2$ rotational band lie below the $13/2^+$ state, resulting in a prompt E1 transition between them. In addition to that there could also be aband built on top of the unobserved $9/2^-$ state. In that case there could be an E1 transition from the $13/2^+$ state to the $11/2^-$ member of the band. In both of these cases the decay of the $13/2^+$ state would be observed in the prompt gamma rays with the JUROGAM spectrometer.

In the subsequent chapters the alpha decay mode of the $13/2^+$ state is discussed first, followed by the the different de-excitation scenarios by electromagnetic transitions.

Possible alpha decay of the $13/2^+$ state

In this scenario the first task is to estimate the branching ratio between the E3 transition and the alpha decay. To calculate the branching ratio the partial half-lives for the E3 transition and alpha decay must be known. The partial half-life for the E3 transition can be obtained from the Weisskopf estimates (table 2.1), corrected for internal conversion. The alpha-decay partial half-life can be estimated by using the semiempirical formula by Taagepera and Nurmia (equation 2.23) or taken from experimentally observed half-lives of known unhindered alpha decays in this mass region. Both of these methods were employed and the results can be seen in figure 5.6. The figure presents the predicted alpha-decay branch as a function of the energy of the E3 transition in ^{195}At (i.e. the transition energy that would result from placing an alpha decay of a particular energy into the ^{195}At decay scheme). The figure shows a good agreement between the experimental data points and the prediction of the Taagepera-Nurmia equation (solid line). In the energy region expected from the level systematics (figure 5.2) the predicted alpha branch is around 5 %, increasing rapidly at transition energies below 50 keV. In ^{193}At the branching ratio for the alpha decay of the $13/2^+$ state was estimated to be approximately 24 % [Ket03b]. This value was obtained by setting the $13/2^+$ state alpha-decay hindrance factor to unity, which is the expected value for unhindered alpha decays. Also taking into account the experimentally observed half-life, the competing E3 transition would be approximately 3 times faster than the Weisskopf estimate for such transition. If this were the case in ^{195}At the magnitude of the alpha branch would be reduced by approximately a factor of three. This case is displayed in figure 5.6 with a dashed line.

As the possible alpha decay of the $13/2^+$ state would likely be hidden under the other alpha peaks in the singles alpha spectrum, additional information is needed for its identification. The $13/2^+ \rightarrow 13/2^+$ alpha decay is followed by an M2 transition to the $9/2^-$ ground state of ^{191}Bi (see figure 5.1). The gamma rays or conversion electrons from this transition provide a means of clearly identifying the possible alpha decay branch. The half-life of the $13/2^+$ state in ^{191}Bi is 562(10) ns and the total conversion coefficient is approximately 0.54, with K conversion being dominant ($\alpha_{\mathrm{K}} \approx 0.42$, $E_{\mathrm{e,K}} \approx 340$ keV). As can be seen from figure 5.6, relatively large alpha-decay branches occur for $E_\alpha < 6900$ keV. In the alpha spectrum (figure 5.3) these alpha decays would

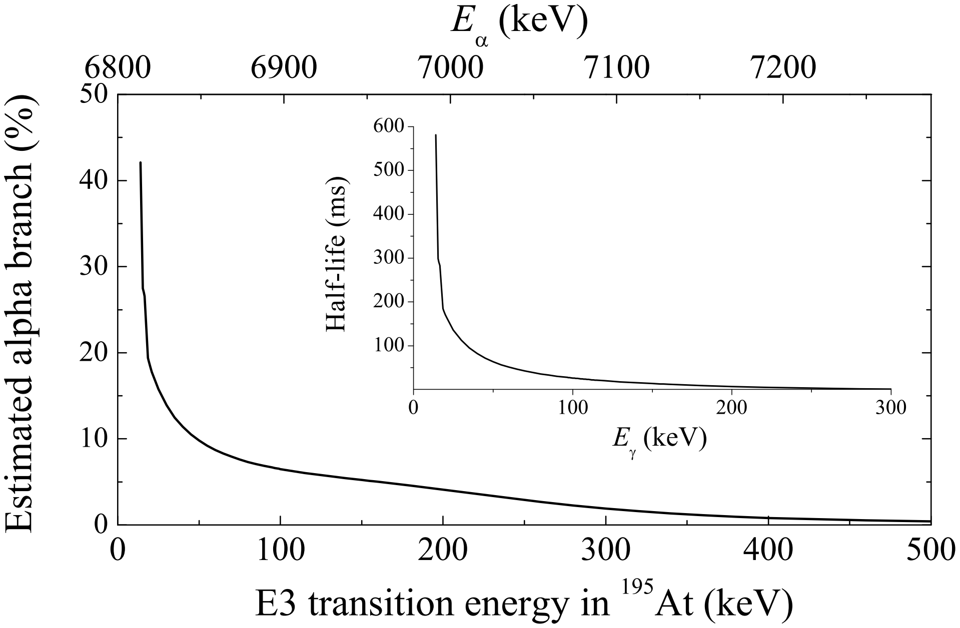

Figure 5.6: Estimated alpha decay branch from the $13/2^+$ state in ^{195}At to the corresponding state in ^{191}Bi. The experimental data points represent some known unhindered alpha decays in the $A \sim 190$ mass region. The solid line is the alpha branch based on the semiempirical Taagepera-Nurmia formula. As explained in the text, it appears that the E3 transition strength in ^{195}At is about three times faster than the Weisskopf estimate, assuming an alpha decay hindrance factor $HF = 1$. An alpha branch calculated using the Taagepera-Nurmia formula, assuming an E3 transition strength of 3 W.u., is drawn with a dashed line. The experimental alpha decay half lives were taken from references [Ket03a], [Ket03b], [Ach06] and [Xia05].

be buried under the large peak from the decay of the 0^+ ground state of ^{194}Po. For higher alpha-particle energies the alpha branch would be expected to be of the order of a few percent and essentially all of the population of the $13/2^+$ state would end up feeding the $7/2^-$ state.

If the $13/2^+$ state were to lie close to the $7/2^-$ state, a significant alpha branch would be visible in the alpha-alpha matrix. As the half-life of the $13/2^+$ state in ^{191}Bi is only 562 ns, the electronics is not able to distinguish the signals from the alpha decay and the conversion electrons from the following M2 transition in the DSSD. The total conversion coefficient for a 430 keV M2 transition is about 0.54, so most of the events in the alpha-alpha matrix would have mother and daughter alpha particle energies of $6800 \text{ keV} < E_{\mathrm{M}} < 6900 \text{ keV}$ and $E_{\mathrm{D}} = 6308$ keV. About one third of the events would have the conversion electron energy (either full or partial) summed with the alpha decay energy. It is clear from figure 5.4 that in addition to the known decays (labelled 2,3, and 4) no other significant groups with $E_{\mathrm{D}} = 6308$ keV are observed. Random correlations due to ^{194}Po ($E_{\mathrm{M}} = 6843$ keV) complicate the situation somewhat, but if the alpha particle energy from the $13/2^+$ state would be below 6850 keV the expected alpha branch would be more than 10 %. This can be estimated to yield more than 100 events, an amount which would be distinguishable even with the high ^{194}Po background. At higher energies it is possible that the alpha decays from the $13/2^+$ state would be masked by the events originating from the $7/2^-$ and $1/2^+$ decays. Identifying the $13/2^+$ state alpha decay from the alpha-alpha matrix would in this case be impossible. However, there is a small set of events between groups two and three, partially overlapping with the latter. The decay properties of the mother and daughter activities of these 21 events are as follows: $E_{\mathrm{M}} = 7010(2)$ keV, $t_{1/2,\mathrm{M}} = 120(30)$ ms, $E_{\mathrm{D}} = 6300(4)$ keV, $t_{1/2,\mathrm{D}} = 16(4)$ s. These are consistent with the alpha decay of the $7/2^-$ state. The expected half-life for the $13/2^+$ state at this energy region, where the E3 branch is the dominant decay mode, is less than 10 ms. Therefore the most likely explanation for these events is that they belong to the low-energy tail of group three.

Another way of identifying the possible alpha decay from the $13/2^+$ state in ^{195}At is by detecting the gamma rays and electrons from the following 430 keV M2 transition. In order to estimate the number of gamma rays or electrons detected it is necessary to estimate the total population of the $13/2^+$ state. As explained above, the possible alpha branch from the $13/2^+$ state must be small, of the order of a few percent or less. This means that groups three and four in the alpha-alpha matrix include almost all of the population of the $13/2^+$ state as well. As the $13/2^+$ state will be yrast at all energies where it can be expected to lie, it is slightly preferentially populated compared to the $7/2^-$ state in heavy-ion induced fusion-evaporation reactions, such as the one used in the present work. As a conservative estimate let us assume half of the events in groups three and four to have originated from the $13/2^+$ state. Finally, after correcting for the E3 branch from the $7/2^-$ state to the $1/2^+$ state, this leads to a total number of

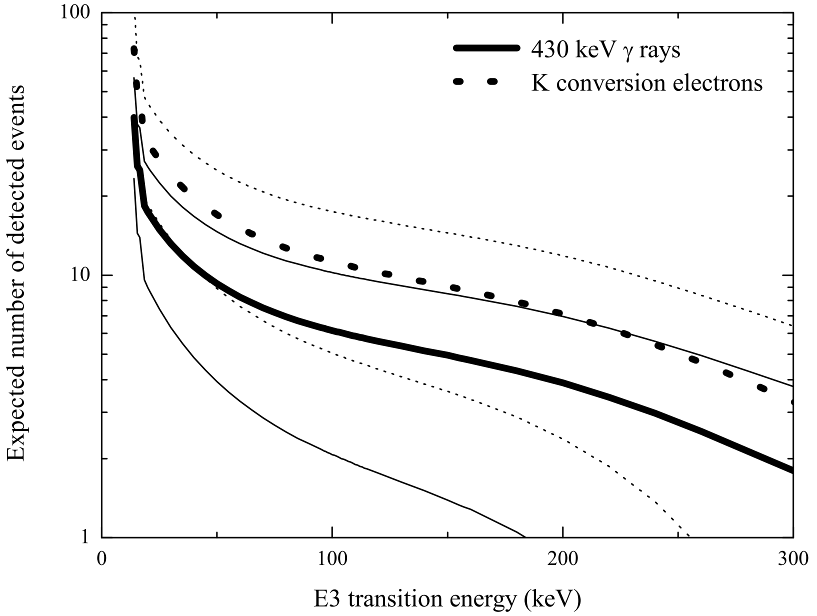

Figure 5.7: Expected number of gamma rays and electrons from the 430 keV M2 transition in ^{191}Bi following the alpha decay of the $13/2^+$ state in ^{195}At, plotted as a function of the energy of the E3 transition in ^{195}At. Of the three lines the middle one is the expected number of events, the surrounding lines describe the error estimate.

8200(1300) $13/2^+$ state decays. Using this value and the known detection efficiencies of the GREAT spectrometer (see chapter 3), the expected number of detected gamma rays and conversion electrons following the $13/2^+$ state alpha decay can be calculated. The result is shown in figure 5.7.

To search for experimental evidence for the gamma rays and electrons following the possible alpha decay of the $13/2^+$ state, alpha-gamma and alpha-electron matrices from events of the type recoil-alpha-gamma/electron were constructed. The alpha-gamma matrix can be seen in panel (a) of figure 5.8. There are only three gamma rays observed at 430 keV with correlated alpha decays in the expected energy region ($\sim$ 6800 keV - 7000 keV). All of these occur in the region of high background from ^{194}Po (E_α = 6843 keV). The alpha-decay half-life for these three events is $t_{1/2} = 530^{+720}_{-190}$ ms, which is consistent with the half-life of ^{194}Po ($t_{1/2} = 392(4)$ ms). As the expected half-life for the $13/2^+$ state at this alpha-particle energy lies in the region of 60 ms, it is likely that these events do not arise from the alpha decay of the $13/2^+$ state in ^{195}At.

The alpha-electron matrix can be seen in panel (b) of figure 5.8. The only events in the matrix are the L and M conversion electrons from the $7/2^-$ to $9/2^-$ transition in ^{191}Bi, fed by the $7/2^-$ to $7/2^-$ alpha decay of ^{195}At. The K electrons are not observed due to their low energy ($E_{\mathrm{e,K}} \approx 58$ keV, $E_{\mathrm{e,L}} \approx 133$ keV, $E_{\mathrm{e,M}} \approx 145$ keV). There are 108 events in figure 5.8, almost all of which come from the conversion of the M1 transition. If one proceeds to calculate the expected number of L and M electrons from the transition, the result is ~ 120. This is in exellent agreement with the observation, thus confirming the calculations. In summary no experimental evidence for the alpha decay of the $13/2^+$ state in ^{195}At could be found in this work. Based on figure 5.7, up to about $E_{\mathrm{E3}} \sim 150$ keV (corresponding to the excitation energy of the $13/2^+$ state being $E(13/2^+) \sim 180$ keV), the alpha-decay mode of the $13/2^+$ state can be ruled out.

Electromagnetic transitions from the $13/2^+$ state

If the alpha branch of the $13/2^+$ state would be too small for detection (i.e. $E_{\mathrm{E3}} > 150$ keV or ($E(13/2^+) > 180$ keV) one could still observe the gamma rays or conversion electrons from the electromagnetic transitions de-exciting the $13/2^+$ state. There are two different scenarios that will be considered here: an E3 transition from the $13/2^+$ state to the $7/2^-$ state and a cascade of two transitions proceeding via an intermediate state. The expected number of detected gamma rays and conversion electrons from the de-excitation of the $13/2^+$ state can be calculated in manner similar as described above for the 430 keV transition, using the same assumptions as a starting point. The results are presented in figure 5.9 for three different transition multipolarities relevant for the following discussion.

Let us begin with the possibility of an E3 transition between the $13/2^+$ and $7/2^-$ states. Panel (a) of figure 5.9 shows the expected number of detected gamma rays and conversion electrons as a function of the E3 transition energy. Conversion electrons from the L and M shells are included as they are the dominant ones. Looking at the figure, the electrons provide the most promising detection method, especially at low transition energies. The half-life of the $13/2^+$ state in this scenario would be of the order of tens of milliseconds. It is not practical to use recoil-gamma/electron search times extending to tens or hundreds of milliseconds because the amount of background radiation in the spectra would increase. The limiting factor for the search time is the total counting rate of the implantation detector. A recoil-gamma/electron search time of 10 ms was used in producing figure 5.9 (a). For the gamma-ray detection only the planar Ge-detector was assumed as the expected transition energies are low.

An alpha-electron matrix constructed from events of the type recoil-electron-alpha is displayed in panel (a) of figure 5.10. The events from the decay of the $13/2^+$ state would appear to be correlated with the wide distribution of alpha decays from the

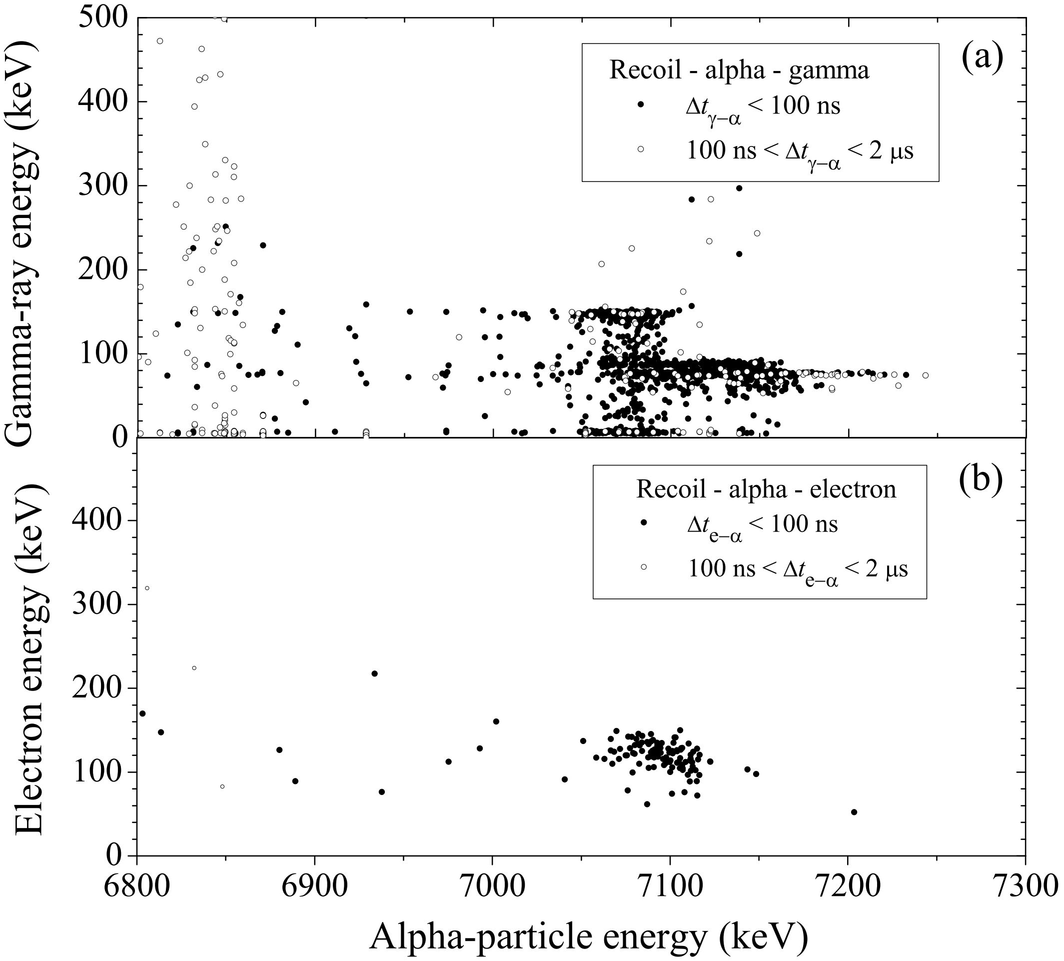

Figure 5.8: Alpha-gamma and alpha-electron matrices from events of the type recoil-alpha-gamma (panel (a)) and recoil-alpha-electron, using data from DSSD-A only. The alpha-gamma and alpha-electron search times (Δt_γ and Δt_e) are indicated in the figures. In the alpha-gamma matrix data from both the planar and clover Ge-detectors were used. It is readily apparent that no evidence for the 430 keV M2 transition in ^{191}Bi following the possible alpha decay of the $13/2^+$ state in ^{195}At can be seen. The most prominent features in the matrices are the gamma rays and L conversion electrons from the $7/2^- \rightarrow 9/2^-$ M1 transition, which follows the alpha decay of the $7/2^-$ state in ^{195}At.

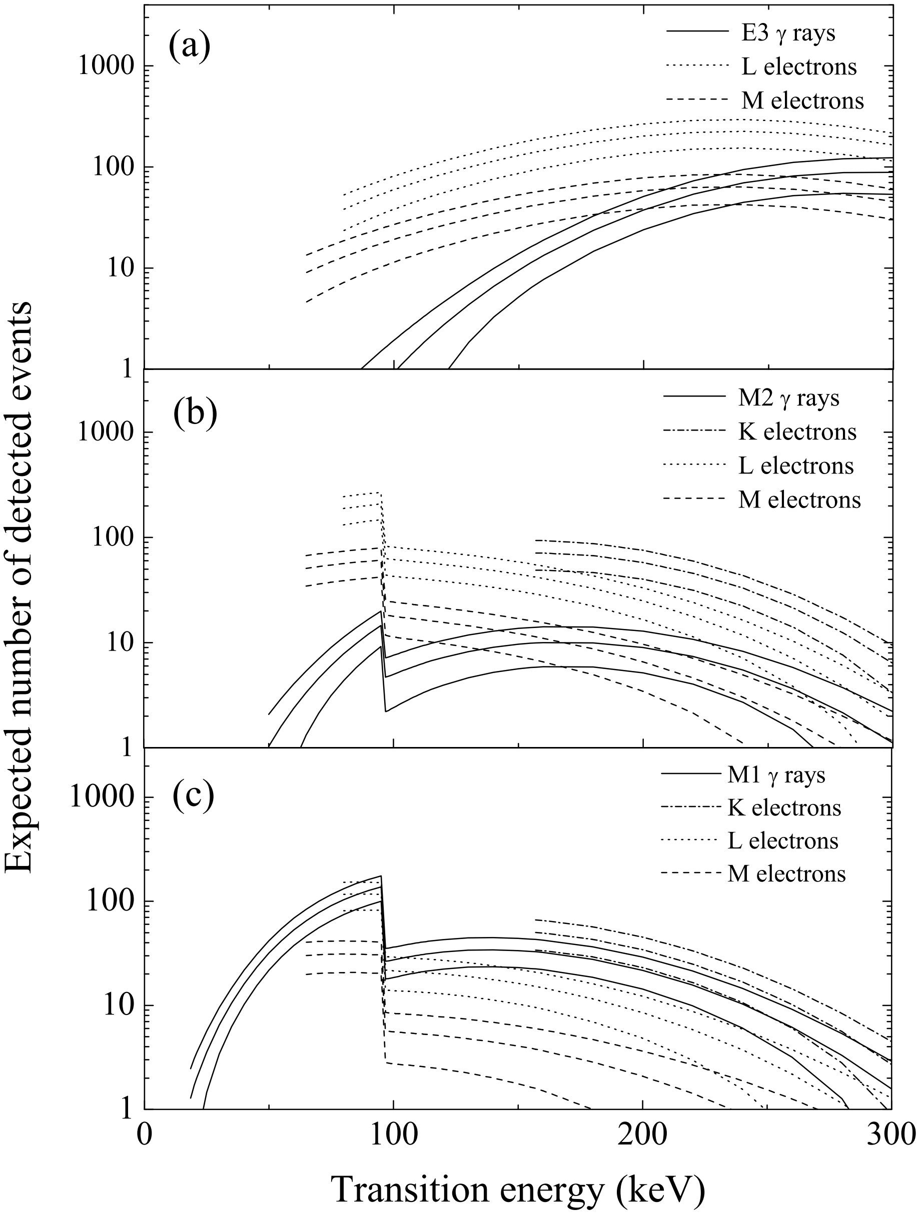

Figure 5.9: Panel (a): the expected number of L and M conversion electrons and gamma rays from an *E*3 transition between the $13/2^+$ and $7/2^-$ states in ^{195}At. K conversion for E3 radiation is very small in the region of interest and is thus not included in the figure. Panels (b) and (c) are the expected number of K, L and M conversion electrons and gamma rays from a possible M2 and M1 transitions arising from the decay of the $13/2^+$ state in ^{195}At. The low energy cutoffs for electron detection were dictated by the noise level of the PIN-diodes. As in figure 5.7, the surrounding lines describe the error estimate.

$7/2^-$ state (approximately 7050 keV $< E_\alpha <$ 7250 keV). This area of interest is indicated by the box drawn with a dotted line. A histogram containing the events inside the box can be seen in panel (b) of the figure. A background spectrum was generated from events observed in the PIN detectors between 90 ms and 100 ms after the recoil implantation. Since the half-life of the $13/2^+$ state is expected to be at most about 30 ms in this energy region, this time window would be expected to consist mostly background radiation. The background spectrum is normalized to contain the same number of events as the projection. It is apparent from the figure that the spectra are essentially the same. An example, intended to illustrate what a realistic number of events would look like on top of the background, is included in the figure. Assuming $E_{\mathrm{E3}} = 150$ keV and using figure 5.9, about 130 L and M conversion electrons would be observed in such a situation. The Gaussian distribution drawn on top of the background spectrum has an area of 130 counts (taking into account the 10 keV bins) and a width similar to the electron distribution seen in panel (b) of figure 5.8. As another example, $E_{\mathrm{E3}} = 100$ keV would yield a similar distribution with an area of about 80 counts. Clearly no evidence for the E3 transition from the $13/2^+$ state to the $7/2^-$ state in ^{195}At can be found in the experimental spectrum. To summarize: if there were an E3 transition between the $13/2^+$ and $7/2^-$ states, it should have been detectable either directly (if $E_{\mathrm{E3}} > 100$ keV) or via the competing alpha decay branch (if $E_{\mathrm{E3}} < 150$ keV). No evidence of either could be found from the present data.

This leaves the possibility that the decay of the $13/2^+$ state proceeds via at least one intermediate state. An obvious candidate would be the $9/2^-$ state, which is the ground state in all odd-mass astatine isotopes down to ^{197}At. It has not been observed in any of the more neutron deficient isotopes, but it is not unreasonable to expect it to lie at a low excitation energy in ^{195}At. It could be placed between the $13/2^+$ and $7/2^-$ states, leading to an M2 transition followed by an M1. The half life of the $13/2^+$ state in this scheme would be in the microsecond region. The half life of this M2 transition is about an order of magnitude longer than expected from the Weisskopf estimates due to the spin flip which occurs between the $13/2^+$ and $9/2^-$ states.

Panels (b) and (c) in figure 5.9 present the estimated number of detected electrons or gamma rays from the M2 and M1 transitions, respectively. Due to stronger internal conversion the M2 would be detectable mainly via conversion electrons, while the M1 would predominantly decay via by gamma-ray emission. The limiting factors for the detection of the M2 transition are the recoil-gamma/electron search time used and the flight time of the recoils through the separator. The former is significant at low transition energies and the latter at higher energies. If a search time of 100 μs is used only about 30 % or less of the decay events are lost due to the combination of these factors. The calculations for the detection of the M1 transition are complicated by the fact that at very low energies the half life of the $13/2^+$ state has abrupt changes due to the L edges in the conversion coefficient. This in turn changes the amount of lost events due to the recoil-gamma/electron search time significantly if the energy of the M2 transition were below 20 keV. In these cases the expected number of detected events can be reduced by a factor of 2 or more. The calculations made for figure 5.9 assume a fixed value of $E_{\mathrm{M2}} = 20$ keV.

In panel (c) of figure 5.10 an alpha-gamma matrix from events of the type recoil - gamma - alpha is displayed. As can be seen from the figure no evidence whatsoever can be seen for the $9/2^-$ to $7/2^-$ M1 transition. A 158 keV gamma ray, known in ^{196}At [Smi00], is clearly visible. Also observed are X rays from the 311 keV M2 transition in ^{197}At. The actual gamma-ray events are missing from the spectrum due to the rather large internal conversion ($\alpha \approx 1.8$) coupled with the rapidly decreasing efficiency of the planar Ge detector with increasing energy (see figure 3.10). Panel (d) presents an alpha-electron matrix where only background electrons appear to be visible between alpha-particle energies of 7000 keV to 7300 keV, revealing no sign of the M2 transition between the $13/2^+$ and $9/2^-$ states. The K and L conversion electrons from the above mentioned 311 keV transition are present.

Finally, regarding the possible $13/2^+$ to $11/2^-$ E1 decay, no evidence for such a decay path was found from the present data. This decay mode could be deduced from prompt $\gamma\gamma$-coincidence data, where transitions de-exciting the $11/2^-$ state would appear in coincidence with gamma rays feeding the $13/2^+$ level. Such coincidences were not observed. Prompt gamma-ray spectorscopy of ^{195}At is discussed in the following section.

The only viable explanation for the non-observation of any candidate transition de-exciting the $13/2^+$ state is that both the M2 and M1 transitions lie below the low-energy detection tresholds. Therefore limits can be placed on the transition energies: $E_{\mathrm{M2}} < 65$ keV and $E_{\mathrm{M1}} < 30$ keV (assuming $E_{\mathrm{M2}} > 20$ keV). This would place an upper limit for the excitation energy of the $13/2^+$ state at ~ 130 keV.

5.1.2 Prompt gamma-ray spectroscopy of ^{195}At

In order to examine the transitions feeding the known states in ^{195}At the Recoil-Decay-Tagging method was employed. Alpha decays from the $1/2^+$ ground state and the low-lying $7/2^-$ state were suitable for tagging. As explained above the $13/2^+$ most likely feeds the $7/2^-$ state via unobserved transitions. Hence the prompt gamma rays feeding the $13/2^+$ state will be present in gamma-ray spectra tagged with the $7/2^-$ state alpha decays.

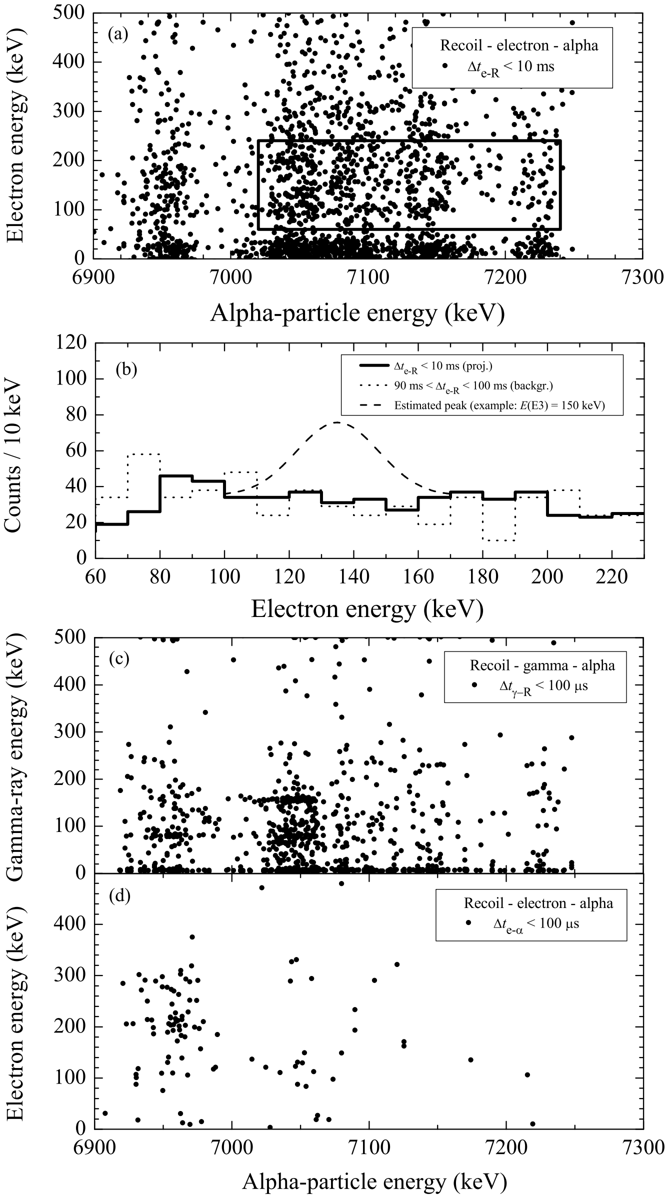

Figure 5.10: Panel (a): Alpha-electron matrix from events of type recoil-electron-alpha. The search times are indicated in the figure. Panel (b) shows a y-projection of the events located inside the rectangle in (a). A background spectrum, normalized to contain the same number of counts as the projection, was generated from events detected between 90 ms and 100 ms from recoil implantation. On top of that an estimeted peak, assuming E3 transition energy of 150 keV, was drawn. Panel (c) presents an alpha-gamma matrix from events of the type recoil-gamma-alpha. The known 159 keV isomeric E2 transition in ^{196}At is clearly visible. Finally panel (d) contains an alpha-electron matrix constructed from events of the type recoil-electron-alpha. Conversion electrons from a known 311 keV M2 transition in ^{197}At are seen (see text for details). No evidence for decays that could be assigned to ^{195}At can be observed in any of the panels.

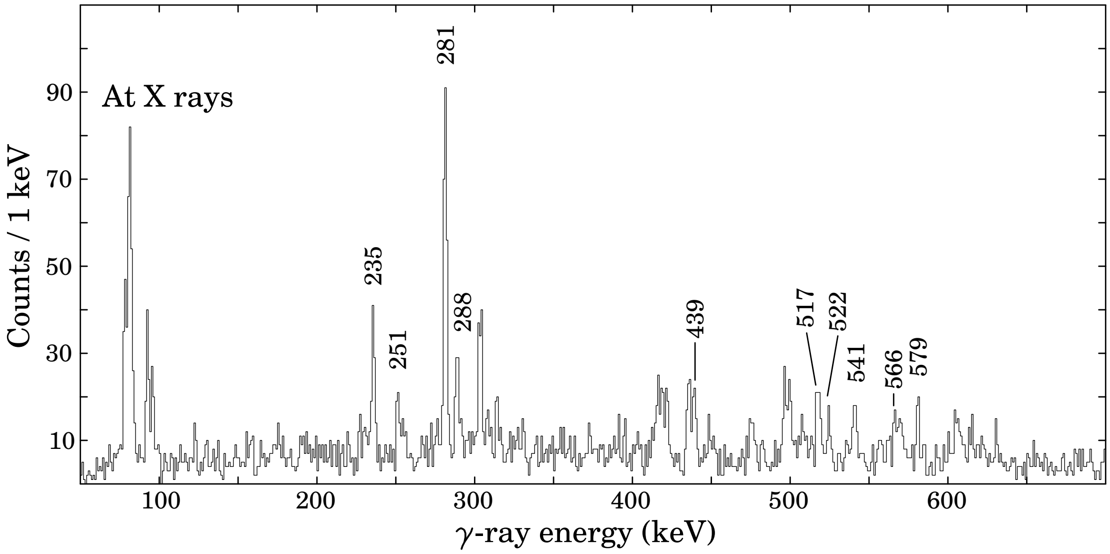

Figure 5.11: Gamma-ray spectrum tagged with the $7/2^-$ alpha decays of ^{195}At. Peaks that have been placed into the level scheme, figure 5.14, are labelled with their energies.

5.1.3 Band 1 - $\mathrm{i}_{13/2}$

As the $13/2^+$ state will be yrast at all energies where it can reasonably be expected to lie, the most prominent peaks in the $7/2^-$ alpha tagged gamma-ray spectrum are very likely to represent the transitions feeding the $13/2^+$ state.

A prompt gamma-ray spectrum tagged with the alpha decays from the $7/2^-$ state is presented in figure 5.11. The energy and time gates for the alpha decay were 7060 keV $< E_\alpha <$ 7280 keV and $\Delta t_{\alpha-\mathrm{R}} = 450$ ms. Both DSSDs were used in order to obtain more statistics. As there are no alpha lines lying higher in energy, the low energy tails from DSSD-B do not contaminate the spectra. A $\gamma\gamma$-matrix was constructed using the same conditions for coincidence analysis.

As the $7/2^-$ state alpha-decay peaks are somewhat contaminated by the decays of ^{194}At and ^{196}At, a clean gamma-ray spectrum was obtained by using alpha-alpha correlations. A prompt gamma-ray spectrum, tagged with the decay events comprising groups three, four, seven and eight in the $\alpha\alpha$-matrix, is presented in panel (b) of the figure 5.13. It was used to confirm the assignments of the gamma rays to ^{195}At. The gamma rays that could be associated with ^{195}At with confidence are presented in table 5.2. The level scheme of ^{195}At can be seen in figure 5.14.

Table 5.2: Measured transition energies, gamma ray intensities normalized to that of the 281 keV transition and spins and parities of the initial and final states.

E_γ (keV)	I_γ (%)	E_i (keV)	I^π_i	I^π_f
119.2(5)	10(3)	119		$1/2^+$
149.9(7)	14(7)			
175.2(5)	7(3)	294	$(5/2^+)$	
235.1(4)	35(9)	$\Delta + 516$	$17/2^+$	$15/2^+$
250.8(7)	25(9)	$\Delta + 1056$	$21/2^+$	$19/2^+$
281.2(2)	100(15)	$\Delta + 281$	$15/2^+$	$13/2^+$
288.4(4)	36(10)	$\Delta + 805$	$19/2^+$	$17/2^+$
302.8(3)	58(12)			
307.5(7)	17(9)			
312.3(9)	19(12)			
315.5(15)	12(10)	$\Delta + 1372$	$23/2^+$	$21/2^+$
355.2(7)	12(5)	650	$(9/2^+)$	
416.2(6)	35(12)			
420.6(5)	43(12)			
434.4(5)	40(12)			
438.6(6)	34(12)	$\Delta + 720$	$(19/2^+)$	$15/2^+$
476.2(7)	25(11)			
496.1(6)	28(8)			
499.1(8)	28(8)			
517.1(6)	33(13)	$\Delta + 516$	$17/2^+$	$13/2^+$
522.4(6)	29(11)	$\Delta + 805$	$19/2^+$	$15/2^+$
541.0(5)	34(11)	$\Delta + 1056$	$21/2^+$	$17/2^+$
566.5(8)	39(19)	$\Delta + 1372$	$23/2^+$	$19/2^+$
569.9(8)	37(16)			
579.4(8)	21(12)	$\Delta + 1635$	$25/2^+$	$21/2^+$
605.1(11)	17(12)			
615.1(9)	19(12)			
629.2(5)	34(12)			

The concentration of peaks in two groups below 300 keV and above 500 keV hints at the existence of a strongly coupled rotational band. Therefore the 281 keV gamma line, having the largest intensity by a considerable margin, can quite confidently be placed to feed the $13/2^+$ state. A gamma-ray spectrum gated with the 281 keV transition can be seen in panel (a) of figure 5.12. The spectrum shows a clear coincidence with the 235 keV gamma ray, which is a candidate to preceed the 281 keV transition due to its high intensity. Furthermore, the sum energy of the two gamma rays is 516.3(6) keV, which matches the observed gamma ray at 517.1(6) keV. This gamma ray is not in coincidence with either of the 281 keV or 235 keV transitions. These arguments allow the assignment of the 516 keV gamma ray as an E2 transition from a $17/2^+$ state to the $13/2^+$ bandhead in the favoured signature rotational band. The 281 keV gamma ray is then an interband M1 transition from the unfavoured signature band to the $13/2^+$ state. The 439 keV gamma ray appears in coincidence with the 281 keV transition only, which is why it is therefore placed to feed the $15/2^+$ state.

Summing the gates on the 281 keV and 235 keV transitions yields the spectrum presented in panel (b) of figure 5.12. Among other lines, it reveals further coincident gamma rays at 251 keV and 288 keV. Only the latter has an energy sum with the 235 keV gamma ray, 523.5(6) keV, matching reasonably well the observed gamma ray at 522.4(6) keV. This gamma ray is weakly visible in the spectrum gated with the 281 keV transition, as can be seen in figure 5.12, but is not observed when gating with the 235 keV and 288 keV transitions. This allows the 522 keV gamma ray be identified as the lowest E2 in the unfavoured signature band. The sum energy of the 288 keV and 251 keV gamma rays is 539.2(9) keV. The observed gamma ray at 541.0(5) keV is close but not quite within the error margins. The energies still match within two standard deviations. Therefore, the 541 keV gamma ray is assigned to be the $21/2^+$ to $17/2^+$ E2 transition. There are other possible gamma rays with energy sums with the 288 keV transition matching observed energies, but the 251 keV gamma ray is the only one appearing in the coincidence spectra. Therefore it will be placed preceeding the 288 keV transition.

Summing the gates of all transitions placed in the level scheme so far produces the spectrum of panel (c) in figure 5.12. It reveals immediately a number of new coincident peaks, most notably two higher energy transitions at 566 keV and 579 keV. Gating on these two then produces the spectrum of panel (d) in the figure. The presence of the 281 keV and 235 keV peaks in the spectrum adds confidence to the 566 keV and 579 keV gamma rays belonging to the same rotational band. The absence of the 541 keV gamma ray from the gated spectrum is most likely due to the low statistics. The gamma ray at 316 keV has an energy sum with the 251 keV, 566(2) keV, which matches the observed value of 566.5(8) keV. This allows the placement of the 316 keV gamma ray preceeding the 251 keV one in the level scheme. The 579 keV transition is then placed in parallel with it. This is further supported by the fact that the events at 251 keV appear only in coincidence with the 579 keV gamma ray, not the 566 keV one.

The remaining peaks that appear both in the coincidence spectrum of panel (c) in figure 5.12 and the total alpha-alpha gated gamma spectrum are 193 keV, 620 keV and 689 keV. They appear to be in coincidence with members of the $13/2^+$ band, but their placement in the level scheme could not be deduced. The statistics were too low for an angular distribution analysis, except for the 281 keV transition. The experimental value was R_{exp} =0.9(3), which is consistent with the calculated value for a pure 15/2 → 13/2 M1 transition, $R_{\mathrm{theor}} = 0.67$. The theoretical value for a 17/2 → 13/2 E2 transition is 1.73. The theoretical values were calculated using data from reference [Yam67].

5.1.4 Non-yrast states

The transitions in figure 5.11 not appearing in coincidence with those assigned to the yrast band presumably feed the $7/2^-$ state at 32 keV. Based on its high intensity the 303 keV gamma ray is a strong candidate to either directly feed the $7/2^-$ state or feed the $9/2^-$ state and be followed by a highly converted low energy transition. The large number of possible energy sums and transitions with similar intensities make it possible to construct many scenarios. With the present statistics, which are insufficient for coincidence analysis, none of the options can be chosen over the others with a reasonable level of confidence. Therefore, the clarification of the level ordering above the $7/2^-$ state has to be left for the future. However, in addition to the 303 keV transition at least the gamma rays with energies 416, 421, 434, 496 and 499 keV are good candidates to be placed to feed the $7/2^-$ state. It should also be noted that no coincidences with the yrast band members were observed when gating with the above mentioned transitions.

A gamma-ray spectrum tagged with the $1/2^+$ ground state alpha decays of ^{195}At is presented in figure 5.13. The number of detected alpha particles was ~ 2000, hence the gamma ray spectrum has very low statistics. Furthermore, as there is a considerable E3 gamma decay branch from the $7/2^-$ state at 32 keV to the $1/2^+$ state, the strongest transitions feeding the $13/2^+$ and $7/2^-$ states are also present in the spectrum. Also present are gamma rays from ^{197}At as the $9/2^-$ ground state alpha decay energy 6957 keV overlaps vith the ^{195}At $1/2^+$ decay. The remaining gamma rays are then assigned to feed the $1/2^+$ ground state. The proposed level structure is based on energy sum and intensity arguments.

The presence of gamma rays feeding the $13/2^+$ and $7/2^-$ states in the $1/2^+$ alpha tagged spectrum present a possibility to confirm the magnitude of the E3 branch between the $7/2^-$ and $1/2^+$ states. The relative intensities of these peaks can be used to deduce the E3 branching ratio b_{E3}. The result is $b_{\mathrm{E3}} = 13(6)$ %, which is in very good agreement with the result obtained from the recoil-alpha time distribution: 12(4) % (see section 5.1.1).

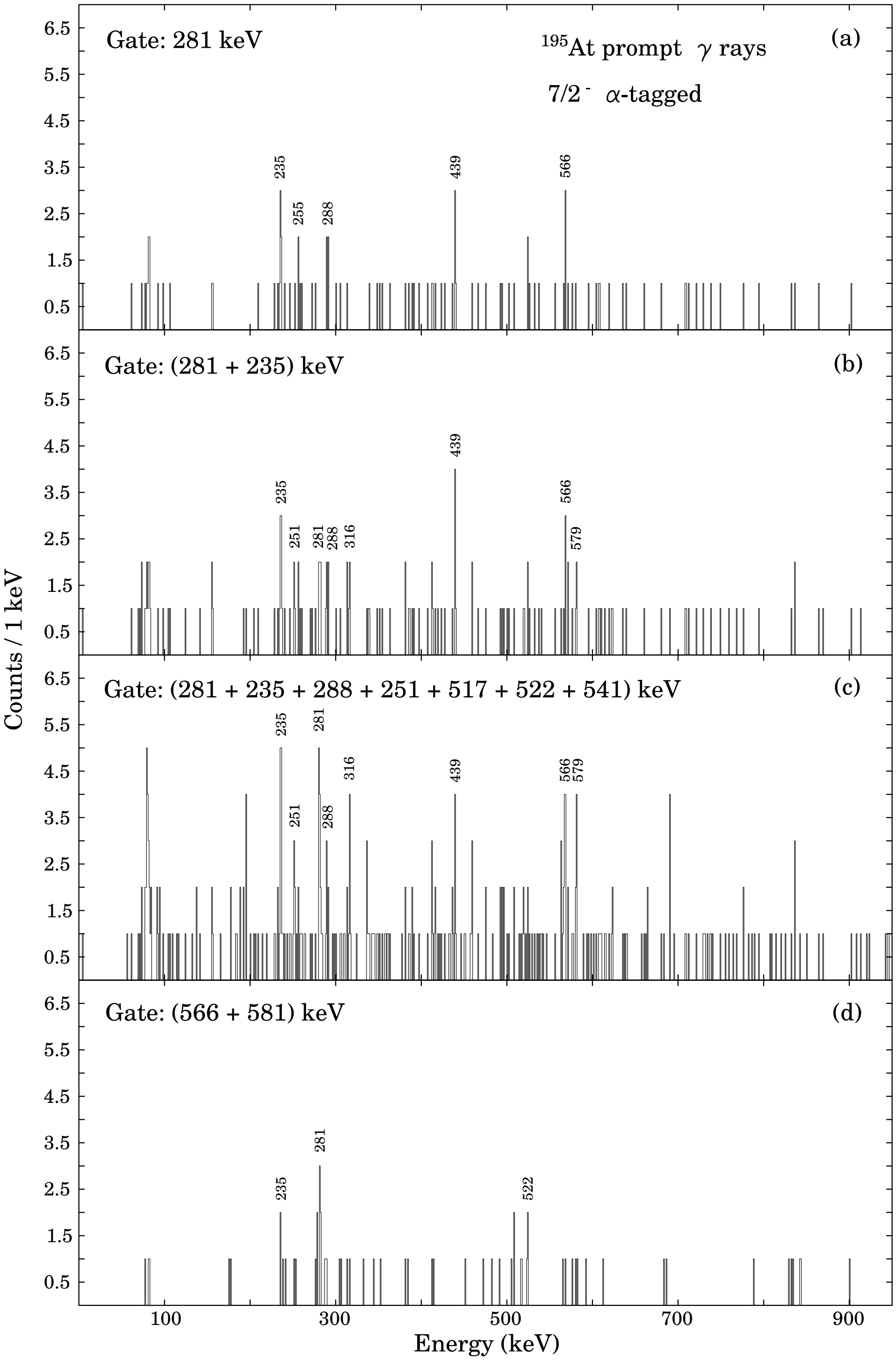

Figure 5.12: Panel (a) shows the gamma spectrum gated with the 281 keV transition. In panel (b) the sum of gates on the 281 keV and 235 keV gamma rays is displayed. Panel (c) shows the sum of gates on all the lowest transitions in the band feeding the assumed $13/2^+$ state, while panel (d) contains the spectrum gated with the 566 and 581 keV gamma rays. The gamma-gamma matrix was generated from the single alpha tagged data and therefore contains impurities. The peaks associated with ^{195}At using the alpha-alpha tagged data are labelled with their energies.

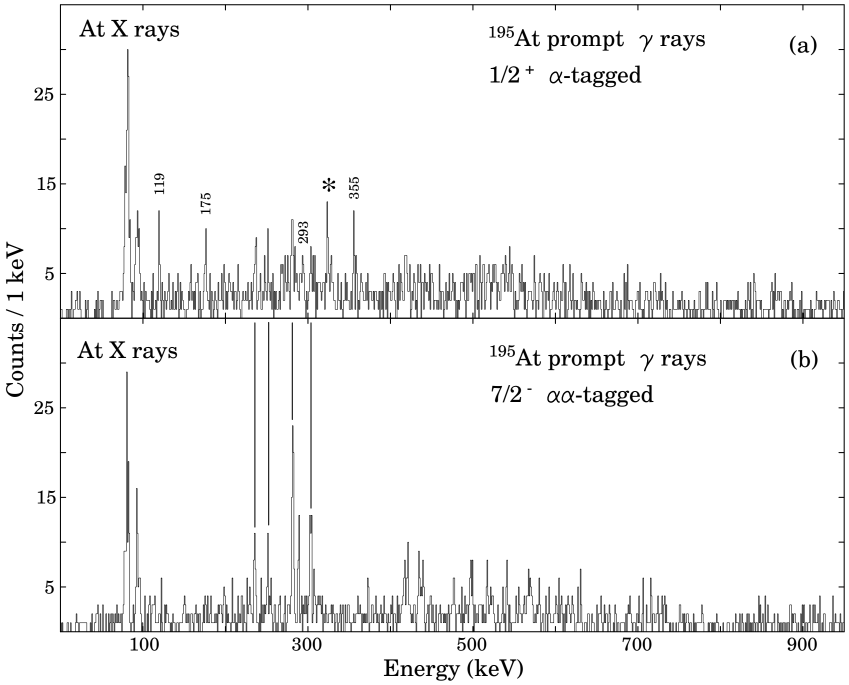

Figure 5.13: A gamma-ray spectrum obtained by tagging with the alpha decays of the $1/2^+$ ground state of ^{195}At (panel (a)). The peak marked with an asterisk is the $15/2^+ \rightarrow 13/2^+$ transition in ^{197}At. Panel (b) shows the gamma-ray spectrum tagged with the $7/2^-$ state alpha decays of ^{195}At and the ^{191}Bi daughter alpha decays (hence the low statistics). The presence of the yrast band transitions in the $1/2^+$ tagged spectrum is clear.

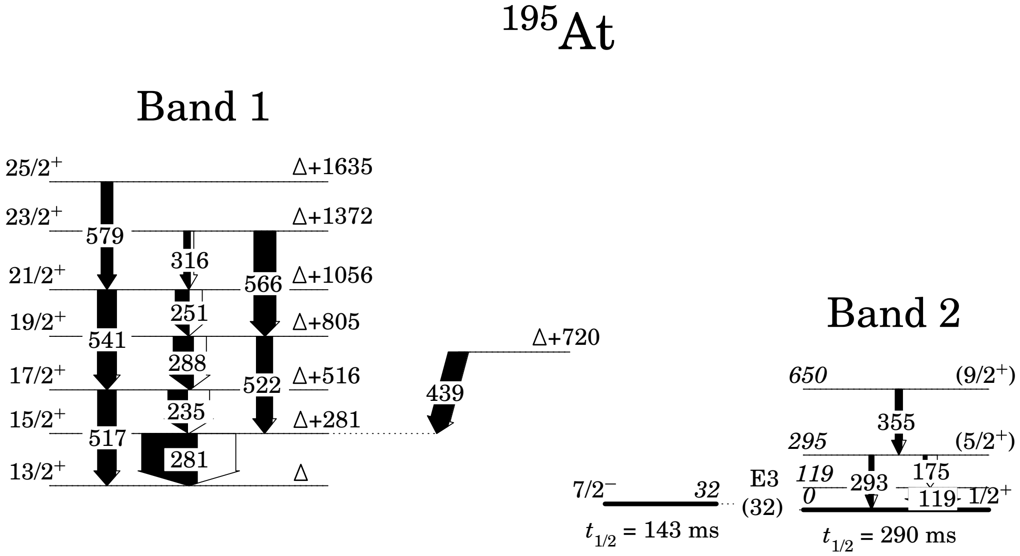

Figure 5.14: Level scheme of ^{195}At.

5.2 Odd-odd isotopes ^{194}At and ^{196}At

The odd-odd astatine isotopes ^{194,196}At have been studied previously in Jyväskylä in the thesis work of T. Enqvist, [Enq96]. An isomeric state was identified in^{196}At by Smith *et al.* [Smi00]. The decay schemes based on these references are presented in figure 5.15. They are intended to facilitate the following discussion.

5.2.1 ^{194}At

Four alpha decay energies were assigned to ^{194}At in the previous study [Enq96]: 7089(6) keV, 7154(5) keV, 7190(5) keV and 7265(6) keV. A common half-life was determined to be 296^{+19}_{-16} ms. It was proposed that the 7089 keV and 7154 keV alpha decays originate from a 10^- state in ^{194}At. The 7154 keV decay was assigned to directly feed the corresponding 10^- state in the daughter nucleus, ^{190}Bi, and the 7089 keV decay would go to an unknown excited state lying at about 165 keV. The 7190 keV and 7265 keV decays were assigned to the decay of a 3^+ state in ^{194}At, the 7265 keV decaying directly to the 3^+ state in ^{190}Bi and the 7190 keV decay feeding an excited state lying at 76 keV. In the same experiment a 76.4(3) keV gamma ray was found to follow the ^{194}At alpha decays, but it appeared to be in coincidence with a wide alpha particle energy distribution. Therefore its placement in the decay scheme could not be determined.

In panel (a) of figure 5.16 the (mother alpha, daughter alpha) pairs assigned to the decay of ^{194}At from the current work are presented. The events in which a 70 keV - 80 keV gamma ray follows the mother decay within 10 μs are depicted using filled circles. As the daughter alpha-particle energies are very close to each other (6431 keV and 6456 keV), the events in the alpha-alpha matrix end up in two partially overlapping groups. These are approximately outlined by the boxes indicating the decay of the high-spin and low-spin states in ^{194}At.

Panel (b) is the x-projection of the data displayed in panel (a), i.e. the mother alpha decays. It shows an irregular distribution of alpha decays where it is difficult to discern any clearly defined peaks, although one appears to lie between 7150 keV and 7200 keV. Panel (c) is the y-projection (daughter decays) from the data of panel (a). The two overlapping alpha-particle energies (6431 keV and 6456 keV) are highlighted by approximately dividing the data to high- and low-spin parts according to their mother alpha-particle energies. The high-spin part is displayed with the dotted line and the low-spin part with the dashed line. The corresponding daughter alpha-particle energies are 6450(5) keV (high spin) and 6427(5) keV (low spin).

Panels (d) and (e) show the x-projections of the events inside the boxes outlined in

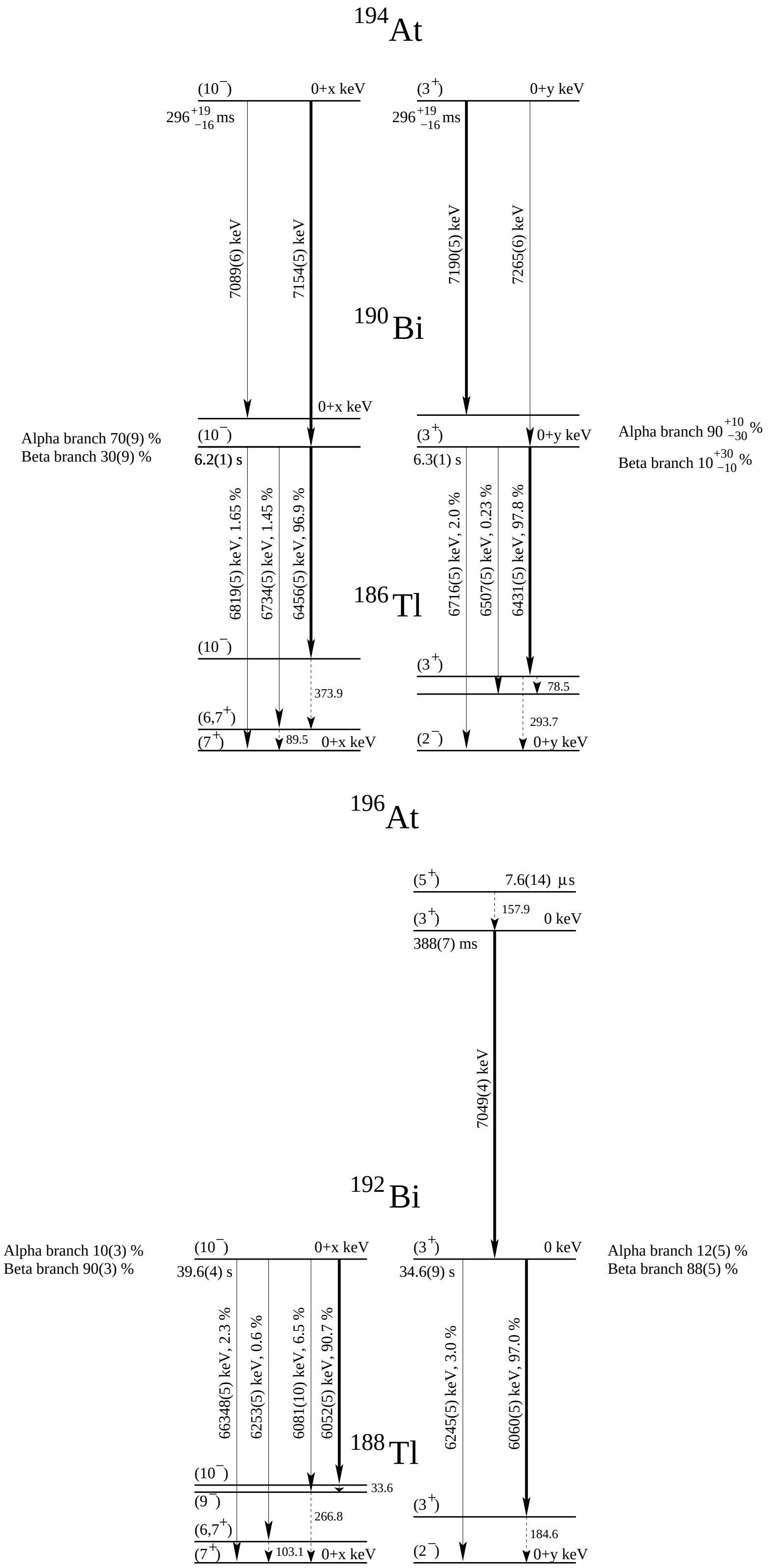

Figure 5.15: Decay schemes for ^{194}At (top) and ^{196}At (bottom), based on the previous works reported in [Dup91], [Enq96] and [Smi00].

panel (a). The most prominent peak in the high-spin part corresponds to an alpha-particle energy 7157(5) keV. In the low-spin part the largest peak has an energy of 7177(5) keV.

A gamma-ray spectrum consisting of events observed within 10 μs following the ^{194}At alpha decays is presented in panel (f) of figure 5.16. The previously observed 76 keV gamma ray is the only peak visible in the spectrum. The energy of the peak from the present data is 76.7(3) keV. A question arises whether the observed peak consists of gamma rays or K-shell X-rays. The X-ray energies in bismuth are 77.11 keV ($K_{\alpha 1}$), 74.82 keV ($K_{\alpha 2}$) and ∼87 keV - 90 keV for the K_β lines. The intensity ratio is $I(K_\beta)/I(K_\alpha) = 0.29$. The observed peak energy lies between the literature values quoted above. Furthermore, as there are 43 events in the peak, one would expect about 12 K_β events between 87 keV and 90 keV. As there are only 3 events between 85 keV and 90 keV, it seems that at least ∼70 % of the counts in the 76 keV peak are gamma-ray events and not K X-rays following a highly converted transition.

From panel (a) figure 5.16 it is apparent that there are two distinct groups that appear in coincidence with gamma rays between 70 keV and 80 keV. The mother and daughter alpha particle energies associated with these groups are $E_{\mathrm{M}} = 7086(10)$ keV and $E_{\mathrm{D}} = 6460(8)$ keV for group A and $E_{\mathrm{M}} = 7174(5)$ keV and $E_{\mathrm{D}} = 6428(3)$ keV for group B. The daughter decay energies are in very good agreement with the published values $E_{\mathrm{D}} = 6456(5)$ keV and $E_{\mathrm{D}} = 6431(5)$ keV for the 10^- and 3^+ states in ^{190}Bi [And03a]. The measured half-lives for both groups, $t_{1/2,\mathrm{A}} = 4.4^{+5.4}_{-1.6}$ s and $t_{1/2,\mathrm{B}} = 4.9^{+2.0}_{-1.1}$ s are also in agreement with the published values: $t_{1/2} = 5.9(6)$ s and $t_{1/2} = 5.7(8)$ s for the 10^- and 3^+ states, respectively. The gamma rays in both groups are essentially prompt, i.e. the time intervals between the alpha decays and the observation of the gamma rays are of the order of tens of nanoseconds.

Obviously, whatever other transitions in ^{190}Bi follow these decays they must be internally converted to such a degree that no gamma rays are observed. This introduces another problem, namely the summing of the signals from the alpha particle and the conversion electron in the implantation detector. If the half life of the decaying state is of the order few microseconds or less, the electronics cannot distinguish between the corresponding signals from each other. Conversion from K, L, M,... shells cause their own sum peaks in the spectrum, the peaks from M, N,... conversion overlapping with the L conversion peak. As an added complication the electrons that escape from the implantation detector cause a continous distribution between the bare alpha peak (where gamma-ray emission has followed the alpha decay) and the alpha + full energy electron peak. The shape of this distribution depends on the energy of the electrons and the implantation depth, which of course depends on the details of the experimental setup and the reaction used. The phenomenon is discussed in references [Hess06] and [The08]. However, as is readily apparent from figure 5.16, the statistics makes unambiguous resolving the alpha and alpha+electron peaks impossible. The lack of

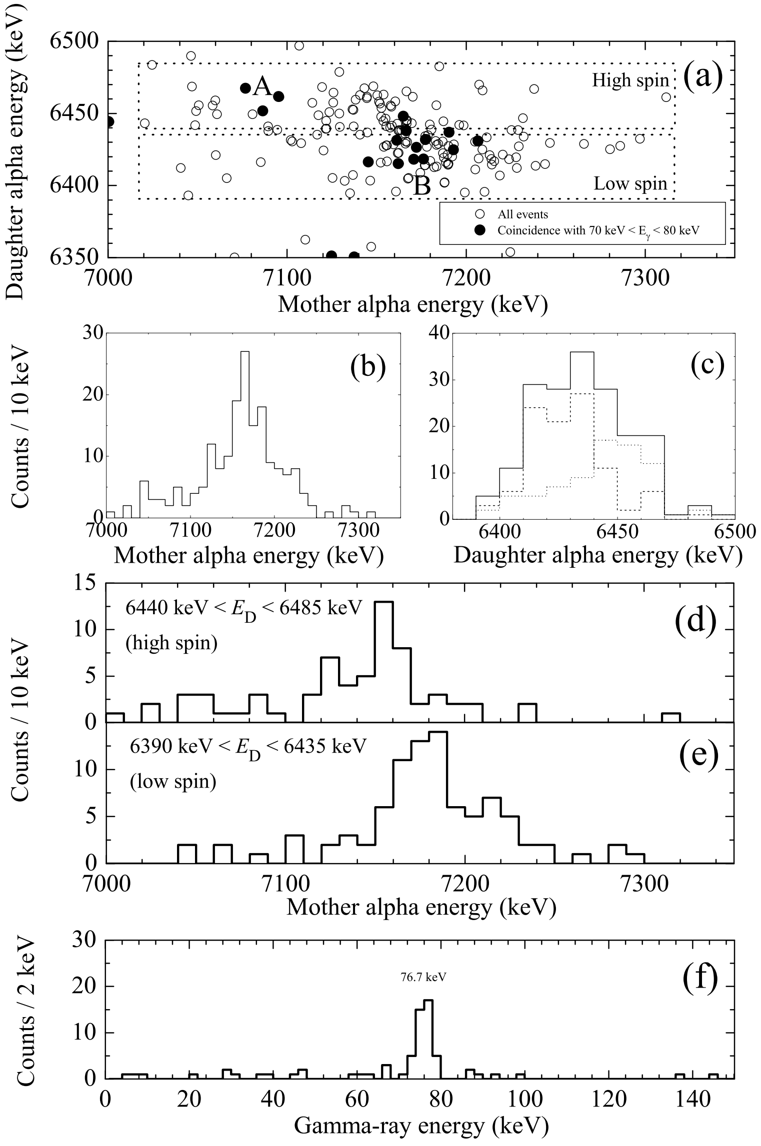

Figure 5.16: Panel (a) shows the portion of the alpha-alpha matrix around group 5 in figure 5.4. The filled circles correspond to events where the mother alpha decay is followed by a coincident gamma ray with energy between 70 keV and 80 keV. The group is divided to two parts: one associated with the decay of the high-spin isomer (10^-) and one with the low-spin isomer (3^+). The total projections of the events in panel (a) to the x- and y-axix can be seen in panels (b) and (c), respectively. The x-projections of the events in the slices marked with rectangles in panel (a) are presented in panels (d) and (e). Panel (f) shows the total gamma-ray spectrum of events following the mother alpha decays associated with ^{194}At. Both DSSDs were used in constructing the spectrum to increase statistics. The spectrum is gated with energy conditions $7000 < E_{\mathrm{M}} < 7350$ keV and $6350 < E_{\mathrm{D}} < 6500$ keV for the mother and daughter decays, respectively.

distinct peaks suggests that a large part of the events arise from alpha+electron sum signals.

Decay of the low-spin isomer in ^{194}At

The gamma-ray events associated with the alpha decay of the low-spin state in ^{194}At allow one alpha-particle energy to be fixed at $E = 7174(5)$ keV. This is based on the 12 events displayed with the filled circles in panel (a) of figure 5.16. The total number of events with $7140 < E_{\mathrm{M}} < 7210$ keV and $6410 < E_{\mathrm{D}} < 6450$ keV is 65. Given this fact, the expected number of 76 keV gamma rays detected for different multipolarities are 13(4) for an E1, 3(2) for an M1 and less than 1 for an E2. Thus, an E1 multipolarity can be assigned to the transition. Curiously the group of events coincident with the gamma rays appears to overlap with both the low-spin and high-spin alpha decay groups. This could be an artefact of low statistics or indicate a gamma-decay branch from the 3^+ state to the 10^- state in the daughter nucleus ^{190}Bi. The sum peak from the conversion electrons appears at around 7240 keV. In figure 5.16 there appears another peak at 7218(7) keV. This could be another alpha line or originate in part or fully from electron summing effects. There is no way to deduce the situation from the present data.

Calculating the alpha-decay hindrance factors for any single peak in the spectra presented in panels (d) and (e) of figure 5.16 gives $HF > 10$. This means that, unless summing effects due to the conversion electrons take away intensity from the peaks, there would be no unhindered alpha decays present in ^{194}At. Obviously this should not be the case and thus it is evident that a large portion of the events associated with the alpha decay of ^{194}At arise from alpha+electron sum signals.

The relative population of the high-spin and low-spin isomers can also be evaluated. Taking into account the respective beta-decay branches for the daughter nuclei the ratio between the population of the high-spin isomer to the total is $N(\mathrm{high})/N(\mathrm{total}) =$ 37(15) %.

Decay of the high-spin isomer in ^{194}At

The three events displayed with the filled circles visible in panel (a) of figure 5.16 and associated with the decay of the high-spin isomer in ^{194}At have a gamma-ray energy $E_{\gamma} = 75(2)$ keV. If these were gamma rays and not X-rays, thus coinciding with the full energy alpha peak, the multipolarity would again have to be E1 due to the large number of observed gamma-ray events relative to the number of alpha decays. Another possibility would be K X-rays from a highly converted transition. As the number of events is low, this is in agreement with the earlier conclusion that most of the events in the gamma-ray peak in figure 5.16 are not K X-rays. In the case of an alpha decay of 7050 keV followed by an M1 or E2 gamma ray with an energy in the region of 100 keV, then K X-rays would appear at around 7080 keV as seen in figure 5.16. The conversion coefficients are sufficiently high for the actual gamma-ray peak to go unobserved. However, it is still impossible to explain unambiguously the shape of the alpha spectrum in figure 5.16.

Various possible decay modes are discussed in chapter 6. A tentative decay scheme deduced from the present data is presented in figure 5.19.

Recent work regarding the alpha decay of ^{194}At

Very recently an article by Andreyev *et al.* was published that investigated the alpha decay of ^{194}At in detail [And09]. An extensive level scheme, identifying a total of eight alpha decay lines assigned to ^{194}At. The decay scheme presented in that work can be seen in figure 5.17. It contains features similar to the ones presented in this thesis. The 7190 keV alpha-particle energy followed by the 76 keV gamma ray and a highly converted 45 keV transition is somewhat higher than what is observed in the present work. As mentioned earlier, from the present data the alpha-particle energy (including possible electron summing effects) associated with the 76 keV gamma ray is 7174(5) keV. Regarding the decay of the high-spin isomer, the two highest intensity alpha lines in figure 5.17 are consistent with the interpretation given in this thesis, albeit again with slightly larger energies.

5.2.2 ^{196}At

The isotope ^{196}At was produced in the 2n evaporation channel of the ^{51}V + ^{147}Sm reaction. A total of 89 recoil - mother alpha - daughter alpha type events were collected during the experiment (group 6 in figure 5.4). From these data the following alpha decay properties for ^{196}At were determined: $E_\alpha = 7047(2)$ keV and $t_{1/2} = 350(40)$ ms. These values are consistent with the ones reported in [Smi00]: $E_\alpha = 7048(5)$ keV and $t_{1/2} = 388(7)$ ms. For the alpha decay of the daughter nucleus, ^{192}Bi, $E_\alpha = 6064(2)$ keV and $t_{1/2} = 18(2)$ s were obtained. The alpha decay energy is consistent with the decay of the 3^+ ground state of ^{192}Bi, $E_\alpha = 6060(5)$ keV, but the observed half-life is notably shorter than the literature value 34.6(9) s. In summary it appears that the only alpha decaying state present in ^{196}At is the low-spin 3^+ state, unlike in the neighbouring isotopes ^{198,194}At.

An isomeric state decaying via a 157.9(1) keV E2 gamma ray was reported in [Smi00].

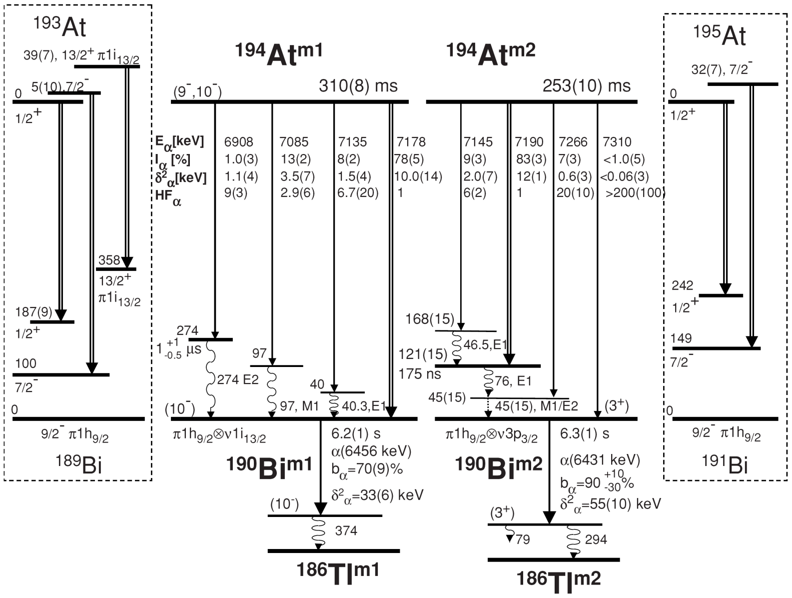

Figure 5.17: The proposed alpha-decay scheme of ^{194}At, taken from [And09].

The half-life for the transition was determined to be 7.6(1.4) μs. The energy and half-life deduced from the data of the present experiment are 157.5(9) keV and 4.0(7) μs. The half-life, determined by a least squares fit of the exponential decay curve to the data, is somewhat shorter than the one previously reported. The time and energy spectra are presented in figure 5.18. Based on the number of observed 158 keV gamma rays, assuming an E2 multipolarity, the population of the high-spin isomer can be estimated to be $N(\text{high})/N(\text{total})$ = 43(7) %, a very similar value to that deduced for ^{194}At.

In addition to the 158 keV gamma ray and astatine K X-rays, a 64(1) keV gamma ray is observed in the spectrum. Based on the observed intensity of the 64 keV gamma ray, the multipolarity of the transition is likely to be M1, assuming that the same amount of the total feeding (compared to the 158 keV transition) goes via the 64 keV transition. However, the half-life corresponding to the 64 keV transition is 11(3) μs, indicating that it possibly belongs to a different cascade than the 158 keV transition. Therefore the placement of this transition in the decay scheme cannot be deduced reliably from the present data. Further discussion about the decay of ^{196}At can be found in chapter 6. The tentative decay scheme based on the present work is presented in figure 5.19.

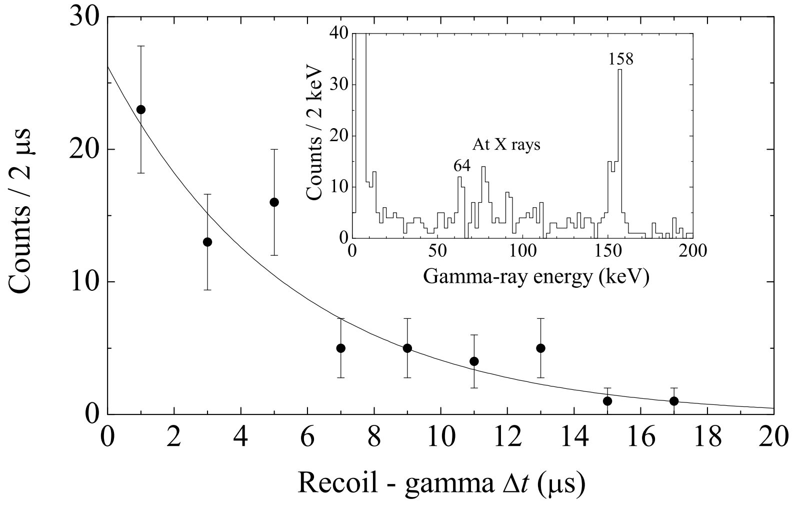

Figure 5.18: Time difference spectrum of the recoil formation and observation of the 158 keV gamma ray in the Planar detector. The exponential decay law was fitted to the data and is shown as the solid line. A gamma spectrum, tagged with the ^{196}At alpha decays and collected with the planar Ge-detector, is shown in the inset. The previously known 157.9(1) keV peak is clearly visible, as well as the new 64(1) keV one. Astatine X rays lie in between. The recoil-gamma search time was 100 μs.

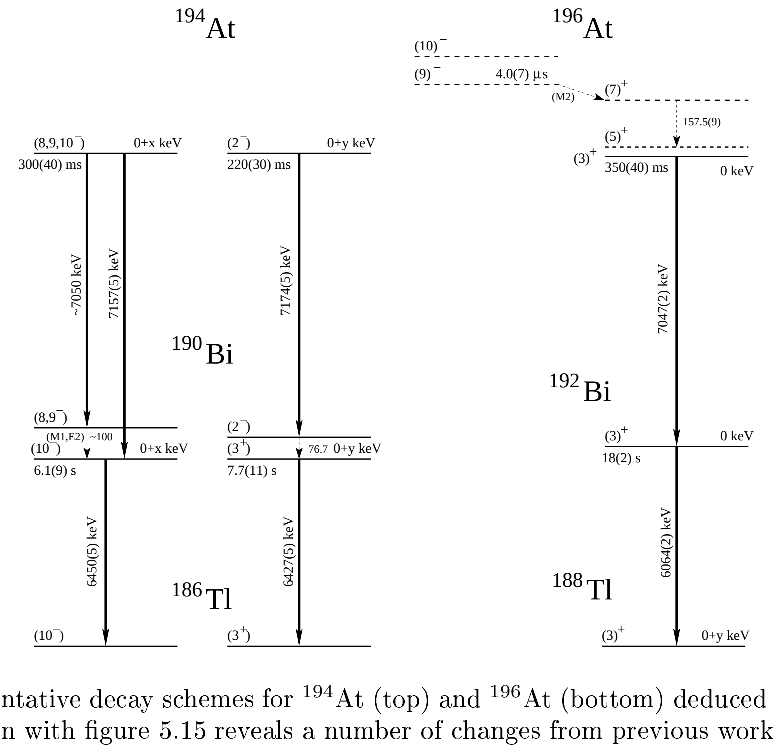

Figure 5.19: Tentative decay schemes for ^{194}At (top) and ^{196}At (bottom) deduced from the present data. Comparison with figure 5.15 reveals a number of changes from previous works.

6 Discussion

6.1 Superdeformation in ^{191}Bi

The observation of the two superdeformed rotational bands in ^{191}Bi marks the first time such bands have been detected from an alpha tagging experiment. Furthermore the isotope ^{191}Bi is by far the lightest bismuth isotope where the superdeformed minimum is observed (the second lightest is currently ^{195}Bi). As described in chapter 4 the two bands observed in ^{191}Bi were determined to be composed of E2 transitions indicating the rotation of a deformed nucleus and ruling out the shears mechanism as a foundation of the bands. The excitation energies could not be determined due to the non-observation of SD to ND linking transitions. The spins of the superdeformed states can be evaluated even in the absence of observable linking transitions to states with known spins. This is because the energy equation for a rigid rotor (equation 2.5) is quite sensitive at low spins. Level spin determination for superdeformed bands is discussed in references [Wu92], [Bec92] and [Wu97]. Retaining only the first order terms, equation 2.5 takes the form

$$E = \frac{\hbar^2}{2\mathcal{J}} \left[I(I+1) - K^2 + a(-1)^{I+1/2}(I+1/2)\delta_{K,1/2} \right] \ . \tag{6.1}$$

The gamma-ray energy $E(I) - E(I-2)$ solved from this can then be fitted to the observed energies with different assumptions for the spin of the lowest observed state. The correct spin values correspond to the best fit. The goodness of the fit is evaluated using the root mean square deviation (equation 6.2). For example in [Wu92] values of $\sigma_{\mathrm{rms}} \lesssim 0.002$ were typically achieved for good fits.

$$\sigma_{\mathrm{rms}} = \sqrt{\frac{1}{\mathrm{n}} \sum_{\mathrm{i}=1}^{\mathrm{n}} \left(\frac{E_\gamma^{\mathrm{cal}}(I_\mathrm{i}) - E_\gamma^{\mathrm{exp}}(I_\mathrm{i})}{E_\gamma^{\mathrm{exp}}(I_\mathrm{i})} \right)^2} \tag{6.2}$$

Fits performed in this manner, assuming $K \neq 1/2$, indicated a spin of 11/2 and 9/2 for the lowest observed levels in bands 1 and 2, respectively.

Energies for superdeformed states in Au - Ra nuclei have been calculated using the

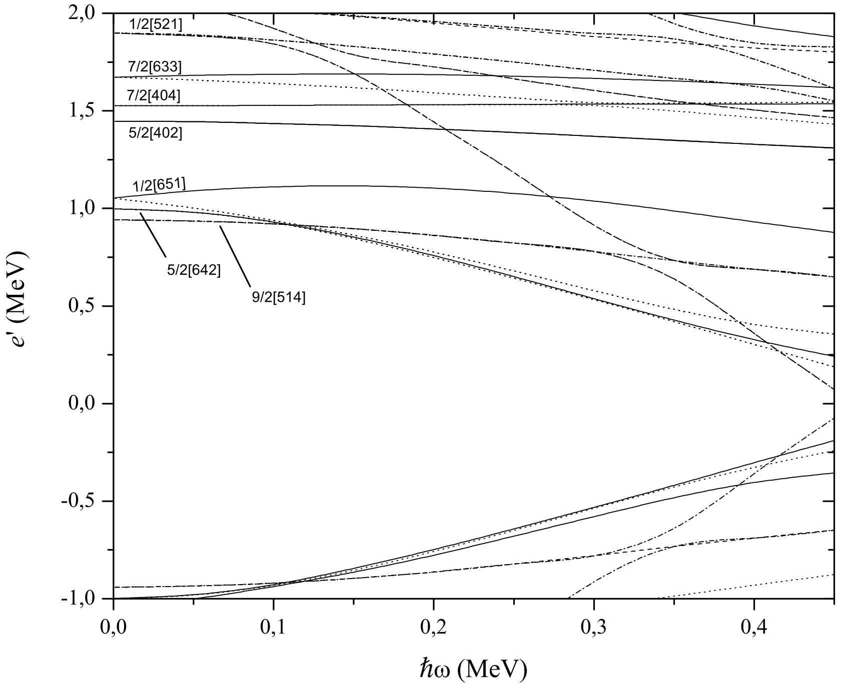

Figure 6.1: Quasiproton level energies in the superdeformed regime for ^{191}Bi using a Woods-Saxon potential and universal parameters. The values for deformation parameters were chosen to be in accordance with [Sat91]: $\beta_2 = 0.47$ and $\beta_4 = 0.07$. The parities and signatures are labelled as follows: $(\pi, \alpha) = (+, +1/2)$ solid, (+,-1/2) dotted, (-,+1/2) dot-dashed, (-,-1/2) dashed.

Strutinsky shell correction method with an average Woods-Saxon potential and a monopole pairing interaction [Sat91]. These calculations place the following five orbitals close to the Fermi-surface in ^{191}Bi: 5/2[642], 9/2[514], 1/2[651], 7/2[404] and 5/2[402]. Cranking calculations using a program from [Pau99] were performed to illustrate the behaviour of these orbitals as a function of rotation. The resulting quasiproton levels are displayed in figure 6.1. The level ordering is different to that in figure 2.1 due to the nonzero value for β_4.

Of the orbitals mentioned above 5/2[642] and 5/2[402] are ruled out as they would produce a strongly coupled band with $\alpha = +1/2$ as the favoured signature. As mentioned in chapter 4, bands 1 and 2 appear not to be connected. In the case of the relatively high-K 9/2[514] orbital the lowest transitions in SD bands 1 and 2 would have to be the transitions feeding the $\alpha = -1/2$ and $\alpha = +1/2$ bandheads, respectively. In this case a satisfactory fit to the data cannot be achieved. Furthermore, no signature splitting is expected for this orbital, as can be seen in figure 6.1. The orbital is also not β_2 driving, meaning that its energy increases with increasing deformation, see figure 2.5. This leaves the 1/2[651] and 7/2[404] orbitals as the only viable choices. If one assumes that the observed two bands are the favoured signatures of bands built on top of these states, it is only possible to get a reasonably good fit for one or the other of the two bands, but not for both. In fact, in order to achieve a good fit to the transition energies of band 1, a second order term needs to be added to equation 6.1 or the *ab*-formula has to be used. This points towards both bands originating from the same orbital. Assuming the 7/2[404] orbital and fitting both bands simultaneously a good fit turns out to be unobtainable, even when using the second order term. And finally, the 7/2[404] orbital is also not β_2 driving and no signature splitting is expected.

This leaves the 1/2[651] orbital as the final candidate. It is the only one of the orbitals exhibiting signature splitting and thus resulting in a decoupled band structure. For a $K = 1/2$ band a correction term including the decoupling parameter a needs to be included, as indicated in equation 6.1. This term makes it possible to achieve a good fit for both bands with the same fitting parameters. This allows the observed bands to be assigned to originate from the 1/2[651] Nilsson level. As the two parameters in equation 6.1 are connected to each other, it is not possible to unambiguously fit both of them. Therefore the decoupling parameter was evaluated first. By using a value of $\hbar^2/2\mathcal{J} \approx 5$ keV, appropriate for a superdeformed nucleus in this mass region, it can be deduced that values for the decoupling parameter of $a \sim -1.6$ result in reasonable description for the observed transition energies. Fitting equation 6.1 with the rotation parameter fixed at a value of $\hbar^2/2\mathcal{J} \approx 5$ yields different values for the decoupling parameter with different spin assumptions. Again, the spins 11/2 and 9/2 for the lowest observed levels in bands 1 and 2 are the only ones that produce values for the decoupling parameter close to the expected value $a \sim -1.6$. The value for the rotation constant $\hbar^2/2\mathcal{J}$ was then varied and the one producing the best fit was determined. Finally both bands were fitted simultaneously using the same procedure. It turns out that this is the only case where it was possible to obtain a satisfactory fit for both bands using the same fitting parameters, supporting the idea that the observed bands are indeed the two signature parners originating from the 1/2[651] orbital. The relevant parameters from the various fits are collected to table 6.1 for comparison.

Furthermore, estimating the $B(\mathrm{M1})/B(\mathrm{E2})$ ratios from the unfavoured band to the favoured one using the Dönau-Frauendorf formula, equation 6.4, [Dön83] [Dön87], yields typical values of $< 0.01\ \mu_{\mathrm{N}}/\mathrm{e}^2\mathrm{b}^2$. This is in accordance with the observation that the two bands are not in coincidence with each other, i.e. the interband M1 transitions are very weak.

A good parameter in comparing different SD bands is the dynamic moment of inertia $\mathcal{J}^{(2)}$ (equation 2.17), which only depends on the transition energies. The kinematic moment of inertia $\mathcal{J}^{(1)}$ (equation 2.16) often cannot be used as the spins of the

Table 6.1: Comparison of fits with different functions and configuration assumptions for the two superdeformed bands. The functions used were the rotor formula (equation 2.5) with and without the $[I(I+1)-K^2]^2$ term. For $K = 1/2$ the equation includes the decoupling term. Also the *ab*-formula (equation 2.8) was used.

Band	Configuration	Function	σ_{rms}
1	7/2[404]	1st order	0.0260
2			0.0060
Both			0.0210
1	7/2[404]	2nd order	0.0034
2			0.0023
Both			0.0195
1	7/2[404]	*ab*	0.0032
2			0.0023
Both			0.0194
1	1/2[651]	1st order	0.0037
2			0.0041
Both			0.0092

SD levels are not known. Panel (a) of figure 6.2 gives a comparison of the dynamic moment of inertia between various SD bands observed in the $A \sim 190$ region and the two bands discovered in the present work. It can be seen that the bands follow closely the systematic trends of the other known SD bands in the region. Panel (b) shows the kinematic moment of inertia calculated for both bands in ^{191}Bi based on the level spin determination discussed above. Also, two examples in this mass region where the spins of the SD bands have been determined accurately by observing the SD to ND linking transitions are shown for comparison. The slopes of the kinematic moment of inertia for the two SD bands observed in ^{191}Bi differ from the others shown in the figure. This is due to the signature splitting. However, a finite initial alignment will also affect the slope of $\mathcal{J}^{(1)}$. This is discussed for instance in reference [Sie04]. In terms of the Harris parameters J_0 and J_1 the kinematic moment of inertia can be written as

$$\mathcal{J}^{(1)} = J_0 + J_1\omega^2 + i/\omega \ , \tag{6.3}$$

where i is the quasiparticle alignment. However, it is not clear if this effect on the kinematic moment of inertia can be separated from that of the signature splitting. Should there be a finite initial alignment present, the validity of the spin determination procedure could be questioned. In the present case the 1/2[651] configuration assignment for the SD bands is supported by the experimental observation that the bands are not strongly coupled.

The transition intensities of the superdeformed bands are displayed in figure 6.3. Typically, the intensity pattern of a superdeformed band shows a sharp drop at the lowest observed spins as the decay out of the SD minimum occurs. This is not apparent from figure 6.3, which would indicate that most of the decay out occurs below the lowest observed level. The bandhead spins for bands 1 and 2 are 3/2 and 1/2, respectively, if they are indeed built on the 1/2[651] Nilsson orbital. The dropping intensities towards the high spin part of the bands are indicative of the bands becoming yrast. This is the region where the bands are populated in the heavy ion fusion reaction. This populating region seems to be quite large, possibly indicating the bands becoming yrast at relatively low spins. However, an experiment with improved statistics would be needed to accurately assess the transition intensities.

6.2 Normally deformed states in ^{191}Bi and ^{195}At

6.2.1 Kinematic moments of inertia

The kinematic moment of inertia offers a means to compare the properties of different rotational bands. The kinematic moment of inertia for known prolate rotational bands is typically about 15 $\hbar^2$/MeV larger than for oblate bands (for typical deformation values), and this systematic behaviour can be used to distinguish between oblate and prolate deformation.

The rotational bands in ^{191}Bi and ^{195}At from the present work are presented in figure 6.4. For comparison the kinematic moments of inertia for the corresponding bands in ^{193}Bi and two known examples of prolate and oblate bands in neighbouring even-even nuclei are also shown. It can be seen that broadly speaking the $\mathrm{i}_{13/2}$ band in ^{191}Bi follows the behaviour of the corresponding band in ^{193}Bi, although its moment of inertia is slightly larger. Both of the $\mathrm{i}_{13/2}$ bands lie between the oblate and prolate regions, which indicates increasing oblate deformation. As reported in reference [Hür04a] the $\mathrm{i}_{13/2}$ bands in ^{187,189}Bi are observed to be decoupled indicating prolate deformation. The $h_{9/2}$ bands in ^{191,193}Bi lie closer to the known oblate bands, again the moment of inertia being slightly larger for ^{191}Bi than ^{193}Bi. Both the $\mathrm{i}_{13/2}$ and $\mathrm{h}_{9/2}$ bands in ^{191}Bi show evidence of a band crossing due to the alignment of a neutron pair in the $\mathrm{i}_{13/2}$ orbital. The moment of inertia of the $\mathrm{i}_{13/2}$ band in ^{195}At is larger than those observed in ^{191,193}Bi, actually lying higher than the two prolate bands included in figure 6.4. This is consistent with the TRS calculations presented in [And08], predicting a relatively large deformation for the $\mathrm{i}_{13/2}$ configuration.

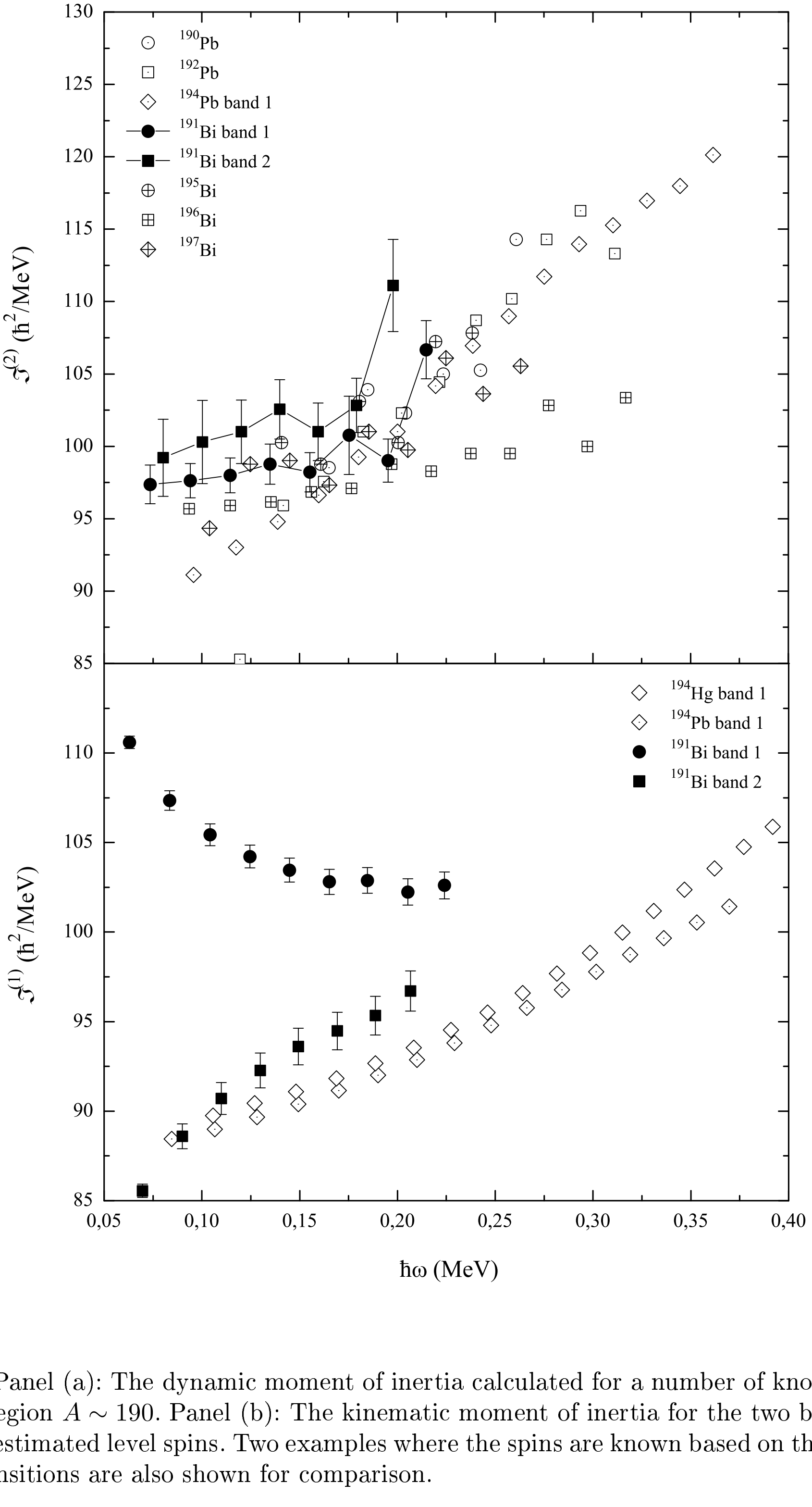

Figure 6.2: Panel (a): The dynamic moment of inertia calculated for a number of known SD bands in the mass region $A \sim 190$. Panel (b): The kinematic moment of inertia for the two bands in ^{191}Bi based on the estimated level spins. Two examples where the spins are known based on the observation of linking transitions are also shown for comparison.

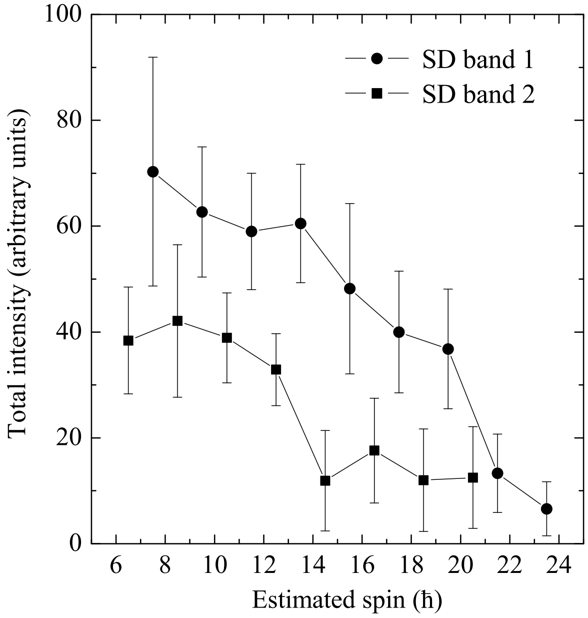

Figure 6.3: The relative transition intensities of the two SD bands observed in ^{191}Bi. The intensities are corrected for internal conversion assuming E2 multipolarity.

The $s_{1/2}$ bands seem to show significant changes with decreasing neutron number. In ^{193}Bi the band appears irregular, although the limited statistics of that experiment ([Nie04]) make the level scheme tentative. The lighter isotopes show collective bands where the signature splitting appears to increase when going from ^{191}Bi to ^{189}Bi. The data for ^{189}Bi, as reported in [Hür04b], is also of very low statistics and consequently the decduced level scheme remains unpublished. The $s_{1/2}$ band in ^{193}Bi exhibits a very low kinematic moment of inertia, lying below the known oblate bands. The moment of inertia then increases drastically in ^{189}Bi. The excitation energies of the $1/2^+$ intruder states in odd-mass bismuth isotopes shows a clear departure from the expected parabolic behaviour with respect to the neutron midshell [And04a]. This indicates that the structure of the $1/2^+$ intruder states in the lightest odd-mass Bi nuclei is different from those in the heavier ones. As discussed in reference [Nie04] alpha decay data are consistent with oblate deformation for the $1/2^+$ intruder states in ^{191,193}Bi. Therefore the observed band feeding the alpha-decaying $1/2^+$ state in ^{191}Bi would not be based on the oblate 2p-1h $1/2^+$ state, but a prolate or triaxial configuration.

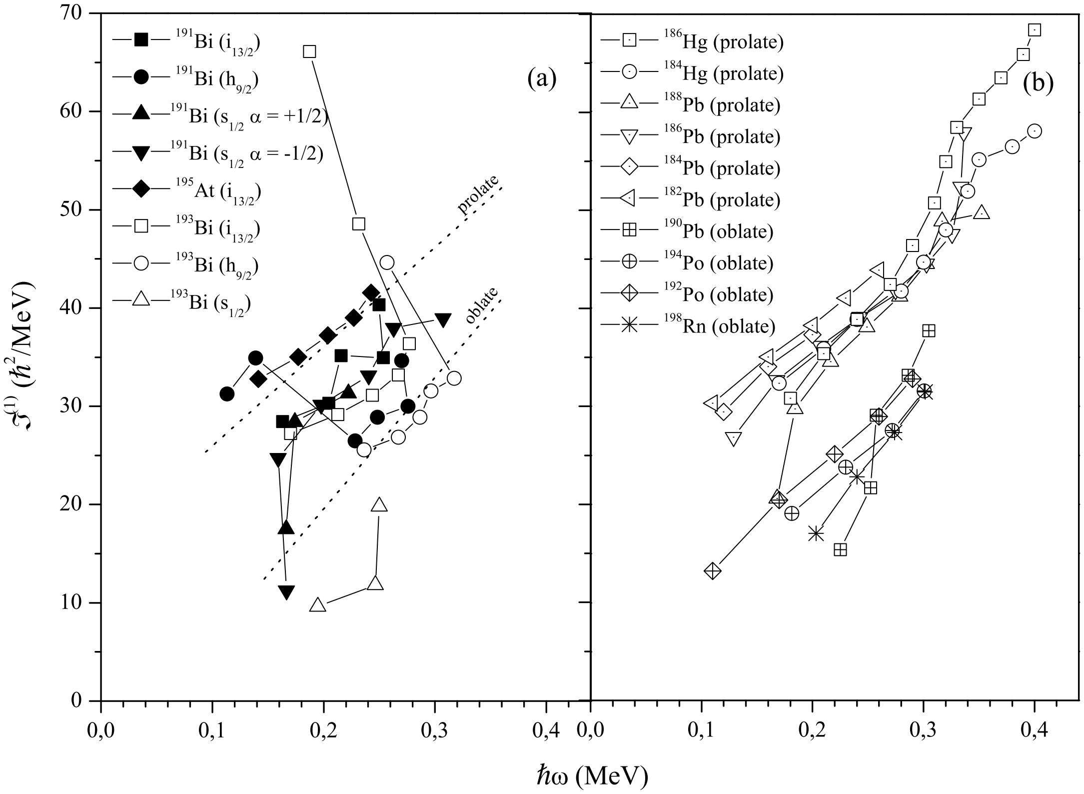

Figure 6.4: Panel (a): Kinematic moments of inertia determined for the bands observed in ^{191}Bi and ^{195}At in this work. Corresponding bands in ^{193}Bi are shown for comparison. Panel (b) displays some examples of known prolate and oblate bands in this mass region. These typical values for $\mathcal{J}^{(1)}$ are indicated in panel (a) by the dotted lines. Data is taken from [Nie04] (^{193}Bi), [Ma93] (^{186}Hg), [Ma86] (^{184}Hg), [Dra98] (^{190}Pb), [Dra04] (^{188}Pb), [Pak05b] (^{186}Pb), [Coc98] (^{184}Pb), [Jen00] (^{182}Pb),[Hel99] (^{194,192}Po) and [Tay99] (^{198}Rn).

6.2.2 Comparisons of aligned angular momenta

The aligned angular momentum, equation 2.13, measures the contribution of the quasiparticle(s) to the total angular momentum. The known oblate band in ^{192}Po was chosen as the rotating reference. The resulting values for the Harris parameters were $J_0 = 11.7\ \hbar^2/\mathrm{MeV}$ and $J_1 = 261.4\ \hbar^4/\mathrm{MeV}^3$.

Panel (a) of figure 6.5 contains the aligned angular momenta for the $\mathrm{i}_{13/2}$ bands (both signatures) observed in ^{191}Bi and ^{195}At from this work. The corresponding band in ^{193}Bi is also included for comparison. The bands in both Bi isotopes show a roughly similar behaviour, with the lower values for i_{x} occurring in ^{193}Bi. This is consistent with a somewhat lower deformation for ^{191}Bi. The alignment gain of about 11 $\hbar$ for ^{193}Bi visible in panel (a) of figure 6.5 was interpreted as being caused by the alignment of an $\mathrm{i}_{13/2}$ neutron pair in reference [Nie04]. A similar behaviour is now observed in ^{191}Bi, for the same reason. The $\mathrm{i}_{13/2}$ band in ^{195}At has slightly larger values for the aligned angular momentum, consistent with a slightly larger deformation. In the case of ^{195}At the current data does not extend to the rotational frequencies where the backbending occurs in bismuth nuclei.

Panel (b) of the figure presents the alogned angular momentum for the negative parity bands in ^{191,193}Bi. Again their behaviour is roughly similar, with both showing evidence of a band crossing similarly to the $\mathrm{i}_{13/2}$ bands. The confirmation of this would require the observation of the bands to higher spins than reached in the present work. Panel (c) of figure 6.5 show the aligned angular momentum for bands 3 and 4 in ^{191}Bi compared to those calculated for the bands feeding the $1/2^+$ state in ^{189}Bi, as tentatively reported in reference [Hür04b]. The values for ^{191}Bi are smaller, indicating a smaller deformation.

6.2.3 B(M1)/B(E2) ratios

Some insight into the single-particle orbital on which a strongly coupled band is based can be achieved by examining the ratios of transition probabilities of the competing M1 and E2 transitions. These can be estimated theoretically by a geometrical model developed by Dönau and Frauendorf [Dön83] [Dön87]. The formula is

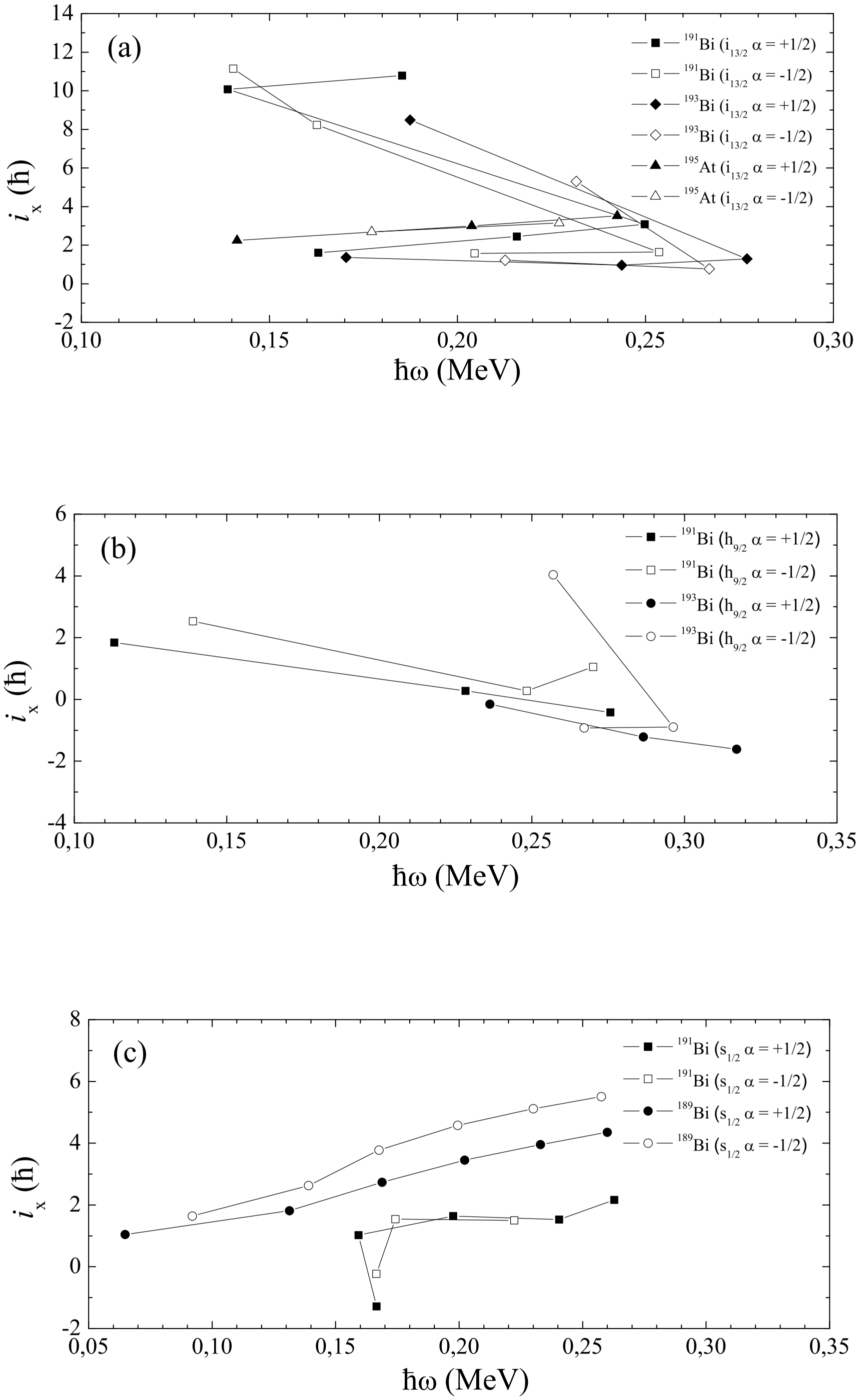

Figure 6.5: Aligned angular momenta for various rotational bands in ^{189,191,193}Bi and ^{195}At. The different signatures ($\alpha = +1/2$ and $\alpha = -1/2$) are displayed with filled and open symbols, respectively. (a) A comparison between $i_{13/2}$ bands in ^{191}Bi, ^{195}At and ^{193}Bi, (b) the same comparison for the $h_{9/2}$ bands in ^{191}Bi and ^{193}Bi, (c) the $s_{1/2}$ bands found in ^{191}Bi compared to the tentative signature partners observed in ^{189}Bi [Hür04b].

$$\begin{aligned}\frac{B(\mathrm{M1})}{B(\mathrm{E2})} &= \frac{12}{5Q_0\cos^2(\gamma+30^\circ)}\left(1-\frac{K^2}{(I-1/2)^2}\right)^{-2} \\ \times\left(1-\frac{K^2}{I^2}\right)^{1/2} &\left[\Omega_1(g_1-g_{\mathrm{R}})\left(1\pm\frac{\Delta e'}{\hbar\omega}\right)^2+\sum_{\mathrm{n}=2}^{\mathrm{N}}\Omega_{\mathrm{n}}(g_{\mathrm{n}}-g_{\mathrm{R}})\right] \\ &-\frac{K}{I}\left[(g_1-g_{\mathrm{R}})i_1+\sum_{\mathrm{n}=2}^{\mathrm{N}}(g_{\mathrm{n}}-g_{\mathrm{R}})i_{\mathrm{n}}\right]\ . \end{aligned} \tag{6.4}$$

The parameter γ is defined by the Lund convention (see Chapter 2) and Ω_{n}, g_{n} and i_{n} refer to the Ω, g-factor and aligned angular momentum of the quasiparticles involved in the calculation with n=1 denoting the particle causing the signature splitting. The rotational g-factor can be approximated by $g_{\mathrm{R}} \approx Z/A$. The sign of the signature splitting term $\Delta e'/(\hbar\omega)$ is positive for transitions from the unfavoured signature to the favoured one and negative for the other way around. The single-particle g-factors can be calculated from

$$g_{\mathrm{n}} = g_l \pm \frac{1}{2l+1}(0.6g_s^{\mathrm{free}} - g_l)\ , \tag{6.5}$$

where the plus sign is for orbitals with $j = l + 1/2$ and minus sign for $j = l - 1/2$. The orbital and spin g-factors for protons and neutrons are

$$\begin{aligned} g_l = 1, &\quad g_s^{\mathrm{free}} = 5.5856 \quad \text{(protons)} \\ g_l = 0, &\quad g_s^{\mathrm{free}} = -3.8262 \quad \text{(neutrons)}\ . \end{aligned}$$

Finally, the intrinsic quadrupole moment for rotational quadrupoloid is related to the deformation parameter β_2 by

$$Q_0 \approx 0.757ZR^2\beta(1+0.36\beta)\ , \tag{6.6}$$

where $R \approx 1.275A^{1/3}$ fm.

To extract the $B(\mathrm{M1})/B(\mathrm{E2})$ ratio from the experimental data the following equation is used

$$\frac{B(\mathrm{M1})}{B(\mathrm{E2})} = 0.697\frac{E_\gamma^5(\mathrm{E2})I_\gamma(\mathrm{M1})}{E_\gamma^3(\mathrm{M1})I_\gamma(\mathrm{E2})(1+\delta^2)}\ . \tag{6.7}$$

The E2/M1 mixing ratio δ is zero for the $I = 1$ transitions, as they are assumed to be pure M1 transitions.

The experimental and calculated $B(\mathrm{M1})/B(\mathrm{E2})$ ratios for some rotational bands observed in ^{189,191}Bi and ^{195}At are presented in figure 6.6. The positive and negative parity bands feeding the $9/2^-$ ground states in ^{191,193}Bi were analyzed in the manner explained above in [Nie04] and the results supported the configuration assignments $\mathrm{i}_{13/2}$ and mixed $\mathrm{f}_{7/2}/\mathrm{h}_{9/2}$. The observation of the unfavoured signature band feeding the $1/2^+$ intruder state makes it possible to perform the analysis for the $\mathrm{s}_{1/2}$ band as well. The M1 transitions are observed only from the unfavoured to the favoured band with the possible exception of the tentative $5/2^+$ to $3/2^+$ transition due to the signature splitting. This seems to be the case also in ^{189}Bi, as reported in [Hür04b].

The experimental and calculated $B(\mathrm{M1})/B(\mathrm{E2})$ values for the $\mathrm{i}_{13/2}$ band in ^{191}Bi are in good accordance. The experimental values reported for this band in the earlier work [Nie04] lie somewhat lower than the calculated ones. A triaxial shape was introduced as a possible explanation. With the improved statistics of the present work the experimental values seem to be larger than previously reported and a good agreement with theoretical predictions is reached. This does not exclude the possibility of some axial asymmetry but in light of the present data it is not needed in describing the yrast band of ^{191}Bi. The corresponding band in ^{195}At exhibits smaller $B(\mathrm{M1})/B(\mathrm{E2})$ values. An agreement between calculations and the experimental data can be reached by increasing the deformation to $\beta_2 \sim -0.3$, as has been done in figure 6.6. This is already atypically large deformation for oblate bands in this mass region. Alternatively the triaxial shape mentioned above can be used to explain the small $B(\mathrm{M1})/B(\mathrm{E2})$ values, as it tends to decrease the effective value of K.

The data for the $\mathrm{h}_{9/2}$ bands in ^{191,193}Bi showed $B(\mathrm{M1})/B(\mathrm{E2})$ values close to 1 $\mu_\mathrm{N}/\mathrm{e}^2\mathrm{b}^2$. To produce these theoretically a mixed $\mathrm{f}_{7/2}/\mathrm{h}_{9/2}$ character for the bands was necessary to be assumed, as the values for a pure $\mathrm{h}_{9/2}$ configuration yielded too low values. The g-factor for the mixed configuration was taken to be $g_1 = 1.16$ and the same value was used in the present work. The mixed nature of the 7/2[514] Nilsson orbital has also been proposed to be the cause of the observed large $11^- \rightarrow 8^+$ transition probabilities in ^{190,192}Pb [Dra01]. This mixing is also very evident from the Nilsson diagram, figure 2.5.

The $B(\mathrm{M1})/B(\mathrm{E2})$ values for the $\mathrm{s}_{1/2}$ bands in ^{189,191}Bi are an order of magnitude smaller than those observed for the other bands discussed above, as expected for an $\mathrm{s}_{1/2}$ configuration. The calculated values in figure 6.6 include the signature dependent term in equation 6.4, mainly to illustrate its effect. The other bands discussed above were calculated at the strong coupling limit ($\Delta e' = 0$). The values for ^{191}Bi and ^{189}Bi are very similar and the calculations agree very well with the experiment.

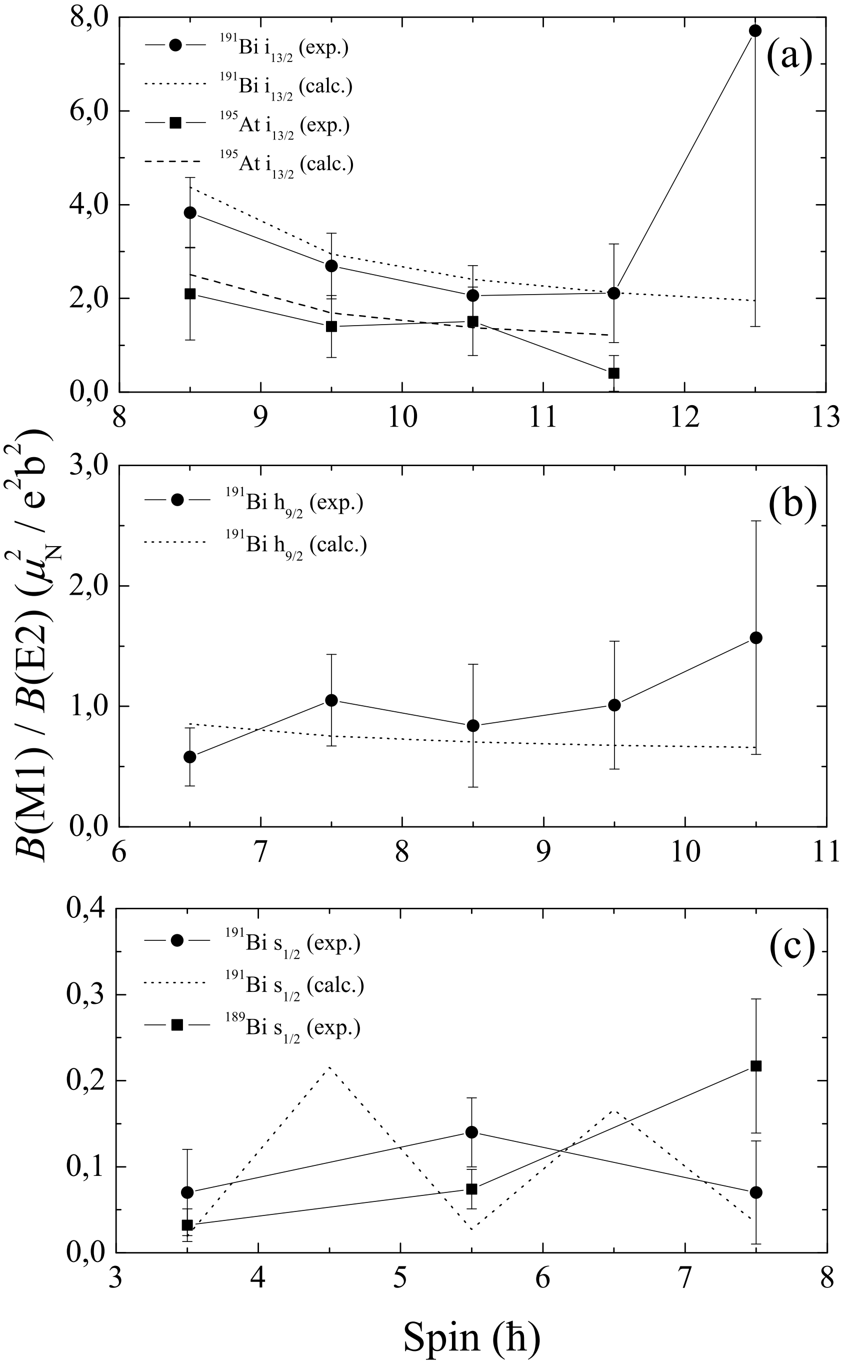

Figure 6.6: Experimental and calculated B(M1)/B(E2) ratios for the $i_{13/2}$ (a), $h_{9/2}$ (b) and $s_{1/2}$ (c) bands in ^{191}Bi and ^{195}At. The tentative experimental values for the $s_{1/2}$ band in ^{189}Bi are also provided for comparison. The parameter values used for the calculated values are included in table 6.2. The calculations for the $i_{13/2}$ and $h_{9/2}$ bands were calculated at the limit of strong coupling (i.e. $\Delta e' = 0$), whereas the signature splitting term was included in the calculation for the $s_{1/2}$ band in ^{191}Bi, mainly just to illustrate its effect.

Table 6.2: Values of the various parameters that were used to calculate the theoretical $B(\mathrm{M1})/B(\mathrm{E2})$ estimates in figure 6.6.

	^{191}Bi $\mathrm{i}_{13/2}$	^{195}At $\mathrm{i}_{13/2}$	^{191}Bi $\mathrm{h}_{9/2}$	^{191}Bi $\mathrm{s}_{1/2}$
β_2 (eb)	-0.23	-0.30	-0.18	0.25
K	13/2	13/2	7/2	1/2
i_1	1/2	1/2	1/2	1/2
g_1	1.18	1.18	1.16	3.35
$\Delta e'$ (MeV)	0	0	0	-0.04

6.3 Decay spectroscopy of ^{194,196}At

As explained in chapter 5 only one alpha decay line was observed in ^{196}At, consistent with a decay from the 3^+ state to the corresponding state in ^{192}Bi. This is in contrast to the heighbouring odd-odd astatine isotopes, where alpha decays from both low-spin (3^+) and high-spin (10^-, 7^+) states occur. In order to understand this behaviour the the energies of some low-lying states in odd-odd astatine isotopes were estimated. The odd proton and neutron couple their angular momenta to form a multiplet of states with spins $|I_\mathrm{p} - I_\mathrm{n}| \leq I \leq I_\mathrm{p} + I_\mathrm{n}$. This coupling of angular momenta in odd-odd nuclei was first studied by Nordheim [Nor50]. Further coupling rules were later introduced by Gallagher and Moszkowski in reference [Gal58]. One of the rules states that for a nucleus with proton (neutron) outside a closed shell and a neutron (proton) hole in a shell the lowest member of the multiplet has a spin $I = j_\mathrm{p} + j_\mathrm{n} - 1$. A more general method for determining the lowest multiplet member is the parabolic rule given in reference [Paa79]. A simple way to estimate this energy is to obtain the excitation energies of the relevant proton and neutron orbitals from neighbouring odd-even and even-odd nuclei and adding them together. Figure 6.7 shows the results of such analysis. The proton and neutron single-particle energies were obtained from the neighbouring Po and Rn nuclei, respectively. The energy of the coupled proton-neutron system was then computed using both lighter and heavier neighbours and an average value taken for then odd-odd nucleus. If sufficient data did not exist for both (N-1,Z-1) and (N+1,Z+1) nuclei, whichever value was possible to extract was taken as a substitute for the average. When viewing figure 6.7 it must also be remembered that only the lowest member of each multiplet is shown. The actual level density is thus higher than might be thought from the figure. Also some of the proton and neutron level energies were obtained from level systematics rather than actual experimental data with corresponding large uncertainties. As a result the error bars for some of the data points can range up to ±100 keV. Considering the crudeness of the estimates and in the interests of clarity these are not included in the figure. Experimental data in the odd-odd astatine nuclei are scarce, but energies for some of the states can be found in the literature and are included in the figure for comparison. They reveal a surprisingly good agreement with the estimated energies. Even in the cases where the agreement is not the best, the discrepancies are only of the order of 100 keV. The most obvious feature, which is apparent in the figure, is the increasing level density in the lighter isotopes. With the addition of other members of each multiplet the density increases further and as a consequence the energies of gamma-ray transitions between excited states are likely to be low. This is also supported by the non-observation of strong gamma-ray transitions preceeding the alpha decays.

In ^{196}At the ground state is expected to have a spin-parity of 3^+, with a 2^- state lying very close. The 10^- state observed to alpha decay in ^{198}At is predicted to rise in energy in ^{196}At. Therein lies the possible explanation to the non-observation of the alpha decay from this state. As can be seen from figure 6.7 the $(\pi 2\mathrm{f}_{7/2} \otimes \nu 1\mathrm{i}_{13/2})9^-$ state is expected to be below the 10^- state. This together with the two possible 7^+ states and the lower spin levels displayed in the figure provide a gamma-decay path with fast $\Delta I \leq 2$ transitions with which the alpha decay cannot compete. Additionally the strongly downsloping $(\pi 1\mathrm{i}_{13/2} \otimes \nu 2\mathrm{f}_{5/2})9^-$ state is also expected to appear below the 10^- level. Thus the only alpha decaying state in ^{196}At would be the $(\pi 1\mathrm{h}_{9/2} \otimes \nu 3\mathrm{p}_{3/2})3^+$ state, which is strongly supported by the experimental data. The 158 keV E2 gamma ray observed to preceed the alpha decay could perhaps arise from the $7^+ \rightarrow 5^+$ transition, its half-life being determined by the preceeding slower $9^- \rightarrow 7^+$ M2 transition. The observed half-life for the 158 keV transition, 4.0(7) μs is consistent with the Weisskopf estimate for a ∼50 keV M2 transition, which would remain unobserved in the present experiment.

In ^{194}At the ground state does not necessarily have a spin-parity of 3^+ anymore, although the same three low-spin states as in ^{196}At are expected to lie low in energy. The 10^- state is expected to lie even higher in energy than the one in ^{196}At and would not alpha decay for the same reasons. The observation of an alpha decay feeding a high-spin state in ^{190}Bi therefore has to involve another configuration. As can be seen from the figure 6.7 there are two candidates below 150 keV: the $(\pi 1\mathrm{i}_{13/2} \otimes \nu 3\mathrm{p}_{3/2})8^-$ and $(\pi 1\mathrm{i}_{13/2} \otimes \nu 2\mathrm{f}_{7/2})9^-$ levels. Either of these could be the lowest within the uncertainties. In any case a gamma transition to the 5^+ state cannot compete with the alpha decay feeding the corresponding configuration in ^{190}Bi. Based on figure 6.7 the alpha decaying low-spin state in ^{194}At is the 2^- state. The 76 keV E1 gamma ray observed to follow the alpha decay would then naturally be explained by a $2^- \rightarrow 3^+$ transition in ^{190}Bi. Also the alpha decay of ^{192}At has been observed not to feed directly the 3^+ and 10^- states in the daughter nucleus ^{188}Bi, as reported in [And06].

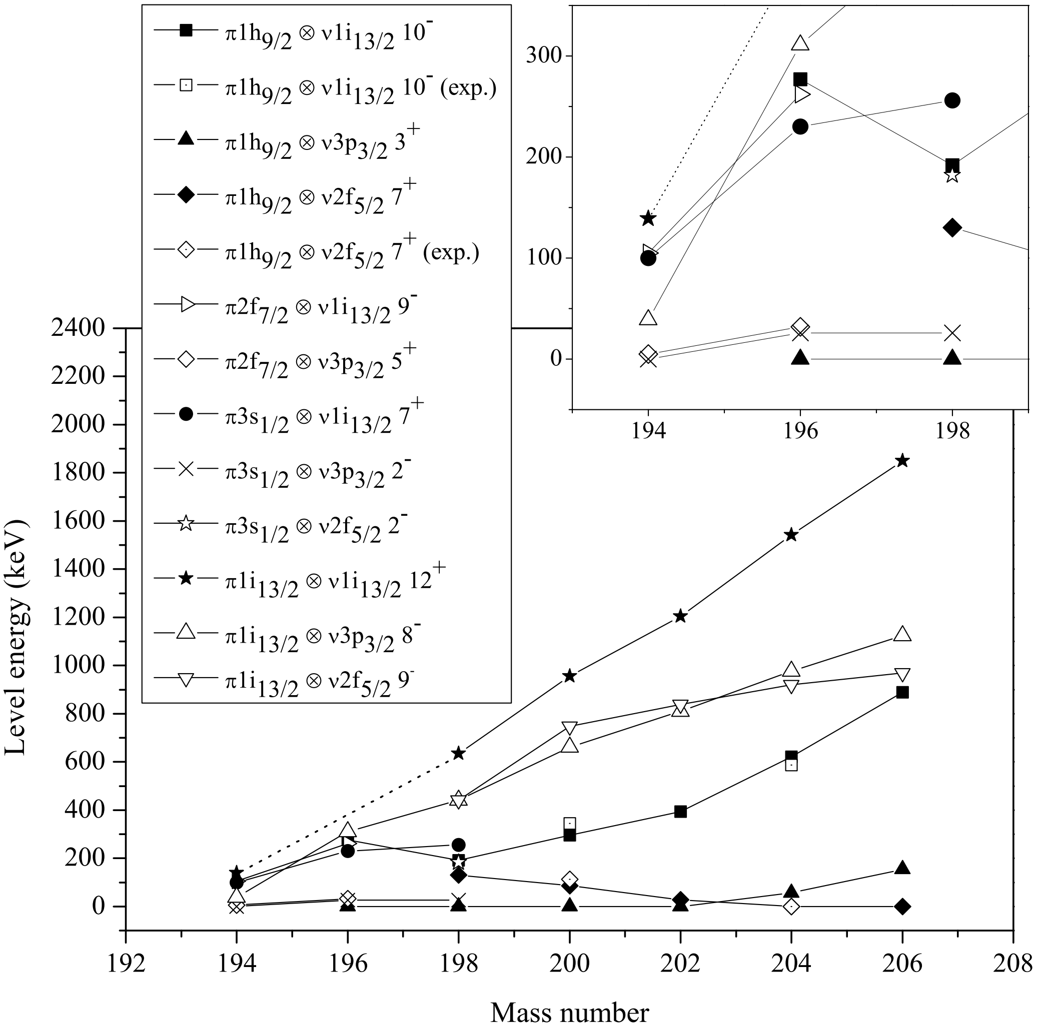

Figure 6.7: Estimated level energies for the expected lowest members of some proton-neutron multiplets occurring in odd-odd astatine isotopes. The method by which the energies were computed is explained in the text. An enlargement of the area interesting for the present work is displayed in top right. The configurations and the expected spin-parities for the states are also shown. Data taken from the relevant Nuclear Data Sheets: [Ach06], [Zho94], [Xia05], [Sin07], [Kon07], [Kon05], [Kon04] and [Mar93].

7 Summary and future perspectives

The neutron deficient isotopes ^{191}Bi and ^{194,195,196}At have been investigated by means of in-beam and decay spectroscopy. The experiments utilized the JUROGAM Ge-detector array coupled with the recoil separator RITU and focal plane spectrometer GREAT and employed the powerful technique of recoil-decay tagging.

The study of ^{191}Bi confirmed and extended the previous level scheme and revealed two previously unobserved superdeformed bands. ^{191}Bi is the lightest bismuth isotope by far in which a stable superdeformed minimum has been observed so far. In ^{195}At prompt gamma rays feeding the $i_{13/2}$ isomeric state were detected for the first time. The level structure indicated strong coupling of the valence proton to the core, as is the case in ^{191}Bi also. A detailed decay spectroscopic study was undertaken to study the odd-odd astatine isotopes ^{194,196}At. Low statistics made this challenging, but nevertheless it was possible to draw some conclusions for the decay paths of both these isotopes.

Some open questions remain. In ^{191}Bi a number of weak gamma-ray transitions feeding the $1/2^+$ inruder state could not be placed into the level scheme. It appears that the level structures above the $1/2^+$ state are especially complex in ^{191}Bi which lies in a transitional region between predominantly oblate and prolate deformations. It would be important to be able to detect the linking transitions between the superdeformed and normally deformed states, but this is an enormous experimental challenge. The decay out pattern between the observed SD bands and the alpha decaying $1/2^+$ and $9/2^-$ states could not be determined accurately. Doing this would require recoil gated data set with sufficient statistics to analyze higher gamma-ray multiplicities, which was not achieved in the present experiment. Also there is a possibility of heretofore unobserved superdeformed bands.

In ^{195}At the level structure directly feeding the alpha decaying $7/2^-$ state is still unknown due to insufficient statistics for $\gamma\gamma$-coincidence analysis. However, it was apparent that the structure will be different to that observed in ^{191}Bi, due to the different gamma-ray energies. This is in contrast to the case of the $i_{13/2}$ bands, which are roughly similar. Also the feeding of the $1/2^+$ ground state in ^{195}At could not be determined with much confidence due to the very limited statistics.

In the odd-odd At isotopes the alpha decays are complicated by the coincident highly converted transitions in the daughter nuclei and the resultant conversion electron summing in the Si-detector. Much improved statistics would be required to assess this problem, and observation of low-energy gamma rays will be needed to be able to fix the excitation energies of at least some of the levels fed in the decays. It should be noted that the results reported here came from an experiment not optimized for decay studies. The reaction was chosen to produce ^{195}At and beam current was limited to serve the needs of in-beam spectroscopy. A decay study with improved statistics is therefore feasible. Also the prompt gamma rays feeding the light odd-odd At isotopes have not been experimentally studied so far.

The JUROGAM II spectrometer which employs Clover Ge-detectros has been commissioned in Jyväskylä and is currently operating in conjunction with RITU and GREAT. Digital electronics have been succesfully tested with the Ge-detectors to allow for increased counting rates and thus relieve the beam current limitations for in-beam experiments. A proposal has already been made by the author of this thesis to employ the setup to study superdeformation and other open questions in ^{193}Bi. The future implementation of the SAGE in-beam electron spectrometer and LISA charged particle detector for evaporation channel selection will further increase the selective power of the system. With regard to the odd-odd isotopes SAGE could be useful as converted prompt transitions and magnetic rotation are likely to be present.

References

[Alp69] M. Alpsten and G. Astner,
Nuclear Physics A **134** 407 (1969).

[Ach06] E. Achterberg, O.A. Capurro, G.V. Marti, V.R. Vanin and R.M. Castro,
Nuclear Data Sheets **107** 1 (2006).

[All98] R.G. Allatt, R.D. Page, M. Leino, T. Enqvist, K. Eskola, P.T. Greenlees, P. Jones, R. Julin, P. Kuusiniemi, W.H. Trzaska and J. Uusitalo,
Physics Letters B **437** 29 (1998).

[And76] G. Andersson,
Nuclear Physics A **286** 205 (1976).

[And00] A.N. Andreyev, M. Huyse, P. van Duppen, L. Weissman, D. Ackermann, J. Gerl, F.P. Heßberger, S. Hofmann, A. Kleinböhl, G. Münzenberger, S. Reshitko, C. Schlegel, H. Schaffner, P. Cagarda, M. Matos, S. Saro, A. Keenan, C. Moore, C.D. O'Leary, R.D. Page, M. Taylor, H. Kettunen, M. Leino, A. Lavrentiev, R. Wyss and K. Heyde,
Nature **405** 430 (2000).

[And03a] A.N. Andreyev, D. Ackermann, F.P. Heßberger, S. Hofmann, M. Huyse, I. Kojouharov, B. Kindler, B. Lommel , G. Münzenberg, R.D. Page, K. van de Vel, P. van Duppen and K. Heyde,
European Physical Journal A **18** 55 (2003).

[And03b] A.N. Andreyev, D. Ackermann, S. Antalic, H.J. Boardman, P. Cagarda, J. Gerl, F.P. Heßberger, S. Hofmann, M. Huyse, D. Karlgren, A. Keenan, H. Kettunen, A. Kleinböhl, B. Kindler, I. Kojouharov, A. Lavrentiev, C.D. O'Leary, M. Leino, B. Lommel, M. Matos, C.J. Moore, G. Münzenberg, R.D. Page, S. Reshitko, S. Saro, H. Schaffner, C. Schlegel, M.J. Taylor, K. van de Vel, P. van Duppen, L. Weissman and K. Heyde,
European Physical Journal A **18** 39 (2003).

[And04a] A.N. Andreyev, D. Ackermann, F.P. Heßberger, K. Heyde, S. Hofmann, M. Huyse, D. Karlgren, I. Kojouharov, B. Kindler, B. Lommel, G. Münzenberg, R D. Page, K. Van de Vel, P. Van Duppen, W.B. Walters and R. Wyss,
Physical Review C **69** 054308 (2004).

[And04b] A.N. Andreyev, P.A. Butler, R.D. Page, D.E. Appelbe, G.D. Jones, D.T. Joss, R.-D. Herzberg, P.H. Regan, J. Simpson and R. Wadsworth,
Nuclear Instruments and Methods in Physics Research A **533** 422 (2004).

[And06] A.N. Andreyev, S. Antalic, D. Ackermann, S. Franchoo, F.P. Heßberger, S. Hofmann, M. Huyse, I. Kojouharov, B. Kindler, P. Kuusiniemi, S.R. Lesher, B. Lommel, R. Mann, G.Münzenberg, K. Nishio, R.D. Page, J.J. Ressler, B. Streicher, S. Saro, B. Sulignano, P. van Duppen, and D.R. Wiseman,
Physical Review C **73** 024317 (2006).

[And08] K. Andgren, U. Jakobsson, B. Cederwall, J. Uusitalo, T. Back, S.J. Freeman, P.T. Greenlees, B. Hadinia, A. Hugues, A. Johnson, P.M. Jones, D.T. Joss, S. Juutinen, R. Julin, S. Ketelhut, A. Khaplanov, M. Leino, M. Nyman, R.D. Page, P. Rahkila, M. Sandzelius, P. Sapple, J. Sarén, C. Scholey, J. Simpson, J. Sorri, J. Thomson and R. Wyss,
Physical Review C **78** 044328 (2008).

[And09] A.N. Andreyev, S. Antalic, D. Ackermann, L. Bianco, S. Franchoo, S. Heinz, F.P. Heßberger, S. Hofmann, M. Huyse, I. Kojouharov, B. Kindler, B. Lommel, R. Mann, K. Nishio, R.D. Page, J.J. Ressler, P. Sapple, B. Streicher, Š. Šaro, B. Sulignano, J. Thomson, P. Van Duppen and M. Venhart,
Physical Review C **79** 064320 (2009).

[Bal92] G. Baldsiefen, H. Hübel, D. Mehta, B.V. Thirumala Rao, U. Birkental, G. Fröhlingsdorf, M. Neffgen, N. Nenoff, S.C. Pancholi, N. Singh, W. Schmitz, K. Theine, P. Willsau, H. Grawe, J. Heese, H. Kluge, K.H. Maier, M. Schramm, R. Schubart and H.J. Maierc,
Physics Letters B **275** 252 (1992).

[Bal94] G. Baldsiefen, H. Hübel, W. Korten, D. Mehta, N. Nenoff, B.V. Thirumala Rao, P. Willsau, H. Grawe, J. Heese, H. Kluge, K.H. Maier, R. Schubart, S. Frauendorf and H.J. Maier,
Nuclear Physics A **574** 521 (1994).

[Bas09] M.S. Basunia,
Nuclear Data Sheets **110** 1205 (2009).

[Bax93] A.M. Baxter, A. P. Byrne, G.D. Dracoulis, R.V.F. Janssens, I.G. Bearden, R.G. Henry, D. Nisius, C.N. Davids, T.L. Khoo, T. Lauritsen, H. Penttilä, D.J. Henderson and M.P. Carpenter,
Physical Review C **48** R2140 (1993).

[Bec92] J.A. Becker, E.A. Henry, A. Kuhnert, T.F. Wang, S.W. Yates, R.M. Diamond, F.S. Stephens, J.E. Draper, W. Korten, M.A. Deleplanque, A.O. Macchiavelli, F. Azaiez, W.H. Kelly, J.A. Cizewski and M.J. Brinkman,
Physical Review C **46** 889 (1992).

[Ben79] R. Bengtsson and S. Frauendorf,
Nuclear Physics A **327** 139 (1979).

[Ben04] M. Bender, P. Bonche, T. Duguet and P.-H. Heenen,
Physical Review C **69** 064303 (2004).

[Beu92] C.W. Beausang, S.A. Forbes, P. Fallon, P.J. Nolan, P.J. Twin, J.N. Mo, J.C. Lisle, M.A. Bentley, J. Simpson, F.A. Beck, D. Curien, G. deFrance and G. Duchêne,
Nuclear Instruments and Methods in Physics Research A **313** 37 (1992).

[Bij96] N. Bijnens, I. Ahmad, A.N. Andreyev, J.C. Batchelder, C.R. Bingham, D. Blumenthal, B.C. Busse, X.S. Chen, L.F. Conticchio, C.N. Davids, M. Huyse, R.V.F. Janssens, P. Mantica, H. Penttilä, W. Reviol, D. Seweryniak, P. van Duppen, W.B. Walters, J. Wauters, B.E. Zimmerman,
Zeitscrift für Physik A **356** 3 (1996).

[Bil86] J. Billowes
Hyperfine Interactions **30** 265 (1986).

[Boh75] A. Bohr and B.R. Mottelson,
Nuclear Structure Volume II: Nuclear Deformations, W.A. Benjamin Inc., New York (1975).

[Bra80] R.A. Braga, W.R. Western, J.L. Wood, R.W. Fink, R. Stone, C.R. Bingham and L.L. Riedinger,
Nuclear Physics A **349** 61 (1980).

[Cha86] T. Chapuran, K. Dybdal, D.B. Fossan, T. Lönnroth, W.F. Piel Jr., D. Horn and E.K. Warburton,
Physical Review C **33** 130 (1986).

[Cla95] R.M. Clark, S. Bouneau, F. Azaiez, S. Asztalos, J.A. Becker, B. Cederwall, M.A. Deleplanque, R.M. Diamond, J. Duprat, P. Fallon, L.P. Farris, E.A. Henry, J.R. Hughes, W.H. Kelly, I.Y. Lee, A.O. Macchiavelli, M.G. Porquet, J.F. Sharpey-Schafer, F.S. Stephens, M.A. Stoyer, D.T. Vo and A. N. Wilson,
Physical Review C **51** R1052 (1995).

[Cla96] R.M. Clark, S. Bouneau, A.N. Wilson, B. Cederwall, F. Azaiez, S. Asztalos, J.A. Becker, L. Bernstein, M.J. Brinkman, M.A. Deleplanque, I. Deloncle, R.M. Diamond, J. Duprat, P. Fallon, L.P. Farris, E.A. Henry, J.R. Hughes, W.H. Kelly, I.Y. Lee, A.O. Macchiavelli, M.G. Porquet, J.F. Sharpey-Schafer, F.S. Stephens, M.A. Stoyer and D.T. Vo,
Physical Review C **53** 117 (1996).

[Cla97] R.M. Clark, S.J. Asztalos, G. Baldsiefen, J.A. Becker L. Bernstein, M.A. Deleplanque, R.M. Diamond, P. Fallon, I.M. Hibbert, H. Hübel, R. Krücken, I.Y. Lee, A.O. Macchiavelli, R.W. MacLeod, G. Schmid, F.S. Stephens, K. Vetter and R. Wadsworth,
Physical Review Letters **78** 1868 (1997).

[Coc98] J.F.C. Cocks, M. Muikku, W. Korten, R. Wadsworth, S. Chmel, J. Domscheit, P.T. Greenlees, K. Helariutta, I. Hibbert, M. Houry, D. Jenkins, P. Jones, R. Julin, S. Juutinen, H. Kankaanpää, H. Kettunen, P. Kuusiniemi, M. Leino, Y. le Coz, R. Lucas, E. Mergel, R.D. Page, A. Savelius and W. Trzaska,
European Physical Journal A **3** 17 (1998).

[Coe85] E. Coenen, K. Deneffe, M. Huyse, P. van Duppen and J. L. Wood,
Physical Review Letters **54** 1783 (1985).

[Coh58] B.L. Cohen and C.B. Fulmer,
Nuclear Physics **6** 547 (1958).

[Cov96] A. Covello (editor),
Proceedings of the 5th International Spring Seminar on Nuclear Physics, "New Perspectives in Nuclear Structure", World Scientific Press, Singapore, 417 (1996).

[Cwi87] S. Cwiok, J. Dudek, W. Nazarewicz, J. Skalski and T. Werner
Computer Physics Communications **46** 379 (1987).

[Dra98] G.D. Dracoulis, A.P. Byrne and A.M. Baxter,
Physics Letters B **432** 37 (1998).

[Dra01] G.D. Dracoulis, T. Kibdi, A.P. Byrne, A.M. Baxter, S.M. Mullins and R.A. Bark.
Physical Review C **63** 061302 (2001).

[Dra04] G.D. Dracoulis, G.J. Lane, A.P. Byrne, T. Kibédi, A.M. Baxter, A.O. Macchiavelli, P. Fallon and R.M. Clark,
Physical Review C **69** 054318 (2004).

[Dup84] P. van Duppen, E. Coenen, K. Deneffe, M. Huyse, K. Heyde and P. van Isacker,
Physical Review Letters **52** 1974 (1984).

[Dup85] P. van Duppen, E. Coenen, K. Deneffe, M. Huyse and J. L. Wood,
Physics Letters B **154** 354 (1985).

[Dup91] P. van Duppen, P. Decrock, P. Dendooven, M. Huyse, G. Reusen and J. Wauters,
Nuclear Physics A **529** 268 (1991).

[Dön83] F. Dönau and S. Frauendorf,
Proceedings of the Conference on High Angular Momentum Properties of Nuclei, Oak Ridge, Tennessee, USA, 1982, edited by N.R. Johnson (Harwood, New York, 1983), p. 143.

[Dön87] F. Dönau,
Nuclear Physics A **471** 469 (1987).

[Enq96] T. Enqvist,
PhD Thesis, JYFL Research Report 3/1996.

[Fir96] R.B. Firestone and V.S. Shirley (editors),
Table of Isotopes, 8th edition, John Wiley Sons, Inc., New York (1996).

[Fos03] R. Fossion, K. Heyde, G. Thiamova and P. van Isacker,
Physical Review C **67** 024306 (2003).

[Fra93] S. Frauendorf,
Nuclear Physics A **557** 259 (1993).

[Fra97] S. Frauendorf,
Zeitschrift für Physik A **358** 163 (1997).

[Gal58] C.J. Gallagher and S.A. Moszkowski,
Physical Review **111** 1282 (1958).

[Ghi88] A. Ghiorso, S. Yashita, M.E. Leino, L. Frank, J. Kalnins, P. Armbruster, J.-P. Dufour and P.K. Lemmertz,
Nuclear Instruments and Methods in Physics Research A **269** 192 (1988).

[Har65] S.M. Harris,
Physical Review **138** 509 (1965).

[Har83] K. Hardt, Y.K. Agarwal, C. Giinther, M. Guttormsen, R. Kroth, J. Recht, F.A. Beck, T. Byrski, J.C. Merdinger, A. Nourredine, D.C. Radford, J.P. Vivien and C. Bourgeois,
Zeitschrift für Physik A **312** 251 (1983).

[Hee93] J. Heese, K.H. Maier, H. Grawe, J. Grebosz, H. Kluge, W. Meczynski, M. Schramm, R. Schubart, K. Spohr and J. Styczen,
Physics Letters B **302** 390 (1993).

[Hei95] P. Heikkinen and E. Liukkonen,
Proceedings on the 14th International Conference on Cyclotrons and their Applications, Cape Town (World Scientific, Singapore) 66 (1995).

[Hel99] K. Helariutta, J.F.C. Cocks, T. Enqvist, P.T. Greenlees, P. Jones, R. Julin, S. Juutinen, P. Jämsen, H. Kankaanpää, H. Kettunen, P. Kuusiniemi, M. Leino, M. Muikku, M. Piiparinen, P. Rahkila, A. Savelius, W.H. Trzaska, S. Törmänen, J. Uusitalo, R.G. Allatt, P.A. Butler, R.D. Page and M. Kapusta,
European Physical Journal A **6** 289 (1999).

[Hess06] F.P. Heßberger, S. Hofmann, D. Ackermann, S. Antalic, B. Kindler, I. Kojouharov, P. Kuusiniemi, M. Leino, B. Lommel, R. Mann, K. Nishio, A.G. Popeko, B. Sulignano, S. Saro, B. Streicher, M. Venhart and A.V. Yeremin,
European Physical Journal A **29** 165 (2006).

[Hey83] K. Heyde, P. van Isacker, M. Waroquier, J.L. Wood and R.A. Meyer,
Physics Reports **102** 291 (1983).

[Huy88] M. Huyse, E. Coenen, K. Deneffe, P. van Duppen, K. Heyde and J. van Maldeghem,
Physics Letters B **201** 293 (1988).

[Hüb86] H. Hübel, A.P. Byrne, S. Ogaza, A.E. Stuchbery, G.D. Dracoulis and M. Guttormsen,
Nuclear Physics A **453** 316 (1986).

[Hüb05] H. Hübel,
Progress in Particle and Nuclear Physics **54** 1 (2005).

[Hür04a] A. Hürstel, Y. Le Coz, E. Bouchez, A. Chatillon, A. Görgen, P.T. Greenlees, K. Hauschild, S. Juutinen, H. Kettunen, W. Korten, P. Nieminen, M. Rejmund, Ch. Theisen, J. Wilson, A.N. Andreyev, F. Becker, T. Enqvist, P.M. Jones, R. Julin, H. Kankaanpää, A. Keenan, P. Kuusiniemi, M. Leino, A.-P. Leppänen, M. Muikku, J. Pakarinen, P. Rahkila and J. Uusitalo,
European Physical Journal A **21** 365 (2004).

[Hür04b] A. Hürstel,
PhD Thesis, Universite Louis Pasteur Strasbourg 2002.

[Ing54] D.R. Inglis,
Physical Review **96** 1059 (1954).

[Jai00] A. Jain, A.K. Jain and B. Singh,
Atomic Data and Nuclear Data Tables **74** 283 (2000).

[Jen00] D.G. Jenkins, M. Muikku, P.T. Greenlees, K. Hauschild, K. Helariutta, P.M. Jones, R. Julin, S. Juutinen, H. Kankaanpaa, N.S. Kelsall, H. Kettunen, P. Kuusiniemi, M. Leino, C.J. Moore, P. Nieminen, C.D. O'Leary, R.D. Page, P. Rakhila, W. Reviol, M.J. Taylor, J. Uusitalo and R. Wadsworth,
Physical Review C **62** 021302(R) (2000).

[Jen02] D.R. Jensen, G.B. Hagemann, I. Hamamoto, S.W. Ødegard, M. Bergström, B. Herskind, G. Sletten, S. Törmänen, J.N. Wilson, P. O. Tjøm, K. Spohr, H. Hübel, A. Görgen, G. Schönwasser, A. Bracco, S. Leoni, A. Maj, C.M. Petrache, P. Bednarczyk and D. Curien,
Nuclear Physics A **703** 3 (2002).

[Jul01] R Julin, K Helariutta and M Muikku,
Journal of Physics G **27** R109 (2001).

[Ket03a] H. Kettunen, T. Enqvist, M. Leino, K. Eskola, P.T. Greenlees, K. Helariutta, P. Jones, R. Julin, S. Juutinen, H. Kankaanpää, H. Koivisto, P. Kuusiniemi, M. Muikku, P. Nieminen, P. Rahkila and J. Uusitalo,
European Physical Journal A **16** 457 (2003).

[Ket03b] H. Kettunen, T. Enqvist, T. Grahn, P.T. Greenlees, P. Jones, R. Julin, S. Juutinen, A. Keenan, P. Kuusiniemi, M. Leino, A.-P. Leppänen, P. Nieminen, J. Pakarinen, P. Rahkila and J. Uusitalo,
European Physical Journal A **17** 537 (2003).

[Kho96] T.L. Khoo, M.P. Carpenter, T. Lauritsen, D. Ackermann, I. Ahmad, D.J. Blumenthal, S.M. Fischer, R.V.F. Janssens, D. Nisius, E.F. Moore, A. Lopez-Martens, T. Døssing, R. Krücken, S.J. Asztalos, J.A. Becker, L. Bernstein, R.M. Clark, M.A. Deleplanque, R.M. Diamond, P. Fallon, L.P. Farris, F. Hannachi, E.A. Henry, A. Korichi, I.Y. Lee, A.O. Macchiavelli and F.S. Stephens,
Physical Review Letters **76** 1583 (1996).

[Kib08] T. Kibédi, T.W. Burrows, M.B. Trzhaskovskaya, P.M. Davidson and C.W. Nestor Jr.,
Nuclear Instruments and Methods in Physics Research A **589** 202 (2008).

[Koi01] H. Koivisto, P. Heikkinen, V. Hänninen, A. Lassila, H. Leinonen, V. Nieminen, J. Pakarinen, K. Ranttila, J. Ärje and E. Liukkonen,
Nuclear Instruments and Methods in Physics Research B **174** 379 (2001).

[Kon04] F.G. Kondev,
Nuclear Data Sheets **101** 521 (2004).

[Kon05] F.G. Kondev,
Nuclear Data Sheets **105** 1 (2005).

[Kon07] F.G. Kondev,
Nuclear Data Sheets **108** 365 (2007).

[Kor91] M.O. Kortelahti, E.F. Zganjar, J.L. Wood, C.R. Bingham, H.K. Carter, K.S. Toth, J.H. Hamilton, J. Kormicki, L. Chaturvedi and W.B. Newbolt,
Physical Review C **43** 484 (1991).

[Kre81a] A.J. Kreiner, M.A.J. Mariscotti, C. Baktash, E. der Mateosian and P. Thieberger,
Physical Review C **23** 748 (1981).

[Kre81b] A.J. Kreiner, C. Baktash, G. Garcia Bermudez and M.A.J. Mariscotti,
Physical Review Letters **47** 1709 (1981).

[Kre88] A.J. Kreiner, J. Davidson, M. Davidson, H. Mosca, L.L. Riedinger, C.R. Bingham, M.W. Guidry and A.C. Kahler,
Physical Review C **38** 2674 (1988).

[Kri92] S.J. Krieger, P. Bonche, M.S. Weiss, J. Meyer, H. Flocard and P.-H. Heenen,
Nuclear Physics A **542** 43 (1992).

[Lan95] G.J. Lane, G.D. Dracoulis, A.P. Byrne, P.M. Walker, A.M. Baxter, J.A. Sheikh and W. Nazarewicz,
Nuclear Physics A **586** 316 (1995).

[Lau02] T. Lauritsen, M.P. Carpenter, T. Døssing, P. Fallon, B. Herskind, R.V.F. Janssens, D.G. Jenkins, T.L. Khoo, F.G. Kondev, A. Lopez-Martens, A.O. Macchiavelli, D. Ward, K.S. Abu Saleem, I. Ahmad, R. Clark, M. Cromaz, J.P. Greene, F. Hannachi, A.M. Heinz, A. Korichi, G. Lane, C.J. Lister, P. Reiter, D. Seweryniak, S. Siem, R.C. Vondrasek and I. Wiedenhöver,
Physical Review Letters **88** 042501 (2002).

[Laz01] I.H. Lazarus, D.E. Appelbe, P.A. Butler, P.J. Coleman-Smith, J.R. Cresswell, S.J. Freeman, R.-D. Herzberg, I. Hibbert, D.T. Joss, S.C. Letts, R.D. Page, V.F.E. Pucknell, P.H. Regan, J. Simpson, J. Thornhill and R. Wadsworth,
IEEE Transactions on Nuclear Science **48**, 567 (2001).

[Lei83] M. Leino,
Thesis, University of Helsinki Report Series in Physics, HU-P-D37/1983.

[Lei95] M. Leino, J. Äystö, T. Enqvist, P. Heikkinen, A. Jokinen, M. Nurmia, A. Ostrowski, W.H. Trzaska, J. Uusitalo, K. Eskola, P. Armbruster and V. Ninov,
Nuclear Instruments and Methods in Physics Research B **99** 653 (1995).

[Lei03] M. Leino,
Nuclear Instruments and Methods in Physics Research B **204** 129 (2003).

[Lop96] A. Lopez-Martens, F. Hannachi, A. Korichi, C. Schück, E. Gueorguieva, Ch. Vieu, B. Haas, R. Lucas, A. Astier, G. Baldsiefen, M. Carpenter, G. de France, R. Duffait, L. Ducroux, Y. le Coz, Ch. Finck, A. Görgen, H. Hübel, T. L. Khoo, T. Lauritsen, M. Meyer, D. Prvost, N. Redon, C. Rigollet, H. Savajols, J.F. Sharpey-Schafer, O. Stezowski, Ch. Theisen, U. van Severen, J.P. Vivien and A.N. Wilson,
Physics Letters B **380** 18 (1996).

[Lön86] T. Lönnroth, C.W. Beausang, D.B. Fossan, L. Hildingsson, W.F. Piel Jr., M.A. Quader, S. Vajda, T. Chapuran and E.K. Warburton,
Physical Review C **33** 1641 (1986).

[Ma86] W.C. Ma, A.V. Ramayya, J.H. Hamilton, S.J. Robinson, J.D. Cole, E.F. Zganjar, E.H. Spejewski, R. Bengtsson, W. Nazarewicz and J.-Y. Zhang,
Physics Letters B **167** 277 (1986).

[Ma93] W.C. Ma, J.H. Hamilton, A.V. Ramayya, L. Chaturvedi, J.K. Deng, W.B. Gao, Y.R. Jiang, J. Kormicki, X.W. Zhao, N.R. Johnson, J.D. Garrett, I.Y. Lee, C. Baktash, F.K. McGowan, W. Nazarewicz and R. Wyss,
Physical Review C **47** R5 (1993).

[Mar93] M.J. Martin,
Nuclear Data Sheets **70** 315 (1993).

[Moo89] E.F. Moore, R.V.F. Janssens, R.R. Chasman, I. Ahmad, T.L. Khoo, F.L.H. Wolfs, D. Ye, K.B. Beard, U. Garg, M.W. Drigert, Ph. Benet, Z.W. Grabowski and J.A. Cizewski,
Physical Review Letters **63** 360 (1989).

[Naz85] W. Nazarewicz, J. Dudek, R. Bengtsson, and I. Ragnarsson,
Nuclear Physics A **435** 397 (1985).

[Nef95] M. Neffgen, G. Baldsiefen, S. Frauendorf, H. Grawe, J. Heese, H. Hübel, H. Kluge, A. Korichi, W. Korten, K.H.Maier, D. Mehta, J. Meng, N. Nenoff, M. Piiparinen, M. Schönhofer, R. Schubart, U.J. van Severen, N. Singh, G. Sletten, B.V. Thirumala Rao and P. Willsau,
Nuclear Physics A **595** 499 (1995).

[New74] J.O. Newton, F.S. Stephens and R.M. Diamond,
Nuclear Physics A **236** 225 (1974).

[Nie04] P. Nieminen, S. Juutinen, A.N. Andreyev, J.F.C. Cocks, O. Dorvaux, K. Eskola, P.T. Greenlees, K. Hauschild, K. Helariutta, M. Huyse, P.M. Jones,

R. Julin, H. Kankaanpää, H. Kettunen, P. Kuusiniemi, Y. Le Coz, M. Leino, T. Lönnroth, M. Muikku, P. Rahkila, A. Savelius, J. Uusitalo, N. Amzal, N.J. Hammond, C. Scholey and R. Wyss
Physical Review C **69** 064326 (2004).

[Nil55] S.G. Nilsson,
Det Kongelige Danske Videnskabernes Selskab Matematisk-Fysiske Meddelelser **29** no. 16 (1955).

[Nol90] P.J. Nolan,
Nuclear Physics A **520** c657 1990.

[Nor50] L.W. Nordheim,
Physical Review **78** 294 (1950).

[Nya84] B.M. Nyak, J.R. Cresswell, P.D. Forsyth, D. Howe, P.J. Nolan, M.A. Riley, J.F. Sharpey-Schafer, J. Simpson, N.J. Ward and P.J. Twin,
Physical Review Letters **52** 507 (1984).

[Paa79] V. Paar,
Nuclear Physics A **331** 16 (1979).

[Pag03] R.D. Page, A.N. Andreyev, D.E. Appelbe, P.A. Butler, S.J. Freeman, P.T. Greenlees, R.-D. Herzberg, D.G. Jenkins, G.D. Jones, P. Jones, D.T. Joss, R. Julin, H. Kettunen, M. Leino, P. Rahkila, P.H. Regan, J. Simpson, J. Uusitalo, S.M. Vincent and R. Wadsworth,
Nuclear Instruments and Methods in Physics Research B **204** 634 (2003).

[Pak05a] J. Pakarinen,
PhD Thesis, JYFL Research Report 4/2005.

[Pak05b] J. Pakarinen, I.G. Darby, S. Eeckhaudt, T. Enqvist, T. Grahn, P.T. Greenlees, V. Hellemans, K. Heyde, F. Johnston-Theasby, P. Jones, R. Julin, S. Juutinen, H. Kettunen, M. Leino, A.-P. Leppänen, P. Nieminen, M. Nyman, R. D. Page, P. M. Raddon, P. Rahkila, C. Scholey, J. Uusitalo, and R. Wadsworth,
Physical Review C **72** 011304(R) (2005).

[Pau99] Programs for calculating single-particle/quasiparticle energies,
http://ns.ph.liv.ac.uk/∼esp/nuclear/WS/.

[Pie85] W.F. Piel Jr., T. Chapuran, K. Dybdal, D.B. Fossan, T. Lönnroth, D. Horn and E.K. Warburton,
Physical Review C **31** 2087 (1985).

[Per62] V.P.Perelygin, S.P.Almazova, B.A.Gvozdev *et al.*,
Zhurnal Eksperimental'noi i Teoreticheskoi Fiziki **42** 1472 (1962), Soviet Physics JETP **15** 1022 (1962).

[Pol62] S.M.Polikanov, V.A.Druin, V.A.Karnaukhov *et al.*,
Zhurnal Eksperimental'noi i Teoreticheskoi Fiziki **42** 1464 (1962), Soviet Physics JETP **15** 1016 (1962).

[Rad95a] D.C. Radford,
Nuclear Instruments and Methods in Physics Research A **361** 297 (1995).

[Rad95b] D.C. Radford,
Nuclear Instruments and Methods in Physics Research A **361** 306 (1995).

[Rah08] P. Rahkila,
Nuclear Instruments and Methods in Physics Research A **595** 637 (2008).

[Rev94] W. Reviol, L.L. Riedinger, J.-Y. Zhang, C.R. Bingham, W.F. Müller, B.E. Zimmerman, R.V.F. Janssens, M.P. Carpenter, I. Ahmad, I.G. Bearden, R.G. Henry, T.L. Khoo, T. Lauritsen and Y. Liang,
Physical Review C **49** R587 (1994).

[Rev95] W. Reviol, L.L. Riedinger. J.M. Lewis, W.F. Müller. C.R. Bingham, J.Y. Zhang and B. E. Zimmerman,
Physica Scripta **T56** 167 (1995).

[Ros93] C. Rossi Alvarez,
Nuclear Physics News **3** 3 (1993).

[Sat91] W. Satula, S. Ćwiok, W. Nazarewicz, R. Wyss and A. Johnson,
Nuclear Physics A **529** 289 (1991).

[Sch84] K.-H. Schmidt, C.-C. Sahm, K. Pielenz and H.-G. Clerc,
Zeitschrift für Physik A **316** 19 (1984).

[Sch86] K.-H. Schmidt, R. S. Simon, J.-G. Keller, F.P. Heßberger, G. Münzenberg, B. Quint, H.-G. Clerc, W. Schwab, U. Gollerthan and C.-C. Sahm,
Physics Letters B **168** 39 (1986).

[Seg65] E. Segrè,
Nuclei and Particles - An Introduction to Nuclear and Subnuclear Physics, W.A. Benjamin Inc., New York Amsterdam (1965).

[Sie04] S. Siem, P. Reiter, T.L. Khoo, T. Lauritsen, P.-H Heenen, M.P. Carpenter, I. Ahmad, H. Amro, I.J. Calderin, T. Døssing, T. Duguet, S.M. Fischer, U. Garg, D. Gassmann, G. Hackman, F. Hannachi, K. Hauschild, R.V.F.

Janssens, B. Kharraja, A. Korichi, I-Y. Lee, A. Lopez-Martens, A.O. Macchiavelli, E.F. Moore, D. Nisius and C. Schück,
Physical Review C **70** 014303 (2004).

[Sin02] Balraj Singh, Roy Zywina and Richard B. Firestone,
Nuclear Data Sheets **97** 241 (2002).

[Sin07] B. Singh,
Nuclear Data Sheets **108** 79 2007.

[Smi99] M.B.Smith, R Chapman, J.F.C. Cocks, O Dorvaux, K Helariutta, P.M. Jones, R. Julin, S. Juutinen, H. Kankaanpää, H. Kettunen, P. Kuusiniemi, Y. Le Coz, M. Leino, D.J. Middleton, M. Muikku, P. Nieminen, P. Rahkila, A Savelius and K.-M. Spohr,
European Physical Journal A **5** 43 (1999).

[Smi00] M.B.Smith, R Chapman, J.F.C. Cocks, K.-M. Spohr, O Dorvaux, K Helariutta, P.M. Jones, R. Julin, S. Juutinen, H. Kankaanpää, H. Kettunen, P. Kuusiniemi, Y. Le Coz, M. Leino, D.J. Middleton, M. Muikku, P. Nieminen, P. Rahkila and A Savelius,
Journal of Physics G **26** 787 (2000).

[Str67] V.M. Strutinsky,
Nuclear Physics A **95** 420 (1967).

[Suh07] J. Suhonen,
From Nucleons to Nucleus - Concepts of Microscopic Nuclear Theory, Springer-Verlag, Berlin Heidelberg (2007).

[Taa61] R. Taagepera and M. Nurmia,
Annales academiæ Scientiarum fennicæ A **78** VI 1 (1961).

[Tay99] R.B.E. Taylor, S.J. Freeman, J.L. Durell, M.J. Leddy, S.D. Robinson, B.J. Varley, J.F.C. Cocks, K. Helariutta, P. Jones, R. Julin, S. Juutinen, H. Kankaanpää, A. Kanto, H. Kettunen, P. Kuusiniemi, M. Leino, M. Muikku, P. Rahkila, A. Savelius and P.T. Greenlees,
Physical Review C **59** 673 (1999).

[The08] Ch. Theisena, A. Lopez-Martens and Ch. Bonnelle,
Nuclear Instruments and Methods in Physics Research A **589** 230 (2008).

[Twi85] P.J. Twin, A.H. Nelson, B.M. Nyak, D. Howe, H.W. Cranmer-Gordon, D. Elenkov, P.D. Forsyth, J.K. Jabber, J.F. Sharpey-Schafer, J. Simpson and G. Sletten,
Physical Review Letters **55** 1380 (1985).

[Twi86] P.J. Twin, B.M. Nyak, A.H. Nelson, J. Simpson, M.A. Bentley, H.W. Cranmer-Gordon, P.D. Forsyth, D. Howe, A.R. Mokhtar, J.D. Morrison, J.F. Sharpey-Schafer and G. Sletten,
Physical Review Letters **57** 811 (1986).

[Uus05] J. Uusitalo, M. Leino, T. Enqvist, K. Eskola, T. Grahn, P.T. Greenlees, P. Jones, R. Julin, S. Juutinen, A. Keenan, H. Kettunen, H. Koivisto, P. Kuusiniemi, A.-P. Leppänen, P. Nieminen, J. Pakarinen, P. Rahkila and C. Scholey Physical Review C **71** 024306 (2005).

[Uus08] J. Uusitalo, personal communication.

[Van07] V.R. Vanin, N.L. Maidana, R.M. Castro, E. Achterberg, O.A. Capurro, G.V. Martí,
Nuclear Data Sheets **108** 2566 (2007).

[Vel03] K. van de Vel, A.N. Andreyev, R.D. Page, H. Kettunen, P.T. Greenlees, P. Jones, R. Julin, S. Juutinen, H. Kankaanpää, A. Keenan, P. Kuusiniemi, M. Leino, M. Muikku, P. Nieminen, P. Rahkila, J. Uusitalo, K. Eskola, A. Hürstel, M. Hyuse, Y. le Coz, M.B. Smith, P. van Duppen and R. Wyss,
European Physical Journal A **17** 167 (2003).

[Wil03] A.N. Wilson, G.D. Dracoulis, A.P. Byrne, P.M. Davidson, G.J. Lane, R.M. Clark, P. Fallon, A. Görgen, A.O. Macchiavelli and D. Ward,
Physical Review Letters **90** 142501 (2003).

[Wil05a] A.N. Wilson, G.D. Dracoulis, A.P. Byrne, P.M. Davidson, G.J. Lane, R.M. Clark, P. Fallon, A. Görgen, A.O. Macchiavelli and D. Ward,
European Physical Journal A **24** 179 (2005).

[Wil05b] A.N. Wilson, A.K. Singh, H. Hübel, P.M. Davidson, A. Görgen, D. Roßbach, A. Korichi, A. Astier, F. Azaiez, D. Bazzacco, C. Bourgeois, N. Buforn, A.P. Byrne, G.D. Dracoulis, F. Hannachi, K. Hauschild, W. Korten, T. Kröll, G.J. Lane, A. Lopez-Martens, N. Redon, P. Reiter, C. Rossi-Alvarez, G. Schonwaßer, O. Stezowski and P.G. Thirolf,
Physical Review Letters **95** 182501 (2005).

[Wis07] D.R. Wiseman, A.N. Andreyev, R.D. Page, M.B. Smith, I.G. Darby, S. Eeckhaudt, T. Grahn, P.T. Greenlees, P. Jones, R. Julin, S. Juutinen, H. Kettunen, M. Leino, A.-P. Leppänen, M. Nyman, J. Pakarinen, P. Rahkila, M. Sandzelius, J. Sarén, C. Scholey and J. Uusitalo,
European Physical Journal A **34** 275 (2007).

[Woo92] J.L. Wood, K. Heyde, W. Nazarewicz, M. Hyuse and P. van Duppen,
Physics Reports **215** 101 (1992).

[Wu92] C.S. Wu, J.Y. Zeng, Z. Xing, X.Q. Chen and J. Meng,
Physical Review C **45** 261 (1992).

[Wu97] C.S. Wu and Z.N. Zhou,
Physical Review C **56** 1814 (1997).

[Wu05] C.S. Wu,
Nuclear Data Sheets **106** 796 (2005).

[Xia05] Huang Xiaolong and Zhou Chunmei
Nuclear Data Sheets **104** 283 (2005).

[Yam67] T. Yamazaki
Nuclear Data A **3** 1 (1967).

[Yas83] S. Yashita,
Thesis, Lawrence Radiation Laboratory, Berkeley, 1983.

[Zho94] C. Zhou,
Nuclear Data Sheets **71** 367 (1994).